FU JEN STUDIES

NATURAL SCIENCES

NO. 7   1973

TENTH ANNIVERSARY
FU JEN CATHOLIC UNIVERSITY
ON TAIWAN
DECEMBER 8, 1973

FU JEN UNIVERSITY
TAIPEI, TAIWAN, REPUBLIC OF CHINA

This Anniversary Issue

is gratefully dedicated to

HIS EMINENCE PAUL CARDINAL YU PIN,

Rector Magnificus of Fu Jen University

and

FATHER DR. RICHARD ARENS SVD,

recently retired Dean of the College of Sciences.

FU JEN STUDIES

NATURAL SCIENCES

NO. 7   1973

CONTENTS

THE EQUATORIAL EVENING MINIMUM IN IONOSPHERIC ELECTRON CONTENT

JOHN KOSTER, SVD

1. INTRODUCTION

In a previous paper entitled "An investigation of the total electron content of the equatorial ionosphere" (Koster, 1971), a description was given of a relatively simple experiment which enables one to determine on an almost continuous basis the total electron content of the equatorial ionosphere. This paper gives a discussion of an "anomaly" in the equatorial ionosphere discovered by this experiment. For the benefit of those who do not regularly concern themselves with this region of the world we preface our main paper with a few remarks about the ionosphere in general and its structure relative to the earth's magnetic field at the equator.

2. THE IONOSPHERE

The ionosphere is described as "that part of the earth's upper atmosphere where ions and electrons are present in quantities sufficient to affect the propagation of radio waves." In practice, we are here concerned with the portion of the atmosphere which lies above a height of about 60 km, and below about 1,000 km. 99.9% of the earth's atmosphere lies below 60 km, and hence does not concern us. Another 99% of the remainder is not ionized, and so does not enter directly into our discussion. The ionosphere is conventionally divided into regions given alphabetic designations, D, E, F in ascending order. The boundary between the D and E regions is often taken as 90 km altitude, that between the E and F regions as 150 km. The lower E region is sometimes referred to as the dynamo region, since atmospheric winds or tides, moving charges across the earth's magnetic field lines, set up currents in this region analogous to the currents set up in the armature of a dynamo.

The process of ionization, we will recall, lies in the removal by radiant energy from the sun of an electron from its parent molecule or atom. The resulting positive ions are relatively massive and immobile, and do not normally affect radio waves appreciably. But the light electrons are highly mobile, and their influence on a passing radio wave can be profound. Radio waves travel more rapidly in a region containing free electrons than they travel in a vacuum. Hence the ionosphere has a different "index of refraction" than the surrounding unionized atmosphere, and this can give rise to the phenomena of refraction and reflection familiar to all students of optics.

3. FARADAY ROTATION

Electrons can influence a radio wave in another very interesting and important way. The wave which we normally pick up with our television aerial is "plane polarized". The wave is made up of mutually perpendicular electric and magnetic fields, which are also perpendicular to the direction of propagation of the wave. A horizontally polarized wave travels with its electric field vector in a horizontal plane, its magnetic field vector in a vertical plane. Such a wave normally travels with the speed of light, the electric and magnetic field vectors being confined to mutually perpendicular planes. If now our wave encounters some free electrons, its speed will change. If an external magnetic field is also present, the plane of polarization of the wave will rotate. The wave will proceed with a twisting motion, and the twist angle can be measured experimentally. This effect is described as "Faraday rotation". It is of great importance to the experimentalist, since there is a relatively simple relationship connecting the twist angle on one hand, and the number of electrons as well as the direction and intensity of the external magnetic field on the other. The usual situation is this. We can measure the total twist angle; we already know the direction and intensity of the earth's magnetic field. From these we can deduce the number density of electrons required to produce the observed twist.

4. DETAILS OF THE EXPERIMENT

In the experiment being reported on here a synchronous satellite (ATS-C) emits plane polarized radio waves at a frequency of 136.98 MHz (i. e. a wavelength of 2.2 meters). It will be recalled that a synchronous orbit is one in which the satellite moves eastward in an equatorial plane at a height of 35,800 km. Its eastward movement just keeps pace with the earth's rotation, so that to an observer on the earth the satellite's position appears to be fixed. If the total twist angle of the received wave is measured, one has valuable information about the number of electrons along the path from observer to satellite. Such measurements have been made at Legon, Ghana (latitude 5.63°N, longitude 0.19°W) on a nearly continuous basis since 1969. The rest of this paper deals with the results obtained from these measurements of the twist angle, hereafter referred to as total Faraday angle, (TFA) of the received wave.

5. AN ANOMALY DISCLOSED BY FARADAY ROTATION

It is common practice in ionospheric physics to postulate some hypothetical and usually grossly over-simplified model of the iono-spheric region in question, and then to describe departures from this model as anomalies. In the present case we shall assume such an over-simplified model of the equatorial ionosphere. In this model, the buildup of electrons in the ionosphere begins at sunrise, and proceeds rapidly as the sun's increasing elevation angle leads to an increase in energy flux.

At noon the influx reaches its maximum. Around this time the loss rate of electrons (due to the recombination of ions and electrons) will just balance production rates, and the electron content of the ionosphere will reach its daily maximum. As the sun's zenith angle increases again, the electron content should begin to drop. At sunset the production rate drops to zero, while the loss processes continue to operate. Our model predicts that the electron content should continue to decrease in an exponential manner through the night, reaching its diurnal minimum just before sunrise.

The gross features of experimental curves of the daily variation of the electron content of the ionosphere agree with this rather crude model. But one very striking "anomaly" appears. Attention has been called (Koster 1972) to the unexpected behaviour of the total Faraday angle in the hours immediately following sunset. Many plots show a sharp diminution in the value of the total Faraday angle immediately after sunset, with a subsequent rise to a maximum before diminishing to the expected sunrise minimum. This feature will be referred to as the *equatorial evening minimum.*

It should be pointed out that our "anomaly" is far from an unusual feature. It appears in at least eight of the twelve monthly mean plots of TFA obtained each year. In this paper it is proposed to investigate the equatorial evening minimum more closely and to suggest a physical mechanism which could be responsible for this unexpected variation of TFA with time.

6. THE NATURE AND FREQUENCY OF THE ANOMALY

Figure 1 is an example of a rather extreme, but not unusual case of the equatorial evening minimum. A smooth curve has been drawn through the discrete values of the TFA obtained from our polarimeter at ten minute intervals.

If the minimum value of TFA is called TFA_{min}, and the maximum value some two hours later designated as TFA_{max}, it is found that the ratio of these two values is equal to 0.34 for this particular record. Some twenty four consecutive daily curves are shown in a recent research report (Koster and Beer, 1972); of these, five had values approximately equal to that shown in Figure 1.

Monthly mean curves of TFA as a function of time are shown in a more recent report (Koster, 1973). From these one can draw three conclusions about the equatorial evening effect:

(a) It is a fairly common effect. The effect is clearly evident in ten of sixteen monthly mean plots. It is suggested in three more, and is totally absent in three cases. Such an effect can show up in monthly mean plots only if the frequency of occurrence is quite high.
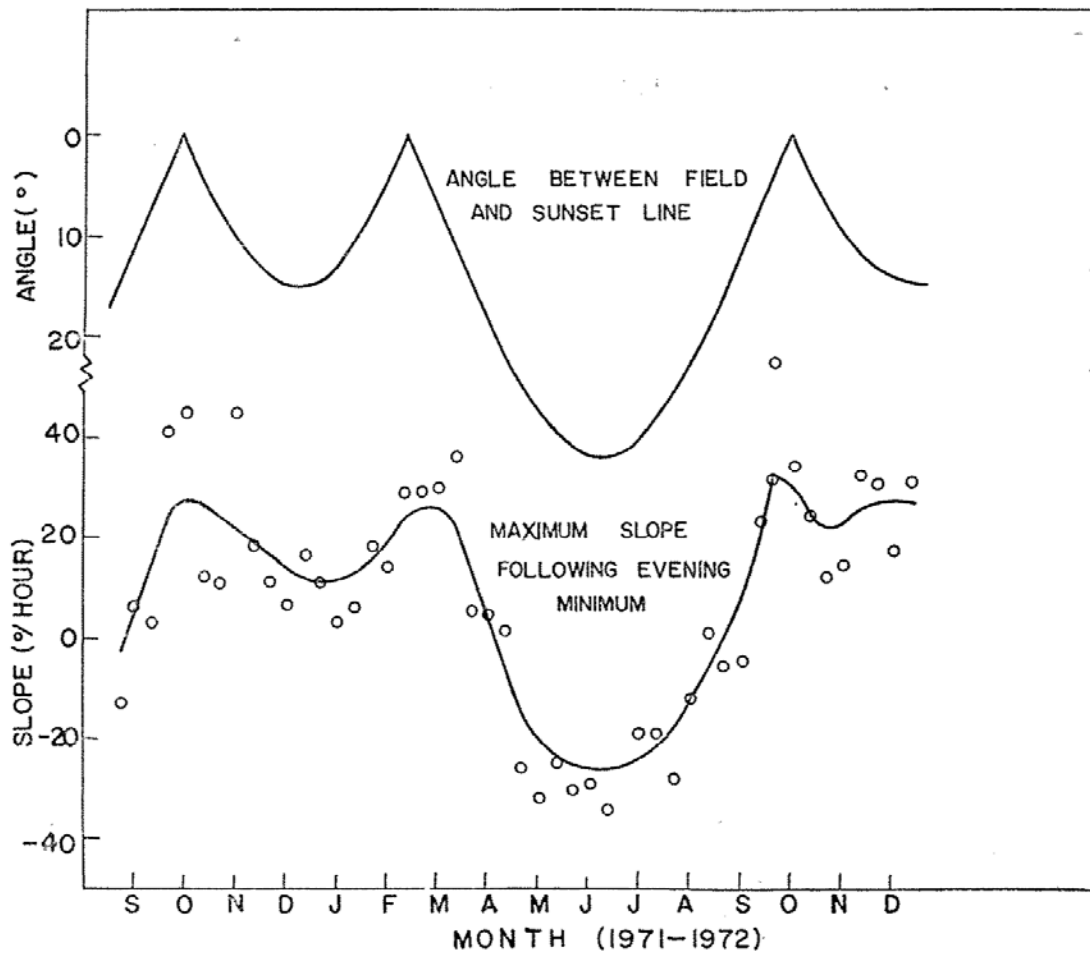
Figure 1. A typical plot of Faraday angle versus time, showing
the equatorial Faraday minimum.

(b) The phenomenon must be quite regular. If the occurrence
were at random times, it would be smoothed out by the monthly
averaging process.

(c) The effect is seasonal. It appears most prominently in the
curves for the equinoctial months, while it is almost totally
absent around the June solstice.

7. THE SEASONAL VARIATION OF THE ANOMALY

Individual daily TFA curves show many and varied structures.
To eliminate to some extent these daily peculiarities, ten-day mean
curves of TFA against time of day were produced. The degree to
which the equatorial evening minimum is present in these curves is
determined by measuring the maximum slope, in degrees per hour,

in the interval 20h–24h local time. Curves with a pronounced equatorial evening minimum will have a large positive maximum slope in this period; curves without the effect will exhibit a negative slope throughout the period.

The value of the maximum slope for each ten day interval is plotted in Figure 2, together with a smoothed curve, produced by a modified exponential smoothing procedure. In this curve, the seasonal variation shows up very clearly. We summarize the results as follows:

(a) The curve has a deep minimum at the June solstice, a much shallower minimum at the December solstice.

(b) The maxima occur about 25 days after the September equinox and about 15 days before the March equinox respectively.

(c) This seasonal variation is in good agreement with the seasonal dependence of thermospheric temperature (Jacchia, 1967) and the seasonal variation of scintillation at Legon (Koster, 1972).

(d) Figure 2 also shows a plot of the angle between the sunset line and the horizontal component of the earth's magnetic field at Legon. The similarity of the two curves is striking. The discussion of a possible explanation of this similarity is given later.

8. A PHYSICAL INTERPRETATION OF THE OBSERVATIONS

It has long been recognized that the well known vertical rise and fall of the equatorial ionosphere around sunset could be a contributing factor to an equatorial evening minimum. An approximate expression for the Faraday rotation angle Ω is given by the expression:

$$\Omega = \frac{K}{f^2} \bar{M} N_t$$

where: K is a numerical constant,

f is the frequency of the radio wave (in Hertz)

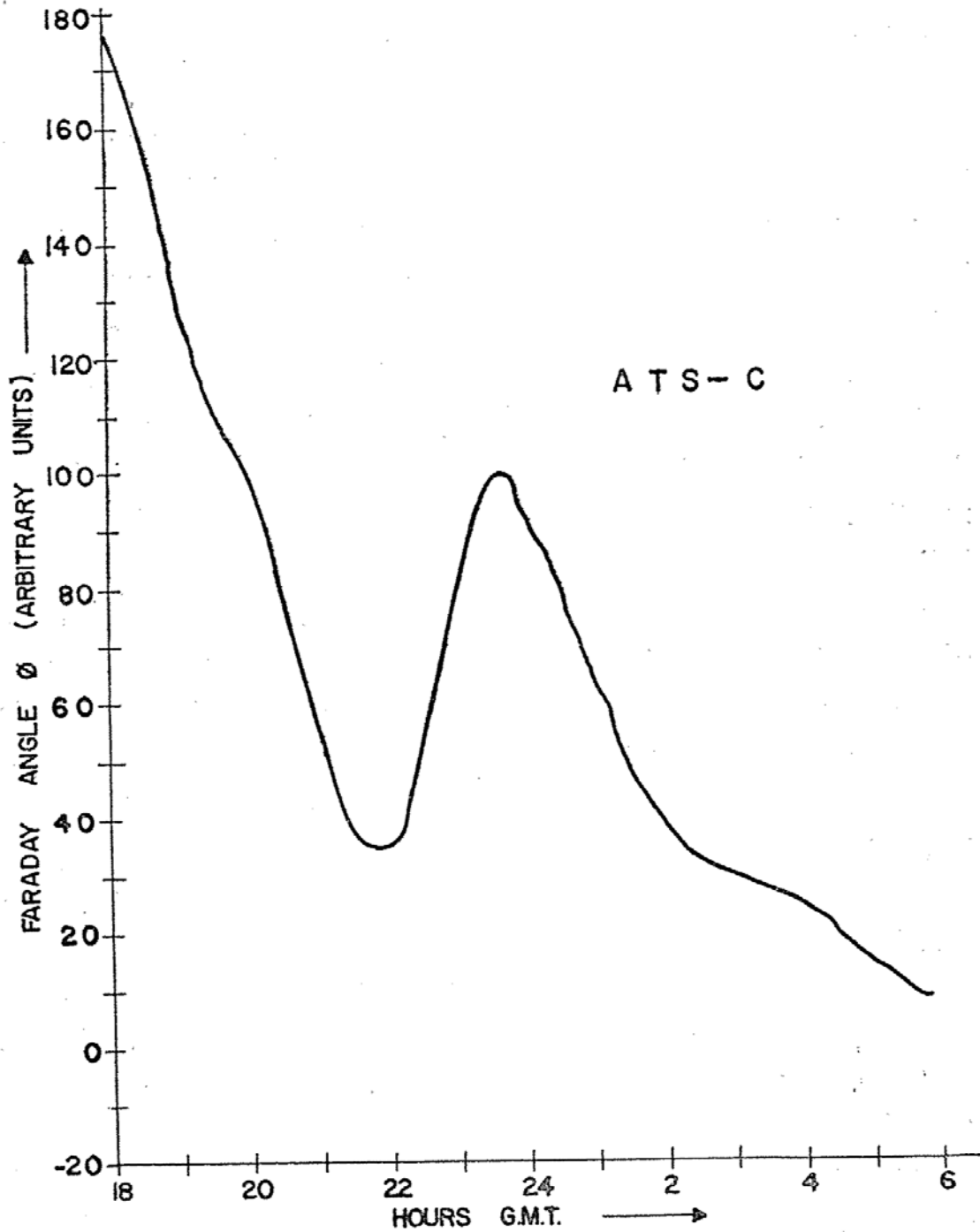$\bar{M}$ is H cos θ sec χ (the weighted mean effect of the magnetic field).

Figure 2. The seasonal variation of the maximum slope of night time TFA curves.

N_t is the total electron content in electrons/m^2 of a vertical column through the ionosphere.

Since K is a constant, and f is fixed during the observations, variations in Ω can be accounted for in terms of variations of the value of $\bar{M}$

with time as well as of variations in the actual total electron content of the ionosphere N_t. We consider briefly the contributions that these two factors make to the equatorial evening minimum.

$\bar{M}$ is usually calculated at some assumed appropriate height (420km is now frequently used). Since M is a function of height, decreasing as the height is increased, it is clear that if electrons present in the ionosphere were to rise to a much greater height, the appropriate value of M would increase, and the corresponding TFA observed would decrease, even though the total number of electrons remained unchanged. The crucial question is: Could this effect alone produce the equatorial evening minimum? The answer is definitely in the negative. A realistic mathematical model of the equatorial ionosphere indicates that a rise of more than 600 km would be required to explain an observation such as that shown in Figure 1. The smallest value of TFA_{min}/TFA_{max} achievable by this mechanism alone in terms of acceptable (i. e. agreeing with observations) changes in ionospheric height is about 0.74. The observed value is frequently of the order of 0.34. We conclude, therefore, that the rise and fall of the ionization in the ionosphere around sunset cannot by itself adequately explain the magnitude of the equatorial evening minimum, though it is almost certainly a contributing factor to it.

Since we cannot explain the variation in TFA in terms of $\bar{M}$, we must seek an explanation in terms of variations in N_t. The obvious way to do this is to postulate a horizontal movement to accompany the well known vertical movements.

This has been done, and the results evaluated on an electronic computer. Appropriate (and physically realistic) values of horizontal velocity, combined with the known vertical velocities, give rise to simulated experimental curves that bear a striking resemblance to the actual ones. This suggests quite strongly that there is a large circulatory movement in the equatorial ionosphere after sunset. How can such a circulatory motion of electrons and ions in the equatorial F region of the ionosphere be set up?

9. A MECHANISM FOR PRODUCING
A CIRCULATORY MOTION

The type of circulatory motion mentioned above calls for a large and temporally increasing upward velocity on the day (i. e. west) side of the sunset line, then a rapid reversal and a large downward velocity on the dark (i. e. east) side of the line. Even larger horizontal velocities are required if we are to produce results similar to those actually observed. Horizontal and vertical velocities must be related in such a way that at any point in space the net outward velocity from an element of volume is zero—i. e. the divergence of the velocity must be zero.

It is readily seen that just such a circulatory motion would be produced by an electrostatic field arising from a concentration of electrons in a region just behind (i. e. east of) the sunset line in the dynamo region of the ionosphere.

We here briefly describe the mechanism envisaged. Neutral winds cause a concentration of electrons in two regions north and south of the equator respectively. These "clouds" of electrons give rise to electrostatic fields. The fields are transferred along the earth's magnetic field lines to the F region of the ionosphere over the equator. Since the earth's magnetic field lines are equipotentials (almost), the electrostatic field over the equator will have the form shown in Figure 3. The electric field vectors point inwards the electric charge (electrons) located in the central elliptical region. Equipotentials are a family of confocal ellipses, as indicated in Figure 3. The earth's magnetic field is not shown in the figure, but it can be considered as uniform, and directed into the plane of the paper.

It will be recalled that both positive and negative charges, when located in a region where both an electric field E and a magnetic field B are present, and where collisions with other particles are negligible, will move in a direction $E \times B$, i. e. at right angles to both E and B. In our case this means a movement along the direction of one of the elliptical equipotential lines. Since the electric field intensity increases as we get closer to the centre, the velocity along the inner ellipses is much greater than that along the outer ones.
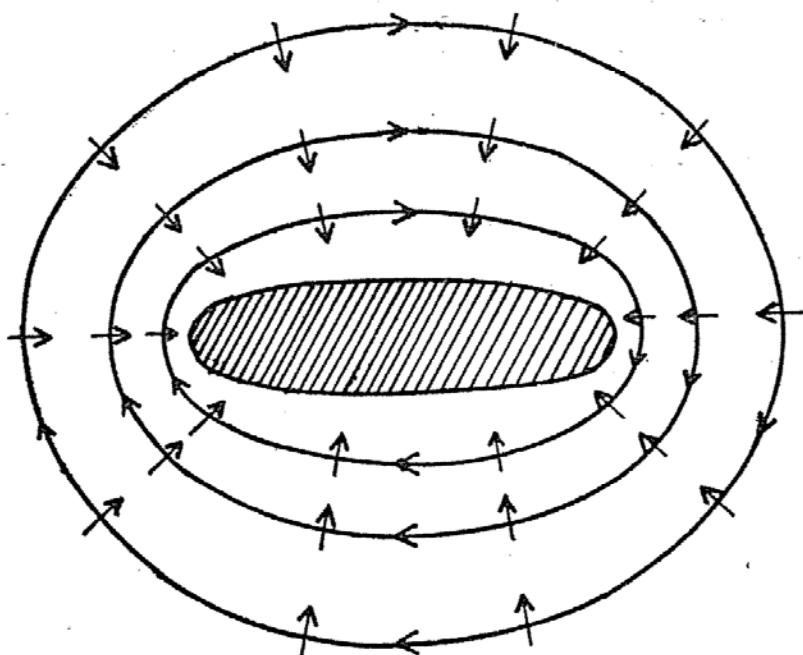
Figure 3.   Equipotentials and fields in a vertical E-W plane
over the equator.   Movement of charges is in
the direction of the ellipses.

Granted that a circulatory motion would result from an electro-static field such as that postulated above, we are now entitled to ask whether there is any theoretical or experimental evidence for the actual existence of such a concentration of electrons along the sunset line, and the resultant electric fields.

In 1972 Carlson and Walker predicted just such a charge concentration with reference to the sunrise line. Their arguments have equal validity in the case of the sunset line, as we propose here. Their prediction was on purely theoretical grounds.

Most of the existing experimental equipment for the measurement of electron velocities is limited to the measurement of only one component of that velocity.

Thus measurements made at Jicamarca, Peru (Balsley and Wood-man, 1971) show large vertical velocities in the F region, and cor-respondingly large horizontal velocities in the E region. These velocity components reverse shortly after ionospheric sunset. These experimental results are consistent with the suggested circulation. Hence it is fair to say that the fields and circulation suggested here

are in comformity with theoretical predictions, and consistent with existing experimental results.

10. THE NET RESULT OF OUR CIRCULATORY MOTION

It must be remembered that the sunset line moves westward with a speed of 500 m/sec at F region heights. An instantaneous "snapshot" would show velocities directed along the lines of confocal ellipses as described above. But the whole family of ellipses moves westward with the velocity of the sunset line. Individual electrons will execute a rather complex motion. But the net result can be summarized quite simply. Consider an original vertical line of electrons.

(a) All electrons end up at the same level as that on which they began (except those, of course, which were lost through recombination during the time interval.)

(b) Electrons above a certain level suffer a net displacement eastward.

(c) Electrons below that level are displaced towards the west. An observer making measurements vertically upward would "see" first a trough, then a crest, in the total electron content above him.

A computer was used to calculate the Faraday angle that an observer would record between the hours of sunset and midnight while such an elliptical circulation cell passed over his site. The results agree very well with actual experimental curves obtained at Legon.

11. A POSSIBLE CONNECTION BETWEEN THE EVENING MINIMUM AND EQUATORIAL SCINTILLATION

Our Faraday rotation measurements suggest rather strongly that a large elliptical "circulation cell" moves westward along the equator at a speed of 500 m/sec. One of the principal motives for investigating the equatorial evening minimum is the fact that it possibly holds the key to the explanation of another baffling equatorial "anomaly". We here refer to the night time appearance of intense irregularities in the electron density of the F region over the equator.

These irregularities are known to give rise to the "scintillation" of radio stars, to rapid amplitude and phase fluctuations in radio signals transmitted through the ionosphere from satellites, and in the rapid and deep fading of signals from transmitters on earth when these signals are received via one or more reflections from the equatorial ionosphere. These same irregularities are shown on ionograms as "Spread F". The various manifestations of the presence of these electron density variations have been known for many decades, but an acceptable mechanism for their generation, consistent with all known experimental facts, has still not been proposed.

12. THE POUSSE CAFE EFFECT

A number of the great ideas of science seem to have originated as scientists brooded over their drinks. Thus Weizsaecker produced his famous "coffee-cup" theory for the formation of spiral galaxies. The original idea from which the liquid hydrogen bubble chamber arose is alleged to have occurred to a scientist contemplating his glass of beer. In the present situation a theoretical physicist (appropriately named Beer) has produceed a theory based on yet another product of the bartender's art—the "pousse-cafe". For those matters, a pousse-cafe is defined as "a cocktail consisting of several liqueurs of different colours and specific gravities poured so as to remain in separate layers." The denser layers are on the top in a pousse-cafe, and the whole system is therefore gravitationally unstable. Any attempt to drink it causes instability to set in, and the liqueurs mix.

Our suggestion here is that the upper atmosphere at the equator is like a pousse-cafe, in that it is gravitationally unstable, a heavy layer of electrons and ions overlaying a lighter layer beneath. The large rise of the electrons and ions relative to the neutral atmosphere just before sunset can certainly be a contributing factor to such an unstable situation. But this is not sufficient in itself to account for the generation of irregularities high up in the ionosphere. Beer, in his theory of the pousse-cafe effect, invokes another mechanism called the "spatial resonance effect." If ionization, moving with the elliptical

circulation velocities described above, interacts with gravity waves in the neutral atmosphere, it can set up a number of layers in which a more dense fluid overlays a less dense one. The force of gravity then produces the irregularities, much as it causes a pousse-cafe to mix.

The theory is still in its developmental stage, however, and we shall not say more about it here.

13. CONCLUSION

The evening minimum in the total Faraday angle measured at the equator is an observed fact. Our attempt to explain it in terms of an electrostatic field originating from an accumulation of charge in the dynamo region of the ionosphere is in agreement with the theory proposed by Carlson and Walker (1972) and with the experimental results of Balsley and Woodman (1971).

The moving elliptical circulation cell suggested here would produce the variation in TFA observed at the equator.

The movements described here would not by themselves produce electron density irregulatities, but they could contribute to a gravitationally unstable situation through interaction with atmospheric gravity waves in the spatial resonance effect. This could set up a multi-layered "pousse-cafe". Its collapse is thought to give rise to the observed irregularities.

REFERENCES

(1) Koster, John R., 1971: An investigation of the total electron content of the equatorial ionosphere. *Fu Jen Studies* 4, 105.

(2) Koster, John R., 1972: Equatorial Scintillation. *Planet Space Sci.* 20, 1999-2014.

(3) Koster J. R. & Beer, T., 1972: *Final Scientific Report. Ionospheric Research Using Statellites. An Interpretation of Ionospheric Faraday Rotation Observations at the Equator.* Dept. of Physics, University of Ghana, June, 1972.

(4) Koster, J. R., 1973: *Ionospheric Research Using Satellites. The Equatorial Evening Minimum.* Dept. of Physics, Univ. of Ghana, April, 1973.

(5) Jacchia, L. G., 1967: Properties of the upper atmosphere determined from satellite orbits. *Phil. Trans. Roy. Soc. Lond.* A 262, 157

(6) Carlson, H. C. Jr. & Walker, James C. G.: Electrodynamic drift in the neutral F-region Ionosphere caused by conjugate point sunrise. *Planet Space Sci.* **20**, 141–148.

(7) Balsley, Ben B. and Woodman, Ronald F.: *Ionosphere Drift Velocity Measurements at Jicamarca, Peru.* (July 1967–March 1970). Report UAG17, World Data Center. *An Upper Atmosphere Geophysics*, NOAA, Boulder, Colorado.

CORRECTED ONSAGER FORMULAS FOR PURE LIQUIDS WITH ANISOTROPIC MOLECULES

GÜNTER BREUER

ABSTRACT

The method of the reaction field for ellipsoidal molecules (ONSAGER-SCHOLTE model) is presented, taking into account the interaction of the reaction field with the induced dipole moment of electrically and optically anisotropic molecules. Corrected formulas are derived for the molecular refraction, the molecular polarization and the Kerr constant. For the electrical and optical polarization, model calculations are carried out for a number of pure organic liquids and the results are compared with experimental data.

1. INTRODUCTION

Microscopic theories of dielectrica concerning the short range interaction and spacial arrangement of neighbouring molecules within a liquid have been developed by KIRKWOOD[1] and, more generally by FRÖHLICH[2]. While these theories are of most general validity, detailed knowledge of the type of the molecular interaction as well as the spacial and directional correlation of the molecules is needed in order to apply the formalism to a practical case. Mostly however, the microscopic structure of a liquid is not known, which imposes a serious limitation to the applicability.

On the other hand, the semimicroscopic approach of the continuum theory of ONSAGER[3], using the well-known method of the "reaction field", has been proved widely useful as far as the short range interactions can be neglected, which seemed to be true for a large number of liquids except those of the associated type. The refinement of the Onsager-theory by SCHOLTE[4] considering an ellipsoidal cavity instead of a spherical one, and thus accounting for the shape anisotropy of the molecule, has made the theory even more successfull. The dielectric properties calculated by this model show fairly good

agreement with the experimental data in most cases and the remaining deviations can well be attributed to the simplifying assumptions the theory is based upon.

The molecular constants used in the Onsager-Scholte model are the following

 i)   the electrical and optical main polarizabilities,
 ii) the permanent electric dipole moment,
 iii) the semiaxis of the ellipsoidal cavity, defining its volume and its shape.

These parameters are all molecular constants (for the free molecule) by means of which it should be possible to derive the dielectric properties of the substance in the liquid state assuming that the molecules outside of the cavity are randomly distributed and have random directional orientation. This, however, is an oversimplification because even in the case of non-associated liquids a "preferred" distribution and/or directional orientation of neighbouring molecules with respect to a center molecule cannot be ruled out completely.

Furthermore, the assumption concerning the above mentioned theoretical parameters as being "molecular constants" is not quite correct in the case of the cavity parameters. The volume of the cavity has always been a point at issue. It should be remembered that in the spherical case, adopting the "Onsager condition"

(1-1) $$\frac{4\pi}{3} r^3 N = 1,\quad (N = \text{number of molecules per cm}^3)$$

which makes the cavity radius depend on the density, the Onsager formula is reduced to the Clausius-Mosotti equation (or the Lorentz-Lorenz equation) so that nothing new is gained. The other extreme which considers r as a constant, seems to be quite useful and leads to reasonable results so that it can be regarded as a kind of molecular constant, which in fact it is not. It can never be identified with the molecular radius, since in the liquid state the molecules do not form a "close packing". It is hardly possible to give satisfying reasons for any choice of the cavity radius. (This problem will be discussed also in section 4).

Similarly, the shape of the cavity, represented by the ratio of the semiaxes a, b, c, is also open to objection. Usually the shape parameters of the cavity are considered to be identical with those of the free molecule. Here again, because a liquid is not a close packing of molecules, the assumption seems not to be justified. A more suitable method would be to regard these constants as adjustable parameters within reasonable limits of variation, adjusted to fit the experimental data, thereby taking into account some part of the short range interactions not entering explicitly into the formalism of the reaction field.

2. BASIC FORMULAS FOR ISOTROPIC MOLECULES WITH SPHERICAL CAVITY

The Onsager theory describes the effective field $\vec{E}_m$, acting upon a molecule, as being composed of the "cavity field" and the "reaction field" by the formula

(2–1) $$\vec{E}_M = q \cdot \vec{E} + f \cdot \vec{m}$$

with

(2–2) $$q = \frac{3\varepsilon}{2\varepsilon + 1} \quad \text{and} \quad f = \frac{2(\varepsilon - 1)}{2\varepsilon + 1} \frac{1}{a^3}$$

where $\vec{E}$ is the external field, a is the cavity radius, and $\vec{m}$ is the total dipole moment which may be written as the sum of the permanent dipole moment and the induced dipole moment:

(2–3) $$\vec{m} = \vec{\mu} + \alpha \cdot \vec{E}_M$$

From eqs. (2–1) and (2–3) we get

(2–4) $$\vec{E}_M = q \cdot \vec{E} \frac{1}{1 - f \cdot \alpha} + f \cdot \vec{\mu} \frac{1}{1 - f \cdot \alpha}$$

(2–5) $$\vec{m} = \vec{\mu} \cdot \frac{1}{1 - f \cdot \alpha} + q \cdot \alpha \cdot \vec{E} \frac{1}{1 - f \cdot \alpha}.$$

To arrive at the molar polarization, we start with the fundamental equation

(2–6) $$\varepsilon - 1 = 4\pi N \frac{\partial}{\partial E} \langle m_E \rangle_{E \to 0}$$

where $E \to 0$ is necessary to avoid nonlinear effects which may occur at higher field strengths. N is the number of molecules per cm³ and $\langle m_B \rangle$ is the statistical average of the component of the dipole moment in the direction of the external field.

For any quantity X, the "mean value" $\langle X \rangle$ will be evaluated by the standard methods of the statistical mechanics using the formula

$$(2\text{-}7) \qquad \langle X \rangle = \frac{\int X \cdot \exp\left(-\frac{U}{kT}\right) d\Omega}{\int \exp\left(-\frac{U}{kT}\right) d\Omega}$$

U is the potential energy of the molecule in the field, depending on the coordinates Ω.

In our case we have $U = -(\vec{\mu} \cdot \vec{E}_M) - \frac{1}{2} \alpha \cdot E_M^2$ or, written explicitly:

$$(2\text{-}8) \qquad U = -q\frac{(\vec{\mu} \cdot \vec{E})}{(1-f \cdot \alpha)^2} - f \cdot \mu^2 \frac{1}{1-f \cdot \alpha} - \frac{1}{2}\alpha q^2 \frac{E^2}{(1-f \cdot \alpha)^2}$$

$$- \frac{1}{2}\alpha \frac{f^2 \mu^2}{(1-f \cdot \alpha)^2}$$

Here only the first term contributes to the averaging process, the other terms do not, because they are independent of the angle between $\vec{\mu}$ and $\vec{E}$. Evaluation of the statistical average of m_B yields

$$(2\text{-}9) \qquad \frac{1}{E}\langle m_B \rangle = q\left[\frac{\alpha}{1-f\alpha} + \frac{1}{3}\frac{\mu^2}{kT}\frac{1}{(1-f\alpha)^3}\right].$$

Therefore we get

$$(2\text{-}10) \qquad \varepsilon - 1 = 4\pi N \frac{3\varepsilon}{2\varepsilon+1}\left[\frac{\alpha}{1-f\alpha} + \frac{1}{3}\frac{\mu^2}{kT}\frac{1}{(1-f\alpha)^3}\right]$$

and, for the molar polarization

$$(2\text{-}11) \qquad P = \frac{\varepsilon-1}{\varepsilon+2}\frac{M}{\rho} = 4\pi N_A \frac{3 \cdot \varepsilon}{(2\varepsilon+1)(\varepsilon+2)}\left[\frac{\alpha}{1-f\alpha}\right.$$

$$\left. + \frac{1}{3}\frac{\mu^2}{kT}\frac{1}{(1-f\alpha)^3}\right]$$

where $N_A = 6.0225 \cdot 10^{23}$ is the Avogadro number.

The molar refraction R is obtained from the same formula by

writing n^2 instead of ε and neglecting the dipole term at the right hand side:

(2-12) $\qquad R = \dfrac{n^2-1}{n^2+2}\dfrac{M}{\rho} = 4\pi N_A \dfrac{3 \cdot n^2}{(2n^2+1)(n^2+2)} \cdot \dfrac{\alpha}{1-f\alpha}$,

with a corresponding change in the formula (2-2) for the reaction field constant f.

Eq. (2-10) is simply reduced to the well known Debye formula[5], which follows from neglecting the reaction field, $(f=0)$; and for $\varepsilon \approx 1$:

(2-13) $\qquad \varepsilon - 1 = 4\pi N \left[\alpha + \dfrac{\mu^2}{3kT} \right]$ (Debye formula)

Onsager derived his formula under the simplifying assumption that the dipole to be orientated has the moment $\vec{\mu}$, and not $\vec{\mu}/(1-f\alpha)$ which is the correct value. The field orienting the dipole is $q\vec{E}/(1-f\alpha)$. In Onsager's theory the interaction energy is $q(\vec{\mu}\cdot\vec{E})/(1-f\alpha)$, in contrast to the first term in our eq. (2-8). The formula of the early Onsager theory, instead of eq. (2-10), is the following:

(2-14) $\qquad \varepsilon - 1 = 4\pi N \dfrac{3\varepsilon}{2\varepsilon+1} \left[\dfrac{\alpha}{1-f\alpha} + \dfrac{1}{3}\dfrac{\mu^2}{kT}\dfrac{1}{(1-f\alpha)^2} \right]$

For further reference on the older theory, see FRÖHLICH[2]. The correction due to the "indirect effect" of the dipole orientation has first been pointed out by RAO[6].

In the present paper the consideration has been extended to the case of electrically and optically anisotropic molecules with an ellipsoidal cavity, which leads to a further correction of eq. (2-10)–(2-12).

3. GENERALIZED FORMULAS OF ELECTRICAL AND OPTICAL POLARIZATION FOR MOLECULES WITH ANISOTROPY

The method of the reaction field for ellipsoidally shaped molecules, as presented by SCHOLTE[4], can be corrected for the orientational effect of the molecular field on the induced dipole moment, if the molecules possess anisotropic polarizability. In this case the

vector of the induced dipole moment is not parallel to the effective field.

Consider $S' = (x_1', x_2', x_3')$ a cartesian coordinate system fixed with the molecule which may have an arbitrary orientation with respect to the laboratory system $S = (x_1, x_2, x_3)$, within which the electric field $\vec{E}$ is fixed. Let $T = (r_{ik})$ be the tensor which transforms S' into S. We assume that $\vec{E}$ lies in the direction of the x_3-axis and that the axes x_1', x_2', x_3' coincide with the directions of the main polarizabilities α_1, α_2, α_3, of the molecule. For each component of the effective field and of the total dipole moment in S' we have

(3–1) $\qquad E_{Mi}' = q_i \cdot E_i' + f_i \cdot m_i'$

(3–2) $\qquad m_i' = \mu_i' + \alpha_i \cdot E_{Mi}', \quad (i = 1, 2, 3)$

with the constants

(3–3) $\qquad q_i = \dfrac{\varepsilon}{\varepsilon + (1-\varepsilon)D_i} \quad f_i = \dfrac{3}{abc} \dfrac{D_i(1-D_i)(\varepsilon-1)}{\varepsilon + (1-\varepsilon)D_i}$

which describe the ellipsoidal cavity field and the reaction field. The D_i are the well known depolarizing factors and have been tabulated by OSBORN[7].

Equations (3–1) and (3–2) can be shortly written as

(3–4) $\qquad \vec{E}_M' = Q \cdot \vec{E}' + F \cdot \vec{m}'$

(3–5) $\qquad \vec{m}' = \vec{\mu}' + A \cdot \vec{E}_M'$

where Q, F, A are tensors with elements

(3–6) $\qquad q_{ik} = q_i \cdot \delta_{ik}, \; f_{ik} = f_i \cdot \delta_{ik}, \; \alpha_{ik} = \alpha_i \cdot \delta_{ik}.$

By rearrangement we get

(3–4′) $\qquad \vec{E}_M' = RQ \cdot \vec{E}' + RF \cdot \vec{\mu}'$

(3–5′) $\qquad \vec{m}' = R\vec{\mu}' + RAQ \cdot \vec{E}'$

where $R \equiv (I - AF)^{-1}$ with $I =$ unit tensor

The interaction energy is

(3–7) $\qquad U = -(\vec{\mu}' \vec{E}_M') - \dfrac{1}{2} A \vec{E}_M' \cdot \vec{E}_M'.$

Inserting the preceding equations we get

(3-7′)
$$U = -\vec{\mu'} \cdot RQ\vec{E'} - \vec{\mu'} \cdot RF\vec{\mu'} - \frac{1}{2}[ARQ\vec{E'} \cdot RQ\vec{E'}$$
$$+ ARQ\vec{E'} \cdot RF\vec{\mu'} + ARF\vec{\mu'} \cdot RQ\vec{E'} + ARF\vec{\mu'} \cdot RF\vec{\mu'}].$$

Among the different terms of U, the second and the sixth are constant; the remaining are, after some simplification

(3-8)
$$U' = -RQ\vec{E'} \cdot (I + ARF)\vec{\mu'} + \frac{1}{2}ARQ\vec{E'} \cdot RQ\vec{E'}$$

In our case, all tensors are diagonal and, noting that $I + ARF \equiv R$, we get

(3-8′)
$$U' = -RQ\vec{E'} \cdot R\vec{\mu'} - \frac{1}{2}ARQ\vec{E'} \cdot RQ\vec{E'}$$

where the tensor R of the reaction field has the components

(3-9)
$$r_{ik} = r_i \delta_{ik} \quad \text{with} \quad r_i = \frac{1}{1 - f_i \cdot \alpha_i}.$$

Let us write

$$\vec{\mu'} = \vec{\beta} \cdot \mu, \quad \text{with} \quad \vec{\beta} = \begin{pmatrix} \beta_1 \\ \beta_2 \\ \beta_3 \end{pmatrix} \text{ (unit vector)}$$

and

$$\vec{E'} = \vec{r} \cdot E, \quad \text{where} \quad \vec{r} = \begin{pmatrix} r_{13} \\ r_{23} \\ r_{33} \end{pmatrix} \begin{array}{l} \text{(the third column vector of} \\ T = (r_{ik})) \end{array}$$

U' can then be written explicitly

(3-8″)
$$U' = -\mu \cdot E \sum q_k \cdot r_k^2 \cdot \beta_k \cdot r_{k3} - \frac{1}{2} E^2 \sum \alpha_k \cdot q_k^2 \cdot r_k^2 \cdot r_{k3}^2$$

The E-component m_E of the total dipole moment becomes

$$m_E = \vec{m'} \cdot \vec{r} = (R\vec{\mu'}) \cdot \vec{r} + (RAQ\vec{E'}) \cdot \vec{r}$$

or, explicitly,

(3-5″)
$$m_E = \mu \cdot \sum r_k \cdot \beta_k \cdot r_{k3} + E \cdot \sum \alpha_k \cdot q_k \cdot r_k \cdot r_{k3}^2$$

With the equations (3-5″) and (3-8″), following the usual procedure of statistical mechanics, we can derive the formulas for the polarization and for the Kerr constant.

a) The electrical and optical polarization.

Using eq. (2–7) for the statistical average of m_R one needs only to consider the first order terms of E/kT, so that

$$-\frac{1}{E}\langle m_R\rangle = \frac{1}{3}\sum \alpha_k \cdot q_k \cdot r_k + \frac{\mu^2}{3kT}\sum \beta_k^2 \cdot q_k \cdot r_k^3$$

which leads to the formula

(3–10) $\varepsilon - 1 = \frac{4\pi}{3}N\left[\sum \alpha_k \cdot q_k \cdot r_k + \frac{\mu^2}{kT}\sum \beta_k^2 \cdot q_k \cdot r_k^3\right].$

With this formula we get the final expressions for the molar polarization and the molar refraction which are defined by the Clausius-Mosotti equation and the Lorentz-Lorenz equation

$$P_{CM} = \frac{\varepsilon - 1}{\varepsilon + 2}\frac{M}{\rho} \quad \text{and} \quad R_L = \frac{n^2 - 1}{n^3 + 2}\frac{M}{\rho}.$$

The result is

(3–11) $P = \frac{4\pi}{3}N_A \frac{1}{\varepsilon + 2}\left[\sum \alpha_k \cdot q_k \cdot r_k + \frac{\mu^2}{kT}\sum \beta_k^2 \cdot q_k \cdot r_k^3\right]$

and

(3–12) $R = \frac{4\pi}{3}N_A \frac{1}{n^2 + 2}\sum \alpha_k \cdot q_k \cdot r_k$

The quantities q_k and r_k, as defined by eqs. (3–3) and (3–9), are to be expressed in terms of ε and n^2 for P and R respectively.

b) The Kerr constant.

Let us assume, that the static electric field E_0 applied to the medium lies in the direction of the x_3-axis (z-axis), and the light propagates through the medium along the x_2-axis (y-axis). The field vector $\vec{E}_L$ of the light is assumed to be parallel or perpendicular to the static field, that means parallel to the z-axis or x-axis respectively. The Kerr constant is defined by

(3–13) $K = \frac{n_z - n_x}{n}\frac{1}{E_0^2}$

where the refractive indices n_z and n_x are those referring to the light polarized in z- and x-direction respectively, and n is the average between n_z and n_x.

The formula for K is derived from the fundamental formulas (1–6) applied to the optical case:

(3–14)
$$n_z^2 - 1 = 4\pi N \frac{1}{E_z} \langle m_{R\,z} \rangle$$

$$n_x^2 - 1 = 4\pi N \frac{1}{E_x} \langle m_{R\,x} \rangle$$

Again we use eq. (3–5″), which for E_z remains unaltered but, for E_x contains the tensor elements r_{k1} instead of r_{k3}:

(3–15)
$$m_{R\,z} = \mu \cdot \sum r_k \cdot \beta_k \cdot r_{k3} + E_z \sum \alpha_k \cdot q_k \cdot r_k \cdot r_{k3}^2$$

$$m_{R\,x} = \mu \cdot \sum r_k \cdot \beta_k \cdot r_{k1} + E_x \sum \alpha_k \cdot q_k \cdot r_k \cdot r_{k1}^2$$

U' is in this case completely determined by E_0, used in eq. (3–8″). The calculation of the statistical average $\langle m_{R\,z} \rangle$ and $\langle m_{R\,x} \rangle$ leads, after suitable arrangement of the different terms, to the expression

$$\frac{\langle m_{R\,z} \rangle}{E_z} = \frac{1}{3} \sum \alpha_k \cdot q_k \cdot r_k + \frac{E_0^2}{2kT} \left(\frac{1}{5} \sum a_k \cdot a_k^0 + \frac{1}{15} \sum_{j<k} a_k \cdot a_j^0 \right)$$

$$+ \frac{E_0^2 \mu^2}{2(kT)^2} \left(\frac{1}{5} \sum a_k \cdot b_k + \frac{1}{15} \sum_{j<k} a_k \cdot b_j \right)$$

$$- \frac{E_0^2}{2kT} \frac{1}{9} \sum a_k \cdot a_j^0 - \frac{E_0^2 \mu^2}{2(kT)^2} \sum a_k b_j$$

and a similar expression for $\frac{1}{E_x} \langle m_{R\,x} \rangle$.

Here the following abbreviations have been used:

(3–16)
$$a_k = \alpha_k \cdot q_k \cdot r_k$$
$$a_k^0 = \alpha_k^0 \cdot q_k^{02} \cdot r_k^{02}$$
$$b_k = q_k \cdot r_k^2 \cdot \beta_k$$

where q_k and r_k are from eq. (3–3) and (3–9). The superscript 0 indicates the electrostatic quantities expressed by ε, otherwise, expressed by n^2 for the optical quantities.

The equation for $\langle m_{R\,z} \rangle / E_z$, written above, and the corresponding one for $\langle m_{R\,x} \rangle / E_x$, can be put into a simpler form as follows:

$$\frac{\langle m_{R\,z} \rangle}{E_z} = \frac{1}{3} \sum a_k + \frac{E_0^2}{2} (2\theta_A + 2\theta_D)$$

$$\frac{\langle m_{Ex}\rangle}{E_x} = \frac{1}{3}\sum a_k - \frac{E_0^2}{2}(\theta_A+\theta_D)$$

where

(3-17)

$$\theta_A = \frac{1}{45kT}\sum_{j<k}(a_k-a_j)(a_k^0-a_j^0)$$

$$\theta_D = \frac{1}{45(kT)^2}\sum_{j<k}(a_k-a_j)(b_k^2-b_j^2)$$

usually called the "anisotropy term" and the "dipole term" of the Kerr constant.

By using eq. (3-14) and taking the difference, we get

$$n_z^2-n_x^2 = \frac{4\pi}{3}N\frac{E_0^2}{2}(\theta_A+\theta_D)+\frac{4\pi}{3}N\sum(a_{kz}-a_{kx})$$

In the last sum the indices z and x indicate that the values of a_k refer to the refractive indices n_z and n_x respectively. With eqs. (3-3) and (3-9) the complete expression for $(a_{kz}-a_{kx})$ is

(3-18)
$$a_{kz}-a_{kx} = (n_z^2-n_x^2)\frac{\alpha_k\cdot D_k\left(1+\frac{3\alpha_k}{abc}(D_k-1)\right)}{(n^2+(1-n^2)D_k)^2(1-f_k\cdot\alpha_k)^2}$$

$$= (n_z^2-n_x^2)\cdot C_k$$

With this equation we get

$$(n_z^2-n_x^2)(1-\frac{4\pi}{3}N\sum C_k)=4\pi N\frac{E_0^2}{2}\cdot 3(\theta_A+\theta_D)$$

or

$$n_z-n_x = \frac{3\pi N E_0^2}{n}(\theta_A+\theta_D)(1-\frac{4\pi}{3}N\sum C_k)^{-1}$$

and finally,

(3-19) $$K = \frac{3\pi N}{n^2}(\theta_A+\theta_D)(1-\frac{4\pi}{3}N\sum C_k)^{-1}$$

A similar formula has also been derived by RAO[8]*)

4. DISCUSSION

A) The polarization

There are two ways for testing the validity of the formulas for

---

*) The paper published by RAO[8] was unknown to the author until the completion of the present work.

the electric and optical polarization: 1.) one may compare the dipole moment of the free molecule with the value predicted by the theoretical formula for polar molecules or, 2.) one may investigate the functional dependence of ε (or n^2) by variation of temperature or pressure of the liquid. The calculated functions of the molar polarization and the molar refraction, of course, depend on the particular model adopted and on the choice of the model parameters.

In the following we review some earlier works based upon the Onsager-Scholte model.

For polar, yet isotropic molecules, ABBOTT and BOLTON[9] have derived a formula using a prolate spheroidal cavity. They neglect the anisotropy of polarizability and restrict the theory to molecules having a rotational symmetric shape. Values of μ, calculated from the experimental data of ε (liq.) for several organic compounds are compared with the dipole moment of the free molecule. It turned out that the calculated values lie about 5% to 15% lower than the true values but, in any case, are closer to the true values than the values obtained by using the spherical cavity. It was further shown that in the case of associated liquids (methylamine, hydrogen cyanide) the calculations become quite inadequate which, of course, is rather to be expected.

LE FEVRE and RAO[10], pursuing the same method, used the formula

$$\varepsilon - 1 = \frac{4\pi}{3} N \left[\sum \alpha_k q_k r_k + \frac{\mu^2}{kT} q_1 \cdot r_1^2 \right]$$

which corresponds to our formula (3-10) but has a factor r_1^2, whereas in our formula we have r^3. The formula is restricted to molecules whose dipole moment lies in the direction of one of the main polarizabilities. (This, however, is true for several molecules). Values of μ(calc.) and μ(gas) are compared for $CHCl_3$, C_6H_5Cl and $C_6H_5NO_2$. The result shows slight improvement with respect to the values predicted by the earlier theory of Scholte. The functional dependence of the molar polarization on temperature and pressure has also been investigated for several non-polar liquids and seems to give good results. The cavity radius was chosen using the relation

$$a^3 (= abc) = \frac{3}{4\pi N_A} \frac{M}{\rho_{mp}},$$

where M is the molecular weight and ρ_{mp} is the density at the melting point. The method for determining the cavity radius proposed by BÖTTCHER[11] has proved to be improper since it leads to much higher values of the polarization in the liquid state.*) The comparison of the molar polarization calculated from different formulas does not show a striking improvement gained by the corrected formula (which, for non-polar molecules coincides with our formula (3–10), because $\mu = 0$). This is a poor result partly because the temperature dependence has been considered at two different temperatures only, and the slight increase of R with increasing temperature (about 1%) has a large error**).

It seems therefore worthwhile to extend the investigation to the molar refraction by using eq. (3–12). The main advantage lies in the high precision and reliability of the optical refractive index. In the following, for a number of non-polar and polar molecules the theoretical values of the molar refraction have been calculated assuming different sets of model parameters and are compared with the values R_L (based upon the Lorentz-Lorenz formula) which are inserted into the diagrams as experimental points with errors indicated. The experimental data of $n(t)$ and $\varepsilon(t)$ are taken from standard tables [12,13,14]. The investigation was made for the following liquids: CS_2, C_6H_6, C_6H_5Cl, C_6H_5Br, $C_6H_5CH_3$, $CHCl_3$, $(C_2H_5)_2O$ and $(CH_3)_2CO$. The results are shown in the diagrams of Fig. 1, which represent the relative values of R normalized to the value at the lowest temperature. This seems to be the safest method in order to avoid the large errors introduced by the main polarizabilities α_k. These values were

---

*) The cavity radius determined by BÖTTCHER is close to the molecular radius.

**) In order to get an estimate, let us consider one example:
For Pentane, the value of P (from the Clausius-Mosotti equation) is $P(30°C)=25.30$, and $P(30°C)-P(-90°C)=0.26$.
For an error of 0.1% in ε we get an error of 0.05 in P, which is a 20% relative error.
If we compare the value of P (Clausius-Mosotti) with P (theor.) at one temperature, a large uncertainty arises from the model parameters adopted: The relative values of the α_k are certainly not more accurate than 2%, and the absolute values are even less accurate. The value of the cavity volume is not better known than within 20% accuracy.
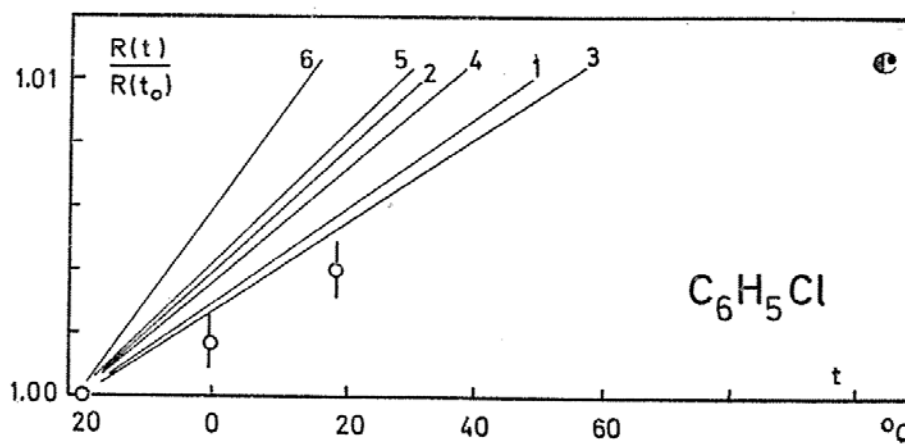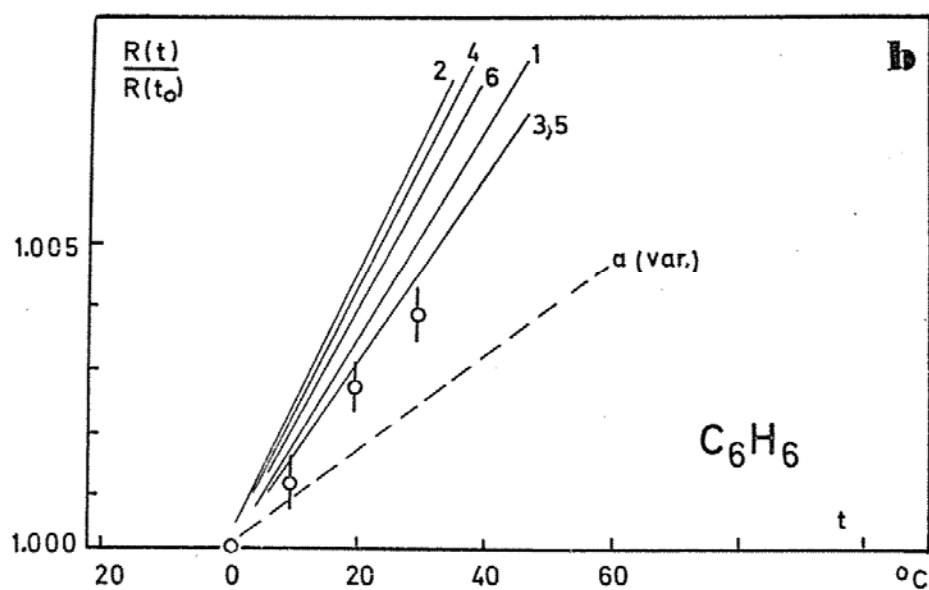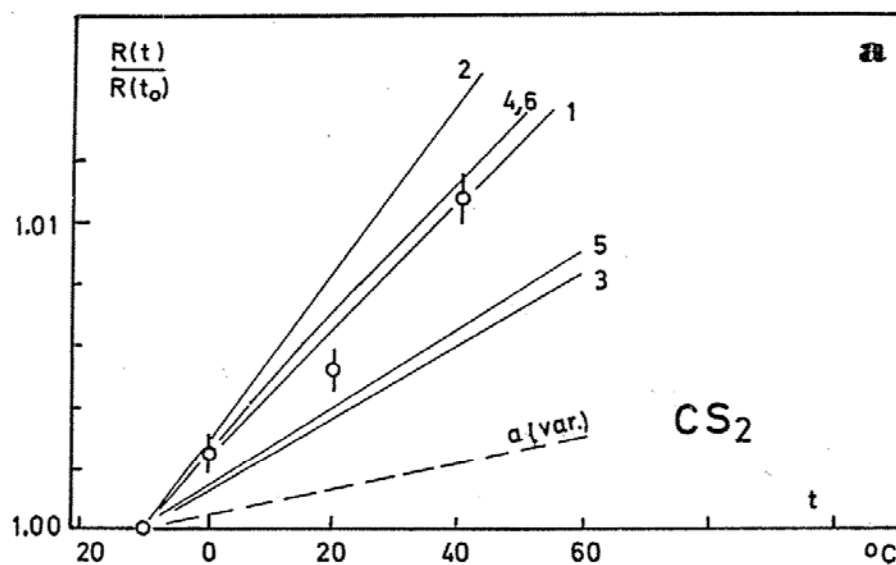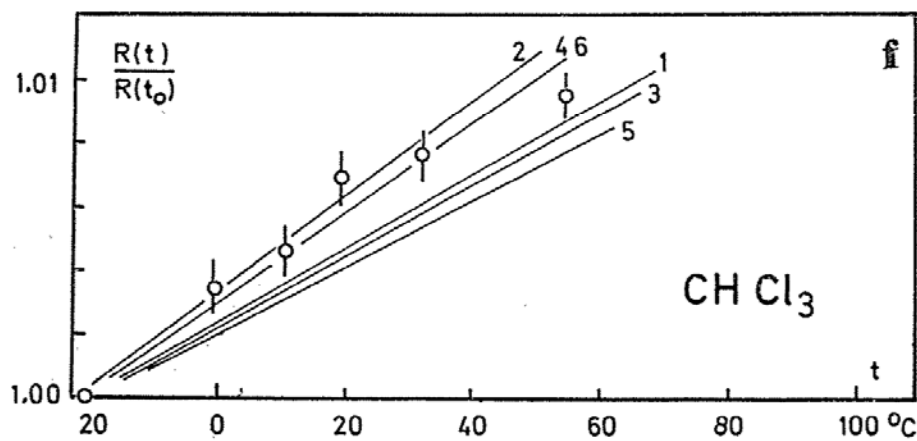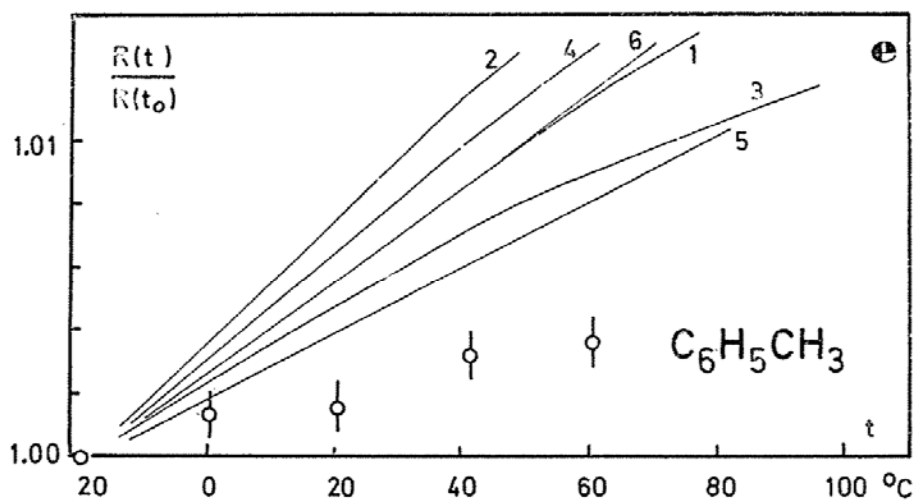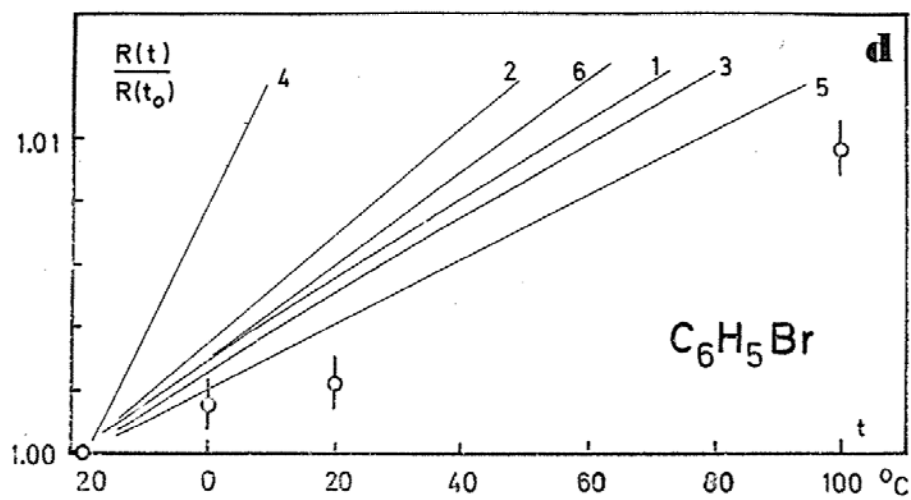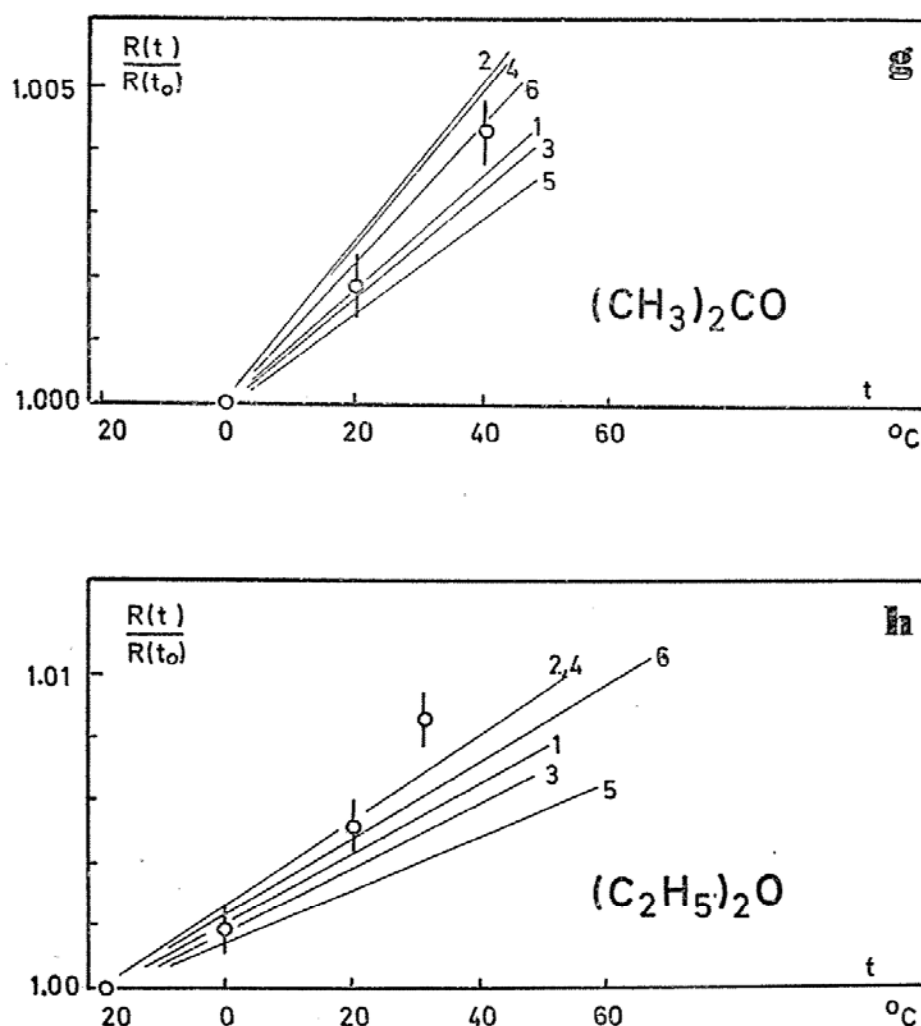
Fig. 1. a–h. Relative molar refraction $\dfrac{R(t)}{R(t_0)}$ of some pure organic liquids.
Curves No. 1–6: Theoretical predictions by eqs. (2–12), (3–12).
Experimental Points: Values given by the Lorentz-Lorenz equation.

published by STUART[15,16]. They should be considered as constants of the free molecule. Unfortunately, however, this is not always ensured, as can be seen by a close inspection of the tables.*)

---

*) This can be proved by comparing the optical anisotropy $\delta^2 = \sum(\alpha_k - \alpha_j)^2/(\sum\alpha_k)^2$ calculated from the tabulated values of the α_k with the value of δ^2 derived from the measurement of the depolarization ratio of scattered light in gases.

The reason for the discrepancy lies in the fact, that in many cases the α_k have been gathered from measurements on the liquid state. The deviation of α_k (gas) from α_k (liq.) may be as large as 10%, while the mean polarizability $(\sum\alpha_k)/3$ is only slightly affected.

The other parameters used in the calculations are chosen in the following way: The cavity radius a, first as equal to r_1, given by

(4-1) $\dfrac{4\pi}{3} r_1^3 = \dfrac{1}{N_A} \dfrac{M}{\rho} \cdot f$ ($f=0.74$ is the "filling factor")

or, secondly, as equal to r_2, given by

(4-2) $\dfrac{4\pi}{3} r_2^3 = \dfrac{1}{N_A} \dfrac{M}{\rho}$

Three different sets of depolarization factors D_k are chosen: the first, as it is used by other authors (indicated by the references), the second with other values closer to 1/3, and the third with $D_k=$ 1/3 (spherical cavity).

Table 1 surveys the molecular parameters used in the calculations, the results of which are represented by the curves No. 1–6 of the diagrams. For R(ellipsoidal) eq. (3–12) is used (curves No. 1–4), and for R(spherical)*) eq. (2–12) is used to give the curves No. 5 and No. 6. The last three columns give the absolute value of $R(t)$ by (3–12), $R_L(t)$ from the Lorentz-Lorenz equation and the temperature t (°C). For CS_2 and C_6H_6 values of R(ELL) are also calculated using the "Onsager relation" (1–1) which considers a^3 strictly dependent on the density. The resulting curves are designated by "a(var.)". As can be seen, these values are far too low. Using the same procedure for R(SPH), we obtain decreasing values for increasing temperature. (The results are not shown in the diagrams). We conclude then that the temperature dependence of the molar refraction (including the effect of volume expansion) is entirely accounted for by the experimental values of the refractive index $n(t)$.

In the case of the non-aromatic compounds the results No. 5 and 6 (for R(SPH)) are generally good and No. 6 fits always better than No. 5 (larger cavity radius). The predicted values of R(ELL) are best for Nos. 2 and 4, and are as good as No. 6. The effect of assuming different depolarization factors D_k is not large, but the difference caused by the different cavity radii is more important.

For the aromatic compounds we find bad agreement between the

---

*) Written henceforth as R(ELL) and R(SPH) respectively.

Table 1. Different sets of model parameters

Molecule $\alpha_k \cdot 10^{24}$	No	D_1	D_2	D_3	Ref	a^3 $(\cdot 10^{24})$	$R(t)$	$R_L(t)$	t °C
CS_2	1 }	0.174	0.413	0.413	(10)	17	22.49	21.27	-10
	2 }					23	20.71		
$\alpha_1 = 15.14$	3 }	0.24	0.38	0.38		17	24.54		
	4 }					23	22.06		
$\alpha_2 = 5.54$	5 }	1/3	1/3	1/3		17	24.42		
$\alpha_3 = 5.54$	6 }					23	22.24		
C_6H_6	1 }	0.174	0.652	0.174	(10)	25	25.36	26.12	0
	2 }					35	24.25		
$\alpha_1 = 12.3$	3 }	0.24	0.52	0.24		25	26.41		
	4 }					35	24.96		
$\alpha_2 = 6.3$	5 }	1/3	1/3	1/3		25	27.63		
$\alpha_3 = 12.3$	6 }					35	25.88		
C_6H_5Cl	1 }	0.26	0.55	0.19	(8) (10)	30	26.10	31.00	-20
	2 }					40	28.94		
$\alpha_1 = 13.2$	3 }	0.30	0.50	0.20		30	31.10		
	4 }					40	29.53		
$\alpha_2 = 7.6$	5 }	1/3	1/3	1/3		30	32.47		
$\alpha_3 = 15.9$	6 }					40	30.56		
C_6H_5Br	1 }	0.30	0.50	0.20	(8)	32	34.70	33.85	-20
	2 }					42	32.87		
$\alpha_1 = 12.8$	3 }	0.30	0.45	0.25		32	34.69		
	4 }					42	32.40		
$\alpha_2 = 10.1$	5 }	1/3	1/3	1/3		32	36.29		
$\alpha_3 = 17.8$	6 }					42	34.10		
$C_6H_5CH_3$	1 }	0.30	0.50	0.20	(8)	32	30.87	30.74	-20
	2 }					42	29.54		
$\alpha_1 = 13.6$	3 }	0.32	0.40	0.28		32	31.97		
	4 }					42	30.38		
$\alpha_2 = 7.4$	5 }	1/3	1/3	1/3		32	32.31		
$\alpha_3 = 15.6$	6 }					42	30.73		

$CHCl_3$	1	0.46	0.27	0.27	(8)	24	21.15	20.87	-20
	2				(10)	31	20.39		
$\alpha_1 = 6.7$	3	0.40	0.30	0.30		24	21.31		
	4					31	20.52		
$\alpha_2 = 9.0$	5	1/3	1/3	1/3		24	21.45		
$\alpha_3 = 9.0$	6					31	20.63		
$(C_2H_5)_2O$	1	0.20	0.41	0.39		30	22.?7	22.55	-19
	2					40	21.66		
$\alpha_1 = 11.3$	3	0.25	0.39	0.36		30	22.45		
	4					40	21.85		
$\alpha_2 = 7.1$	5	1/3	1/3	1/3		30	23.54		
$\alpha_3 = 7.9$	6					40	22.81		
$(CH_3)_2CO$	1	0.25	0.25	0.5		21	16.38	16.14	0
	2					29	15.88		
$\alpha_1 = 7.1$	3	0.28	0.28	0.44		21	16.50		
	4					29	15.96		
$\alpha_2 = 7.1$	5	1/3	1/3	1/3		21	16.50		
$\alpha_3 = 4.8$	6					29	15.94		

experimental and the theoretical values of R for all calculations. Nevertheless, optimal agreement is found for No. 1, No. 3 and No. 5 (the smaller cavity radius).

The usefulness of the Onsager formulas with spherical cavity, eq. (2–12) and eq. (2–11), (molar polarization for non-polar molecules) is also established in the work of LE FEVRE and RAO[10], which shows clearly that there is no improvement by assuming an ellipsoidal cavity (see Table 2 of their work). Obviously, the molar refraction and, for non-polar molecules, the molar polarization is nearly unaffected by the molecular anisotropy so that by this kind of investigation no conclusion can be drawn concerning the degree of usefulness of the different models.

Yet one interesting fact revealed by our diagrams is the total disagreement for the aromatic compounds. The slope of the relative molar refraction is overestimated for all sets of model parameters. We conclude therefore that for the aromatic compounds the molar

refractions in the liquid state are in fact larger than the values predicted by any Onsager model. This means that short range interactions are present which influence the "effective mean polarization" α in the liquid state.

Considering the theoretical and experimental values $R(t)$ and $R_L(t)$ of table 1, we should keep in mind that R depends strongly on the α_k which might not be very accurate. In spite of this, the table reveals a regularity showing best values of R for No. 1 or 3 (with the exception of CS_2, No. 2). This means best results for the smaller cavity radius, eq. (4-1). On the other hand, for $R(SPH)$ best agreement is attained by use of the larger radius eq. (4-2). This is in accordance with the fact mentioned above, stating the best fit for curve No. 6.

The usefulness of the larger radius of a spherical cavity can be made plausible in the following way: Let us visualize an aggregate of regularly distributed molecules with their spherical cavities in two dimensions as shown in Fig. 2.

The shaded circles represent the self-volume of the molecules, having a radius r_M. The spherical volume available for one molecule is indicated by the dashed circle and has the radius

(4-3) $r_3 = 2r_1 - r_M$

where r_1 is given by eq. (4-1). In the limiting case of "no free volume", we have $r_3 = r_M$, and, for the other extreme of "large free volume" (e. g. for gases), we have $r_M \ll r_1$ and hence $r_3 = 2r_1$.

If we calculate r_3 for liquid CS_2 at 20°C, and compare this value with r_2 according to eq. (4-2), we obtain the result

$$r_M = 2.50\text{Å}, \quad r_2 = 2.88\text{Å}, \quad r_3 = 2.85\text{Å}.$$

The value of r_M is based upon the known data of nuclear distance C—S=1.56Å, Van der Waal's radius of S=1.85Å, and assuming a cylindrical molecular volume with radius 1.85Å and length 6.25Å. The result explains clearly the successful application of r_2 to cavity radius.

Now we consider the polarization of polar molecules. Previous attempts to predict the dipole moment μ_0 of the free molecule by
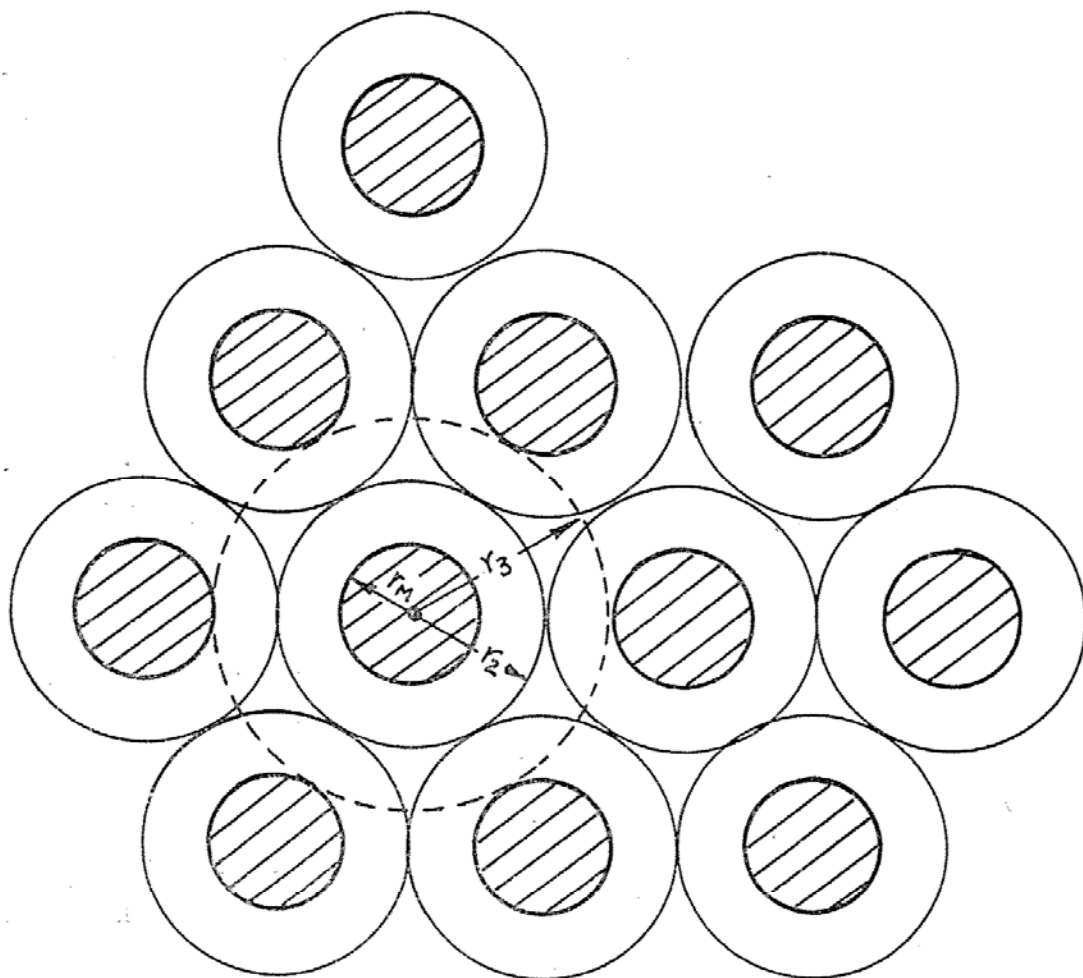
Fig. 2. Schematic two-dimensional representation of a symmetric arrangement of spherical molecules in the liquid state with free volume >0.

using the Onsager-Scholte formalism have been reported at the beginning of this chapter. Similar calculations, but using the Onsager formula with spherical cavity have been made by BÖTTCHER[17], who compared μ_0 with the calculated value of μ for 31 pure organic liquids. Good agreement was attained in several cases but, in the same way as mentioned before, objections can be raised concerning the accuracy of the experimental data and the uncertainty of model parameters so that the reported results are generally not very conclusive. In comparison, however, with the study of the molar refraction (or, for non-polar molecules, the molar polarization), the calculated dipole moment μ will strongly depend on the model parameters because in the formulas it appears as multiplied with the

factor $(1-f\alpha)^{-2}$ or $(1-f\alpha)^{-3}$ (see eqs. (2-10), (2-14)). Moreover, for ellipsoidal cavity (see eq. (3-10)) the electrical anisotropy of the molecule will influence the result sensibly.

In the following, model calculations are carried out using equ. (3-10) for the three molecules $CHCl_3$, C_6H_5Cl, $C_6H_5CH_3$. Table 2 represents the different sets of model parameters used in the calculations of μ. The polarizabilites α_k^0 to be used in our formula are the "electrical polarizabilities". According to a suggestion of GANS[18] they are connected with the "optical polarizabilities" α_k through the relation

(4-4) $$\frac{\alpha_k^0}{\alpha_k} = \frac{P_D}{R},$$

where R is the molar refraction which equals the electric polarization

Table 2. Molecular parameters

Molecule	No.	α_1	α_2 ($\cdot 10^{24}$)	α_3	D_1	D_2	D_3	a^3 ($\cdot 10^{24}$)	μ [D]
$CH\,Cl_3$	1							24	0.250
	2				0.46	0.27	0.27	31	0.852
$\mu_0 = 1.02$	3	8.33	11.25	11.25				24	0.758
$\varepsilon = 4.80$	4				0.40	0.30	0 30	31	0.925
$\rho = 1.490$	5	6.68	9.01	9.01				24	0.899
$t = 20°C$	6				0.46	0.27	0.27	31	1.025
C_6H_5Cl	1							30	1.32
	2				0.26	0.55	0.19	40	1.31
$\mu_0 = 1.71$	3	13.50	7.73	16.25				30	1.28
$\varepsilon = 5.475$	4				0.30	0.50	0.20	40	1.48
$\rho = 1.096$	5	13.24	7.58	15.93				30	1.36
$t = 29°C$	6				0.26	0.55	0.19	40	1.54
$C_6H_5CH_3$	1							32	0.221
	2				0.30	0.51	0.19	42	0.346
$\mu_0 = 0.37$	3	14.20	7.79	16.30				32	0.043
$\varepsilon = 2.3821$	4				0.32	0.40	0.28	42	0.249
$\rho = 0.866$	5	13.66	7.48	15.64				32	0.330
$t = 20°C$	6				0.30	0.51	0.19	42	0.427

P_E, and $P_D = P_A + P_E$ is the "distortion polarization", with $P_A =$ "atomic polarization". The values of P_E and P_A are taken from the tables of LANDOLT and BÖRNSTEIN[16]. The electric polarizabilities thus calculated are used in the calculations Nos. 1–4. In No. 5 and 6 the optical polarizabilities are used. Although in the latter cases better results are obtained, this should not be considered significant. We see that an increase of the cavity radius and values of D_k closer to 1/3 both increase the calculated value of μ. But, although using the larger cavity radius, the dipole moment in Nos. 2 and 4 turns out to be considerably lower than the true value. The deviations are 10%, 13%, 6% for the three molecules repectively, and may well be considered to exceed the experimental errors.

The agreement could certainly be improved by approximating the case of a spherical cavity. This method, however, is not realistic and should be abandoned, thus leaving us with too low values of μ in all cases. As a consequence of this we have to assume that the experimental value of ε is lower than the value needed to lead to the correct dipole moment μ_0. The physical reason for this must be sought in clustered molecules which form aggregates having a finite lifetime so that the average effective dipole moment μ_{liq}. of the molecules in the liquid state is smaller than μ_0. A further investigation of this problem is intended by the author.

b)   The Kerr constant.

The corrected value for the Kerr constant derived here (eq. (3–19)) and by RAO[8] has been examined by the latter author who compared the theoretically derived Kerr constant with the experimental value for several organic liquids. Although some improvement is gained compared with the results derived with the uncorrected formula, the method seems not stringent enough for a test of the validity of the new formula. Quite similar to the situation pointed out in section a), the errors of experimental data*) and the uncertainty of the model parameters may disguise the improvement expected by a particular model or may even lead into the wrong direction. At present, we

---

*) The accuracy of the experimentally determined Kerr constant is even worse than that of ε, P and μ_0.

omit therefore a critical interpretation of the previous results found in the literature. We merely discuss here some aspects of the new Kerr formula in connection with related problems.

1. In the old theory of the Kerr constant, the anisotropy term can be simply written as

$$\theta_A = \frac{1}{45\,kT}\,\frac{n_\infty^2-1}{n^2-1}\cdot\sum_{i<k}(\alpha_i-\alpha_k)^2, \quad \text{(see STUART[15])}$$

which uses Gans' relation (4-4) with

(4-6) $\qquad \dfrac{P_D}{R} = \dfrac{n_\infty^2-1}{n^2-1}$

where n_∞ is the refractive index including the infrared contribution extrapolated to infinite wavelength, and n is the optical refractive index. The "optical anisotropy" is defined by

(4-7) $\qquad \delta^2 = \sum_{i<k}(\alpha_i-\alpha_k)^2/(\sum\alpha_k)^2$

and is connected with the depolarization ratio Δ of scattered light through the relation

(4-8) $\qquad \Delta = \dfrac{6\delta^2}{10r+7\delta^2}, \quad r=RT\beta\dfrac{N}{N_A}, \quad \text{(see, e. g. STUART[15]).}$

There exists therefore a relation between θ_A and Δ which was first discovered by GANS[19] and which may be written as

(4-9) $\qquad K_1 = \dfrac{3}{8}\beta\dfrac{(n^2-1)(\varepsilon-1)}{\pi n^2}\cdot e^2\cdot\dfrac{\Delta}{6-7\Delta}$

where e is the ratio of the effective field divided by the external field (in the most simple case assumed to be the Lorentz-field), and K_1 means that part of the Kerr constant given by θ_A. With the corrected formula of the Kerr constant, it is obvious that this simple relation can no longer be established.*)

2. A dispersion law of the depolarization ratio of scattered light in liquids has been derived stating that

(4-10) $\qquad \dfrac{\Delta}{6-7\Delta} = \text{const}\cdot\dfrac{n^2-1}{n^2+2}, \quad \text{(see CABANNES[20]).}$

---

*) This has also been pointed out by STUART[22] who does not give a definite reason for this suggestion.

This is easily derived from Gans' formula (4-9) with his assumption

(4-11) $e^2 = \dfrac{(n^2+2)(\varepsilon+2)}{9}$,

and using the HAVELOCK—law[21] of the dispersion of the Kerr constant:

(4-12) $\dfrac{n^2 K}{(n^2-1)^2} = \text{const.}$

It should be recognized that eq. (4-10) does not take into account the corrections introduced into the Kerr constant and therefore needs also to be corrected. A new careful examination of the disperson of the depolarization of scattered light could be a useful supplement in the investigation of the theory of the Kerr constant outlined above.

5. SUMMARY

The results of the present investigation can be summarized as follows:

1. If we take into account the interaction of the induced dipole moment with the effective field, the correction of the Onsager formulas for anisotropic molecules leads to new formulas for the polarization and the Kerr constant. For non-polar molecules, the polarization is not affected by the new interaction term but, for polar molecules the factor of the dipole moment is modified.

2. For a number of pure organic liquids the molar refraction has been investigated by systematic model calculations, varying the different model parameters within reasonable limits. It turned out that for the molar refraction and, in case of non-polar molecules, for the molar polarization the predictions are the same no matter if spherical or ellipsoidal cavities are assumed. For the aromatic compounds the theoretical values of the molar refraction are always larger than the experimental ones.

3. For three polar molecules the dipole moment has been investigated by systematic model calculations similar to those described before. All sets of parameters chosen lead to predicted values of μ

smaller than the dipole moment of the free molecule. This disagreement can probably be explained by interactions of clustered molecules in the liquid state.

4. As a consequence of the corrected formula of the Kerr constant, the formulas of the older theory connecting the Kerr constant with the depolarization ratio of scattered light are considered to be inadequate from the present point of view.

REFERENCES

(1) J. G. Kirkwood, *J. Chem. Phys.* **7** 911 (1939); *Ann.New York Acad. Sci.* **40** 315 (1940).

(2) H. Fröhlich, *Theory of Dielectrics* Oxford, (1958).

(3) L. Onsager, *J. Am. Chem. Soc.* **58** 1486 (1936), **64** 1238 (1942); *J. Phys. Chem.* **43** 189 (1939).

(4) T. G. Scholte, *Physica* **15** 437 (1949).

(5) P. Debye, *Phys. Z.* **13** 97 (1912); *Verh. dtsch. phys. Ges.* **15** 777 (1913).

(6) D. A. A. S. Narayana Rao, *Acta Phys. Polon.* **A37** 161 (1970).

(7) J. A. Osborn, *Phys. Rev.* **67** 351 (1945).

(8) D. A. A. S. Narayana Rao, *Trans. Faraday Soc.* **54** 954 (1958).

(9) J. A. Abbott and H. C. Bolton, *Trans. Faraday Soc.* **48** 422 (1952).

(10) R. J. W. Le Fevre and D. A. A. S. Narayana Rao, *Austr. J. Chem.* **8** 329 (1955).

(11) C. J. F. Böttcher, *Physica* **9** 945 (1942)

(12) Handbook of Chemistry and Physics, The Chemical Rubber Co., 1968.

(13) Landolt—Börnstein, *Physikalisch-Chemische Tabellen*, Springer Verlag, (1923), II. Band.

(14) International Critical Tables of Numerical Data, Physics, Chemistry and Technology, Mc Graw Hill, New York 1926–33.

(15) H. A. Stuart: *Molekülstruktur*, Springer-Verlag (1967).

(16) Landolt—Börnstein, *Zahlenwerte und Funktionen*, Springer-Verlag (1951), I. Band, 3. Teil.

(17) C. J. F. Böttcher, *Physica* **6** 59 (1939).

(18) R. Gans, *Ann. Phys.* **65** 97 (1921).

(19) R. Gans, *Z. Phys.* **17** 353 (1923).

(20) J. Cabannes: *La Diffusion Moleculaire de la Lumiere*, Paris (1929).

(21) T. H. Havelock, *Proc. Roy. Soc.* (Lond.) **84** 28 (1908).

(22) H. A. Stuart, *Molekülstruktur*, Springer-Verlag (1967), p. 409.

"The scholar must keep himself free from stain. He does not go among the low to make himself high. He does not seek out the foolish to make himself seem wise. He does not praise those who think as he does, or condemn those who differ."

CONFUCIUS: The Book of Rites, 500 B. C.

UNDERGROUND WATER RESEARCH IN TAIWAN

H. W. Scharpenseel*, F. Pietig*, E. Kruse* and
H. Hesselfeld svd**, K. Specht svd***

INTRODUCTION

The island of Taiwan, having an area of 35,834 km², is 395 km long (N to S), and 123 km wide (E to W). It was named Formosa, "the beautiful", by 16th century Portuguese discoverers, like the district "Formosa" in the Gran Chaco of North Argentine which bears the same name but has an area of 74,535 km² and is more than twice as big. The inhabitants of the island, now numbering more than 15 million, prefer the name "Taiwan".

The distance between Taiwan and the Chinese mainland is 170 km. Taiwan looks like a tilted block, where 2/3 of the area is covered by mountainous landscape rising up to 4,000 meters, (Mount Morrison 3,950 m).

The N-S watershed divide is in the eastern part of the island and descends steeply towards the Pacific Ocean. In the westerly direction, from the dividing ridge a sequence of terraces leads to the coastal plain. This plain is stretched out extensively towards the Taiwan Strait of the Chinese Sea. Between the high mountain ridge and the prominent range of mountains along the western shore, a trough about 140 km long and 9 to 18 km broad forms the "Taitung Rift Valley".

Much of the surface of Taiwan is wooded, forests covering about 50% of the area, and contains great amounts of commercial timber, like the much-demanded camphor tree. This timber cover provides an excellent protection against erosion from mountain slopes and hillsides. Of the remaining agricultural surface area, about 68% is used for growing rice, sweet potatoes, and sugar cane, and to a smaller extent

* Institut für Bodenkunde der Universität Bonn, 53 Bonn, Nussallee 13, West-Germany
** Department of Physics, Fu Jen University
*** Department of Chemistry, Fu Jen University

for growing wheat, soy beans, peanuts, fruit and tobacco.

The climate is subtropical with a long summer, somewhat softened by the surrounding ocean, and with a short and mild winter. Practically there is no interruption of growth of crops, and in some areas there are two or even three harvests each year.

Like the whole South-East Asiatic island territory, Taiwan is also of cenozoic origin. Almost all of its population lives in the coastal plains. High mountain territories form the backward areas inhabited by aborigines of Malaysian origin.

PROBLEM

Because of the intensive agricultural usage, the colluvial and alluvial lands of the coastal plains have been deprived of carbonates and plant nutrient elements. In order to keep up crop yields and agricultural productivity, a high amount of fertilizing is needed every year. Also, in spite of the annual rainfall, which in most areas is more than 1,000 mm, an extra amount of irrigation is necessary for rice fields and sugar cane. One reason for this is that the western coastal regions are partly lying in the region of rain shadow against the N—E monsoons.

Figure 1 shows the climate zones of Taiwan according to Walter and Lieth[1]. The lower regions are influenced by the Koppen-climate types I and II, and to a lesser extent by climate type V, whereas the central highlands are dominated by the mountain-climate type X.

Although the coastal areas are rich in underground water due to the high rainfall and due to the extensive downflow from the central mountains, the measurements during the last two decades report a marked lowering of the surface level in the coastal districts. This is due to heavy water consumption by industry and agricultural watering systems. Similarly alarming is the decrease of the ground water level observed in wells and piezometric tubes.

These coastal areas are covered by blankets of recent, pleistocene, plio-pleistocene, and mio-pliozene sediments (Fig. 2), stretched out in front of the old-tertiary, mesozoic and paleozoic rock formations of the central highlands[2]. The mountain range north of Taipei
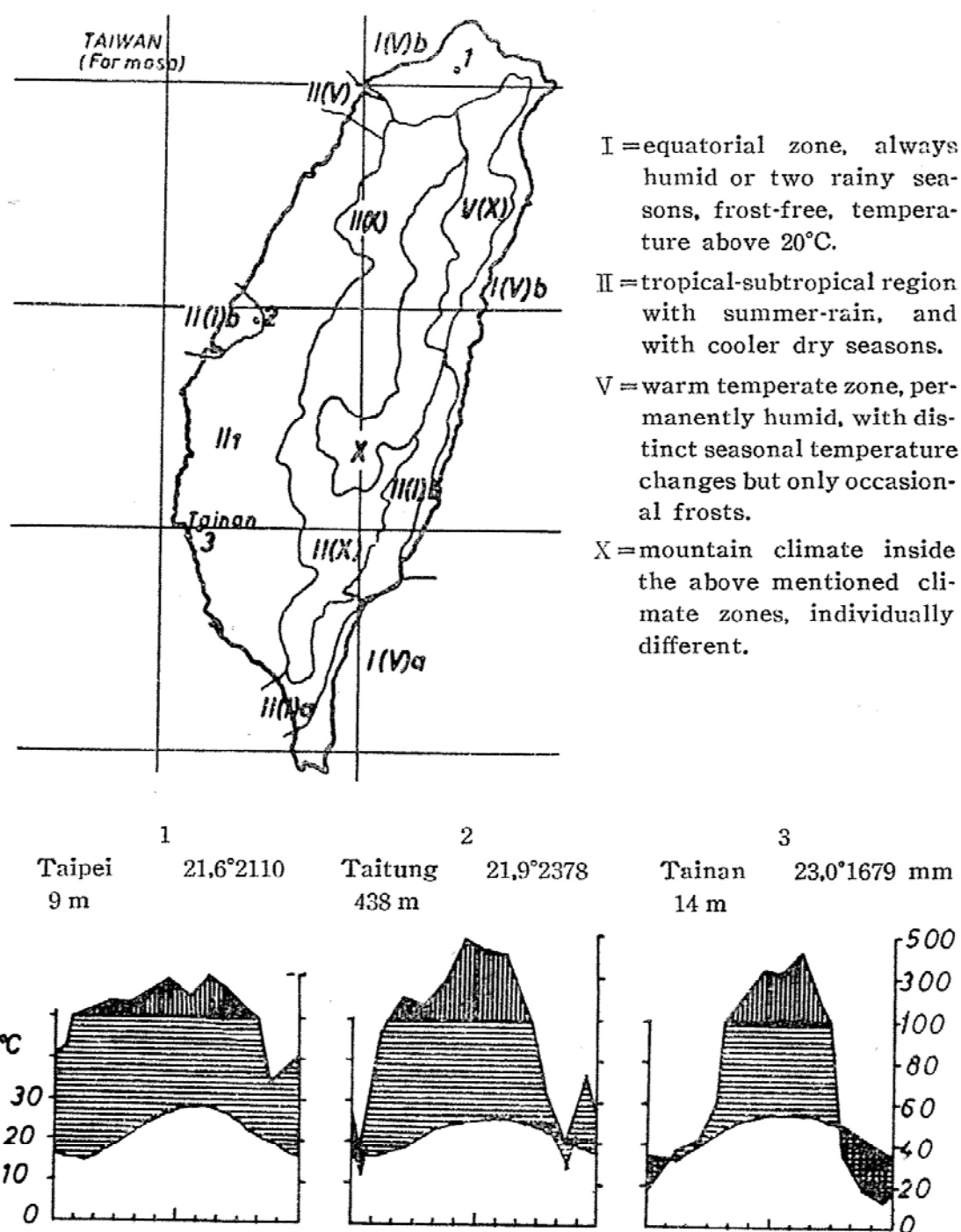
I = equatorial zone, always humid or two rainy seasons, frost-free, temperature above 20°C.

II = tropical-subtropical region with summer-rain, and with cooler dry seasons.

V = warm temperate zone, permanently humid, with distinct seasonal temperature changes but only occasional frosts.

X = mountain climate inside the above mentioned climate zones, individually different.

1		2		3	
Taipei	21,6°2110	Taitung	21,9°2378	Tainan	23,0°1679 mm
9 m		438 m		14 m	

Fig. 1. Chart of climates in Taiwan according to Walter and Lieth, as well as precipitation—temperature diagrams of the three sampling regions.

consists of basic andesitic volcanites. Limited amounts of granite and gneiss are found to the north of Hualien, along the eastern coast.

The sediments of the coastal plains show a great variety of litho-facial differences. In the main rice district of northern Taiwan,

GEOLOGICAL SKETCH MAP
OF TAIWAN

EXPLANATION

10 ☐ Recent
9 ▦ Pleistocene
8 ▨ Plio-Pleistocene
7 ▧ Miocene & Pliocene
6 ▤ Eocene & Oligocene
5 ▨ Cretaceous (?)
4 ▥ Mesozoic(?) & Paleozoic
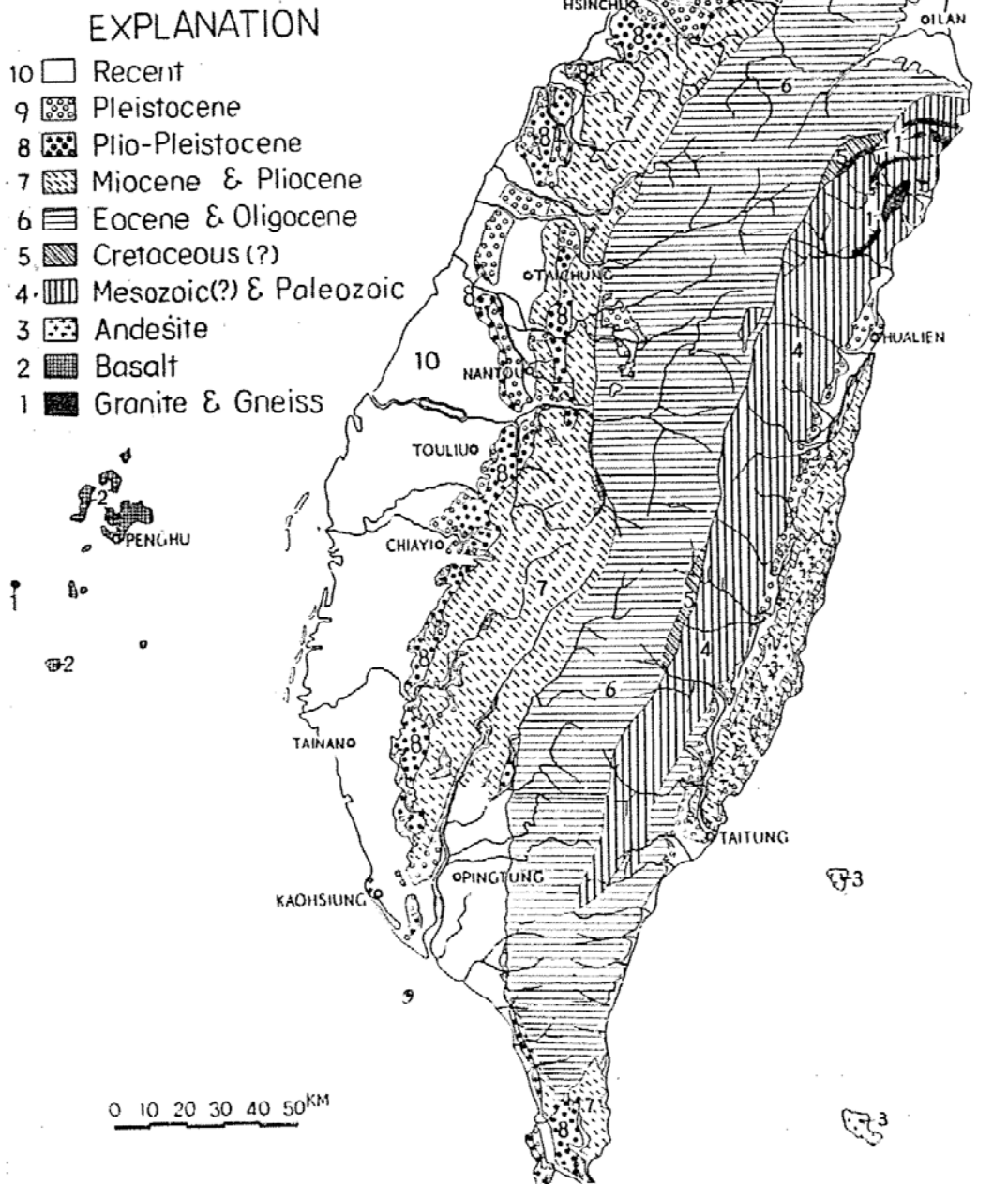3 ⦂ Andesite
2 ▦ Basalt
1 ▦ Granite & Gneiss

Fig. 2. Geological Sketch Map of Taiwan

nearly the whole surface is flooded for the two rice harvests until
the blossoming time. This causes an additional enormous water
consumption by evaporation (evapotranspiration). In southern parts

of the coastal plains, the growth of sugar cane, which requires an extensive irrigation system, also strains the water reserves of the island.

As a small contribution to studies of the hydro-geological and water-economy situation of Taiwan, the authors examined three specifically important areas of the coastal region of Taiwan, where the water consumption is very intensive. Altogether 84 ground water samples were taken from sufficiently accurately described springs and wells. These samples were tested for their natural C^{14} and H^3 concentrations[3]. The three sampling regions are as follows: first the basin of Taipei (predominantly growing rice), secondly the region between Taichung and Chiayi, bordered by the river Wu in the north and the pleistocene and plio-pleistocene sediments in the east (growing rice, peanuts, and other products), and thirdly the southern wedge-shaped coastal region between Tainan and south of Pingtung, between the northern Tsengwen river and the southern Kaoping river (sugar cane region) (Fig. 3).

The ground water samples were mixed with NaOH, some $FeSO_4$, $BaCl_2$, and a precipitating accelerator for collecting CO_2 and the carbonate as $BaCO_3$ (Fig. 4).

By inverting the 60 liter water flask and by inserting it in a ring, the precipitate could be collected into a smaller 1 liter screw cap flask without intermediate contact with the atmosphere. For measuring the tritium, 500 ml PVC flasks were adequate as sample containers if filled with water up to the rim and immediately screwed tightly in order to avoid exchange with the atmosphere.

Natural radiocarbon and tritium were integrated in synthetic benzene[3]. The specific activity of the carbon and tritium was measured in the liquid scintillation spectrometer and was expressed in radiocarbon-age, or tritium units (1 T.U.=10^{-18} T/H).

RESULTS

Table 1 shows the C^{14}—ages, tritium-concentrations, coordinates of the sampling spots, statements about the depth and static level of the ground water at the sampling stations, and the perforation depth
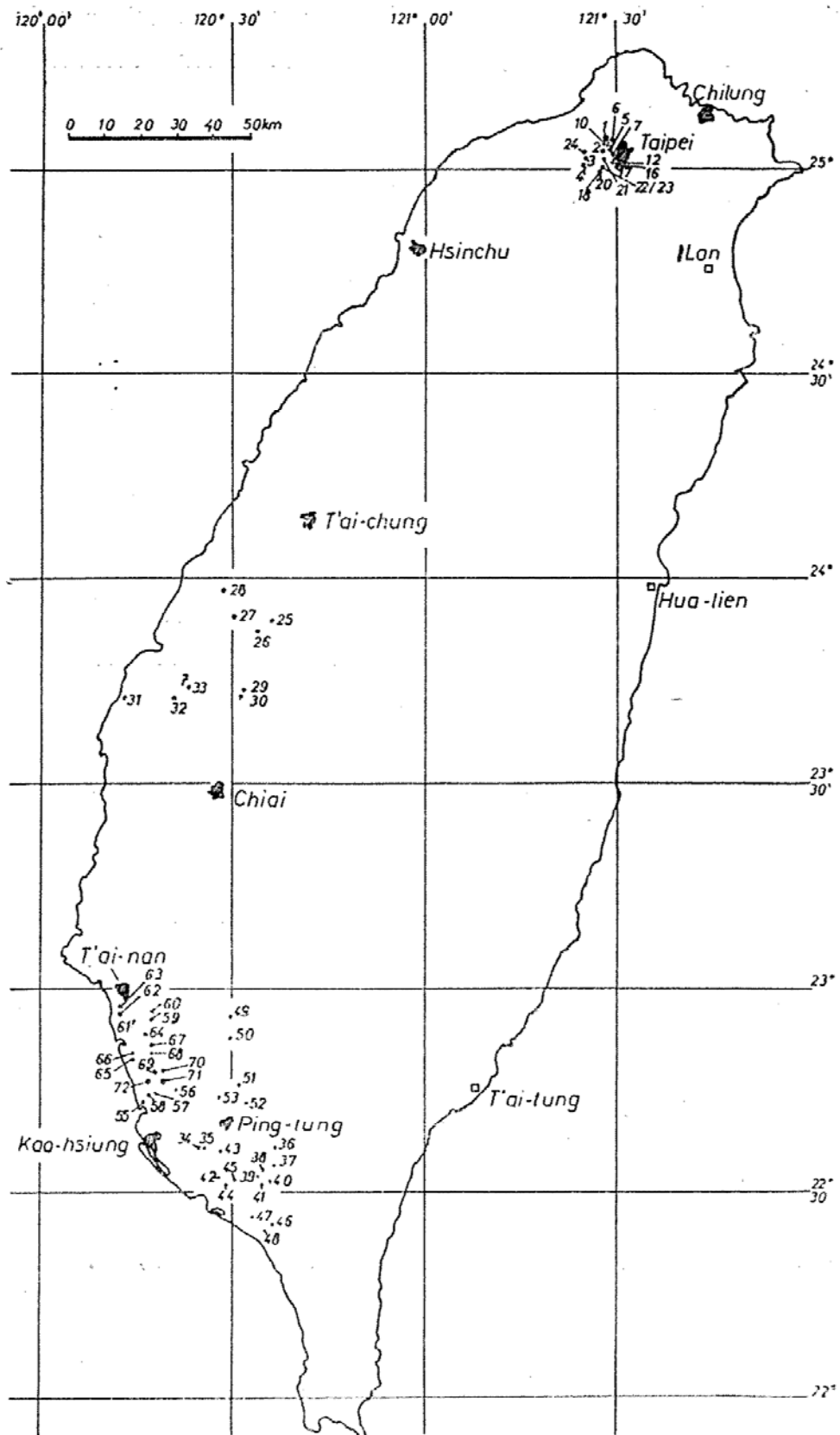
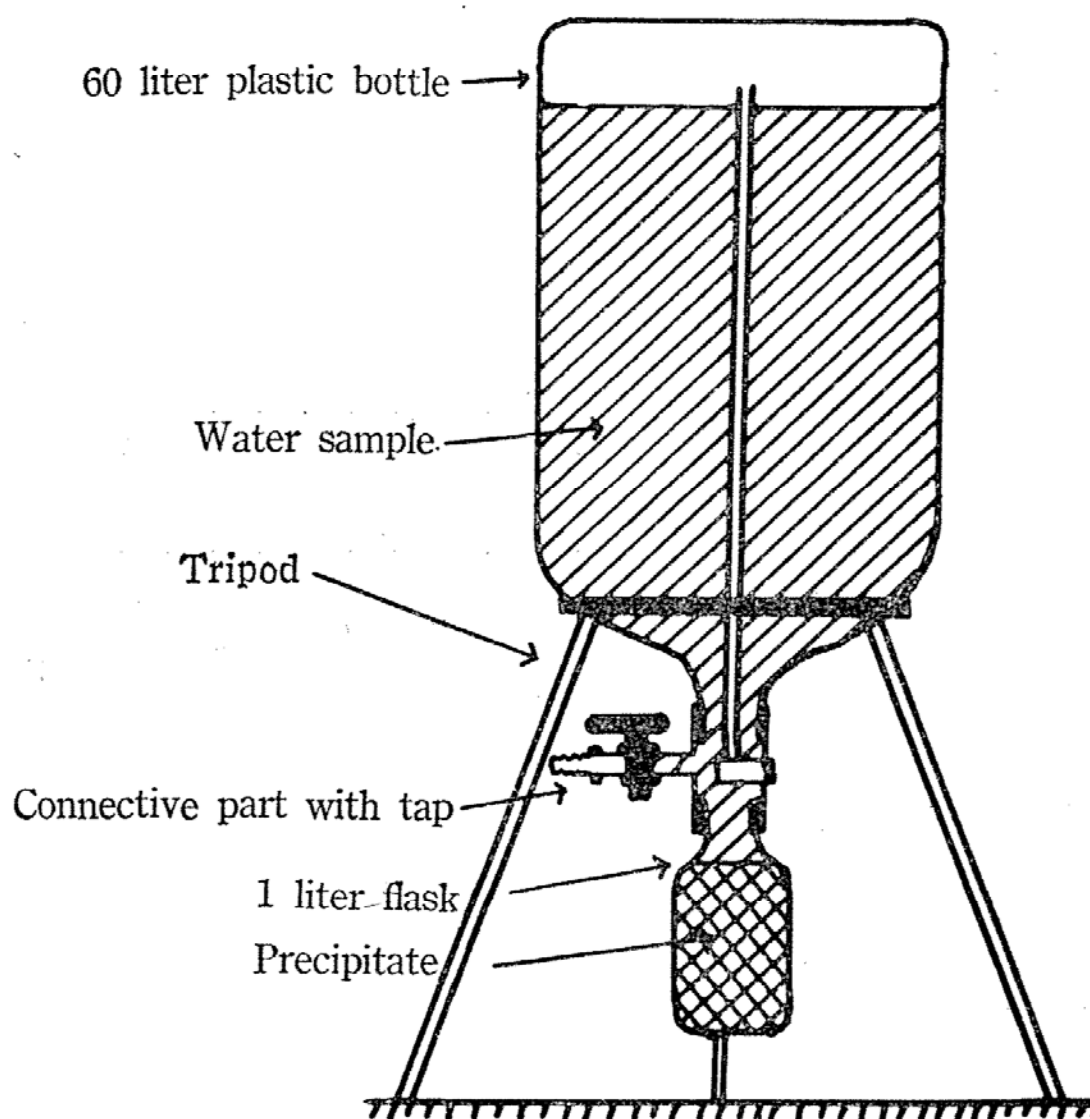Fig. 3.　Sampling stations in Taiwan (three regions)

Fig. 4. Precipitation of carbonates from ground water sample for C^{14} dating

of the wells at the sampling points. Figures 5 to 9 show the sampling stations on a large-scale map. They also show the measured carbon-ages of the three individual sampling regions. An attempt has been made to connect the sampling points by isochronic lines, wherever it was possible, due to concordance with the piezometrical lines and their direction. The flow velocity per year of the groundwater is found from the km-distance of the isochrones, divided by the time difference of the age thresholds represented by them. Short term changes, usually increasing flow velocities, occurring by formation of sink cones and by increased flow slopes due to a "sudden" increase

Table 1. Natural radiocarbon and tritium measurements in ground water samples

Sample No.	Sample name	Perforation (m)	Aquifer (m)	Coordinates of sampling spot	C^{14}-age	T. U.
1/1236	Taipei, W Tanshui river Textilwork, Formosa.		62–70	121°82'36", 25° 4'28",	18260±3220 (minute sample, questionable)	95±4
2/1237	Taipei, W Tanshui river, Foods Company,		63–82.5	121°28', 25° 2'59",	4680±90	130±3
3/1238	Taipei, W Tanshui river, Chem. Co.,		60–75	121°26'24", 25° 1'46",	6930±70	41±3
4/1239	Taipei, W Tanshui river, Wire Cable Factory,		47–69.5	121°26', 25° 0'41",	102.5±0.7% modern	143±3
5/1240	Ta Chiao (Kuo Hsiao),		56–74	121°30'15", 25° 3'50",	7120±150	40±3
6/1241	Yen Pirg,		52–63	121°30'10", 25° 4',	6830±180	113±3
7/1242	Ta Tung,		52–74	121°30'30", 25° 3'53",	6380±180	66±3
8/1243	Cheng Yi,			121°29' 7", 25° 4' 5",	6440±150	66±3
9/1244	Ta Tung Pei Lu,			121°29', 25° 3'48",	5030±120	57±4
10/1245	Hsin Te,			121°28'37", 25° 4' 2",	11380±230	33±4
11/1246	Kung 14,			121°28'55", 25° 4'21",	13200±340	59±3
12/1247	San Kuang,			121°29', 25° 3'18",	4160±130	59±4
13/1248	San Chung,			121°29'12", 25° 4'21",	9200±230	39±4
14/1249	Fu Te,			121°29'38", 25° 3'46",	4020±150	72±5
15/1250	Lung Men,			121°29'25", 25° 4'30",	9550±130	52±5
16/1251	Fu He,			121°29'40", 25° 1',	5350±110	23±5
17/1251a	Miao Wei,			121°29'45", 25° 0'20",	3880±90	58±3
18/1252	Electric Factory,		49–61	121°29'45", 25° 0' 8",	7340±190	62±3

19/1253	Textil Work,		43-61	121°28'16", 25° 4'12"	9330±160	44±4
20/1254	Water Works,		50-64	121°27'54", 25° 0'	3840±160	119±4
21/1255	New deep well of Water Works,		58-79	121°27'56", 25° 1'10"	4650±150	27±3
22/1256	Paper Mill Corpor.,		51-80	121°28' 8", 25° 0'45"	4990±270	52±5
23/1257	Paper Mill,		49-72	121°27'55", 25° 0'41"	4150±270	0
24/1258	Fu Jen University,			121°25'30", 25° 2'15"	8270±190	82±5
25/1259	Changhua, No. 68,		61.9	120°35'34", 23°53'21"	109.6±0.4% modern	88±5
26/1260	Changhua, No. 27,		61	120°33'17", 23°51'41"	2500±60	96±3
27/1261	Changhua, No. 49,		86	120°29'43", 23°53'48"	3410±80	26±4
28/1262	Changhua, No. 12,		140	120°27'56", 23°57'34"	4980±60	21±4
29/1263	Touliu, No. 383,		95 (42.5mH$_2$O)	120°31'42", 23°43'	2270±80	24±4
30/1264	Touliu, No. 403,		122 (24mH$_2$O)	120°31' 7", 23°42'27"	2260±70	22±4
31/1265	Touliu, No. 378,		215 (19mH$_2$O)	120°13' 3", 23°41'38"	2750±70	26±4
32/1266	Touliu, No. 370,		265 (21mH$_2$O)	120°20'38", 23°41'45"	5080±110	48±4
33/1267	Touliu, No. 401 (new well)		283 (28mH$_2$O)	120°21'36", 23°43'36"	5610±70	40±4
34/1268	Tainan/Pingtung, No. 18 Dar Liao	7.6-16.8	1.2-20	120°25' 3", 22°36'14"	100.5±0.5% modern	62±4
35/1269	Same location, Dar Liao,	6.1-27.4	30	120°25' 4", 22°26'14"	104.7±0.6% modern	66±4
36/1270	Tser San.	30.5-55 73.2-85.4	1-23, 26-90,	120°36'50", 22°36' 9"	880±90	88±5

No.	Name						
37/1271	Sin Tso 5111-1,	27.5-67	0-22.5, 27-67.5	120°36'28",	22°33'42",	350±70	61±4
38/1272	Si Lin 5113-5,	41.2-71.7	70.5	120°35'19",	22°32'52".	3110±90	62±5
39/1273	Lim Hou, 5114-3.	30.5-73.4	1.8-75	120°34'27".	22°32'19".	3270±70	119±5
40/1274	Wanlon 5113-7,	58-88.5	0.3-100	120°35'56".	22°31'15".	3350±90	138±5
41/1275	Nan An 5509-2,	18.3-70	1.5-69	120°34'46".	22°30'58".	3660±100	108±8
42/1276	Gun Tan Men 5104-1,	22-33.5	0.3-33	120°28' 3".	22°32' 6".	102.3±0.2% modern	85±5
43/1277	Wan Tan 5103-1,	74-116.7	7.5-128	120°28'24".	22°35'45".	7460±130	48±5
44/1278	Kan Din 5502-2,	109.7-143.2	110-143	120°29'14".	22°30'59".	7330±130	55±5
45/1279	Hou Pi Tso 5505-1,	104-134	102-132	120°30'40".	22°31'43".	6720±150	64±5
46/1280	Ta Hsiang Ying 5511-1,	42.8-73.3	9.6-75	120°36'36".	22°25'44".	1550±90	78±5
47/1281	Chan Lon 5510-5,	39.7-76.4	0.3-75	120°33'23".	22°26'53".	1820±130	57±4
48/1282	Tai Yuan No. 3,	42.7-73.2	1.2-75	120°35'10".	22°25' 1".	1410±100	44±3
49/1283	Yuan Tan Tsz 5207-1,	3.05-27.4	0.6-27	120°29'57".	22°55'32".	190±50	66±5
50/1284	Kin Cuar 5201-2,	54.9-79.3	1.2-23.5	120°29'43".	22°52'17".	4900±100	72±5
51/1285	Peng Tso 5101-1,	8.5-28.4 (8.5-8.7)*	1.5-31.2	120°31'00".	22°45'32".	490±60	56±4
52/1286	Tung Hai Fong 5105-5,	10.7-46.5	1.5-45	120°32'13".	22°42'51".	730±60	71±3
53/1287	Tson Lang 5102-1,	15.3-45.8	1.2-45.6	120°28'25".	22°43'20".	3190±70	72±4
54/1288	Jen Wu 123.	10-18, 25.3-29.3 30.4-33.6	2.4-17.4			530±70	68±4
55/1289	Hou Chin No. 17,	10.1-18.6	4.8-18	120°17' 2",	22°43'10".	2270±100	40±5
56/1290	Jong San Tru 25,	11-20. 20.5-27.5		120°22'16",	22°44'53".	2220±90	6±5

57/1291	East Chin Po, No. 17,	5.5-17.4	5.4-17	120°18'46", 22°44'17"	1100±80	62±5
58/1292	West Chin Po, No. 11,	9.2-30.5	1.0-30	120°18'11", 22°44'16"	2330±70	8±5
59/1293	South Salun, No. 14,	6.7-16.8	6-8.5, 10.5-16.5	120°17' 0", 22°55' 0"	101.1±0.3% modern	65±5
60/1294	North Salun, No. 28,	6.1-25.9	3-25.5	120°17', 22°56'	840±80	66±5
61/1295	Kui Jen, No. 11,	3.4-9.0, 9.8-26.8	3-6, 6.6-9	120°14', 22°55'	2620±80	31±5
62/1296	Hu Shan, No. 15,	3.2-13.3, (13.5-46.9)*	2-6.5	120°12', 22°56'	2480±80	56±5
63/1297	Hu Shan, No. 19,	6.1-53.4	3-55	120°12', 22°57'	2360±90	46±5
64/1298	Sin Yuan, No. 21,	7.9-31.7	7-31	120°16', 22°53'	4130±80	46±5
65/1299	Lu Tzu, No. 15,	8.9-25	25-33	120°14', 22°50'	1120±50	259±6
66/1300	Pen Chau, No. 19,	3-7, 9.5-17		120°15'19", 20°50'12"	1460±50	20±5
67/1701	Chiu Kui, No. 15,	11.6-23.5	11.4-23.5	120°18' 3", 22°51'17"	2240±60	29±5
68/1702	Chin Jon Tza, No. 19,	21.6-35.7	21.3-35	120°18' 4", 22°49'41"	3500±60	71±6
69/1703	Tiou Chi Lin, No. 15,	16.3-24.7	16-24.3	120°18'42", 22°47'32"	2400±50	8±5
70/1704	North Kun Sui, No. 17,	20.7-41.7	20.4-41.1	120°19'52", 22°47'33"	2340±60	39±5
71/1705	South Kun Sui, No. 18,	9.7-26.3	6.5-26	120°19'53", 22°46'28"	1800±70	57±5
72/1706	Pai Shou Tze, No. 14, 2520/222	14.7-23.8	14-27	120°17'34", 22°45'54"	1300±50	32±5
73/1707	Tainan, Wangliao No. 11	21.6-40.8	20-53		2480±70	59±5
74/1708	Tainan, Cheang No. 2,	99-104, 138-172 (64-82.4, 97.6-109.8, 125-129, 144.3-155.6)*	98-103, 102-168 (CO_2)		7930±80	14±4
75/1709	Taoyeh, No. 2,	122-173	123-170(CO_2)		9500±90	29±4

No.	Location				
76/1710	Kannai, No. 1,	132.2–186	126–83 (CO₂+H₂S)	11640±160	25±4
77/1711	Liufen Liao, No. 13,	4–7.3, 7.9–12.2, 13.7–17.1	4–7.2, 8.4–12, 13.5–15.8,	108.9±0.3% modern	49±5
78/1712	Tsengwen, No. 15,	4–14.4 (6.2–14.4)*	14.4	1250±70	335±6
79/1713	Sanhua, No. 11,	13.5–25.5 (13.4–25.6, 9.9–31.7)	13.5–18, 19.5–25.5	3080±70	95±6
80/1714	Chiapo, No. 13,	8.5–11.5, 27–31, 41–45, 57–78,	8–12, 27–31, 41–45, 57–83,	1530±60	43±5
81/1715	Fantzeliao, No. 13,	16.8–23.5, 66.2–90.9		4960±120	48±5
82/1716	Fantzeliao, No. 14,	23.8–29, 29.9–34, 47–71, 91.5–104	23.8–29, 29.9–34, 47–71, 91.5–104,	6930±170	13±4
83/1717	Shinhua, No. 12,	8–15, 26–39.5	8–15, 26–39.5	4540±80	19±4
84/1718	Chuochia, No. 13,	9–21 (10.5–22.5)*	8.5–21.8	1050±70	88±5

* Discrepancy between notes taken during sampling trip and additional information received later.

I 不固結岩層
Unconsolidated formations

| A4 | 地下水廣泛且豐富
Extensive and rich aquifers.

| A3 | 地下水廣泛,部份豐富
Extensive and local rich aquifers.

| A2 | 地下水部份豐富
Local rich aquifers.

| A1 | 局部有地下水
Local aquifers.

II 固結岩層
Consolidated formations

| B4 | 地下水較豐富
Rich aquifers.

| B3 | 地下水部份豐富 地下水源較深
Local rich aquifers, often in great depth.

| B2 | 地下水部份豐富,常形成泉水
Local rich aquifers, ultilization mainly by springs.

| B1 | 無地下水或極少地下水
Without or only with very local groundwater.

| B0 | 無地下水
Without groundwater.

地下水位
Groundwater table (El. in meter)

地下水流向
Flow direction of groundwater.

Fig. 5. Legend for regional maps
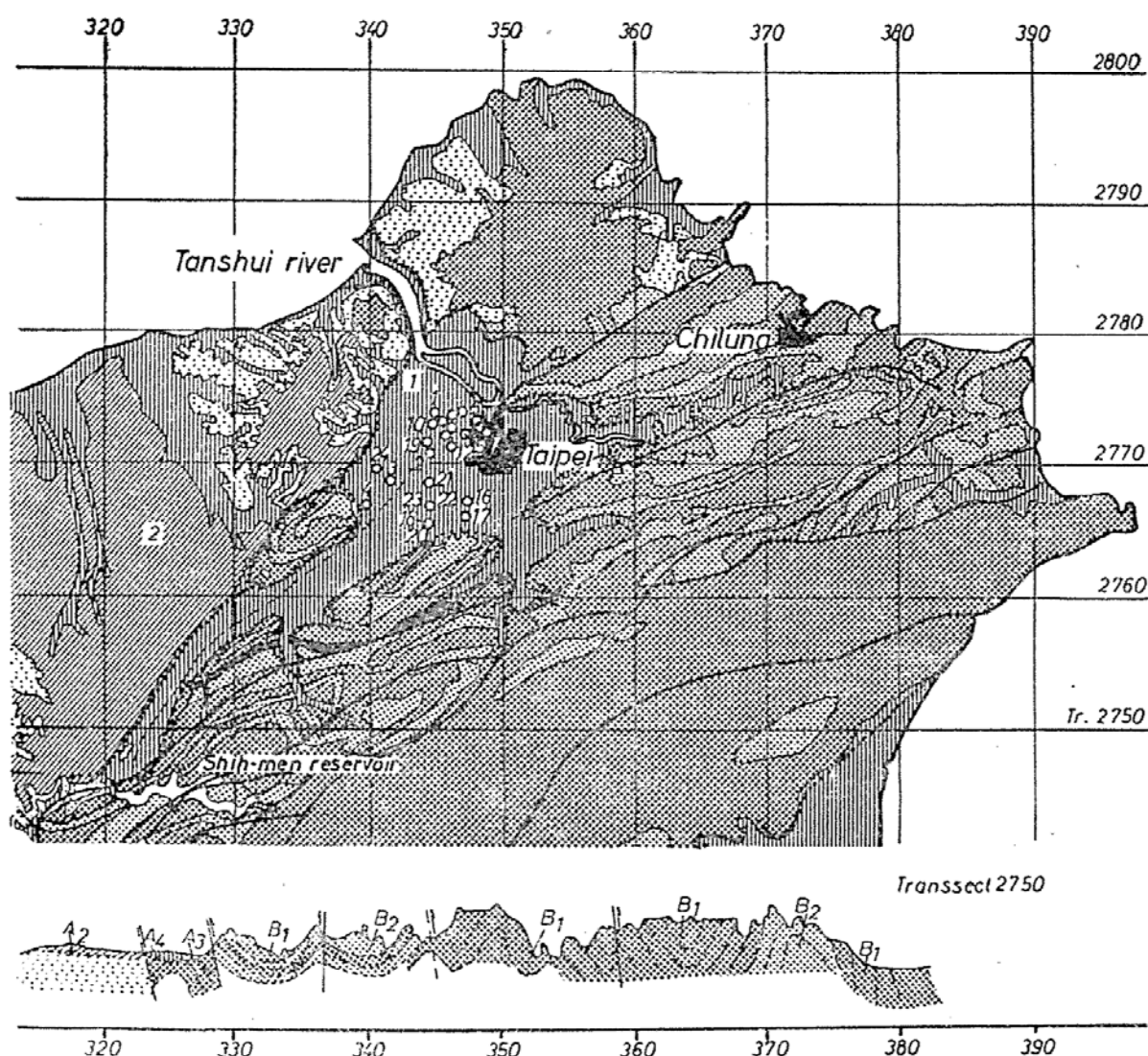
Fig. 6. Area around Taipei

of ground water consumption, are often obscured for a while and are measured only with a certain retardation.

An aging of the ground water by carbon from lethogenic carbonate species is in Taiwan less relevant than in more arid sampling regions. This is because of the lack of carbonate in most sediments of Taiwan with her high pluviometry. Therefore, the data were not corrected for carbonate—C contribution. Anyway, the present correction methods are still of questionable value[4-6].

1. The basin of Taipei

Figure 7 shows the sampling stations 1–24 in the basin of Taipei, which are seen in Figure 6 as closely concentrated spots. The arrows
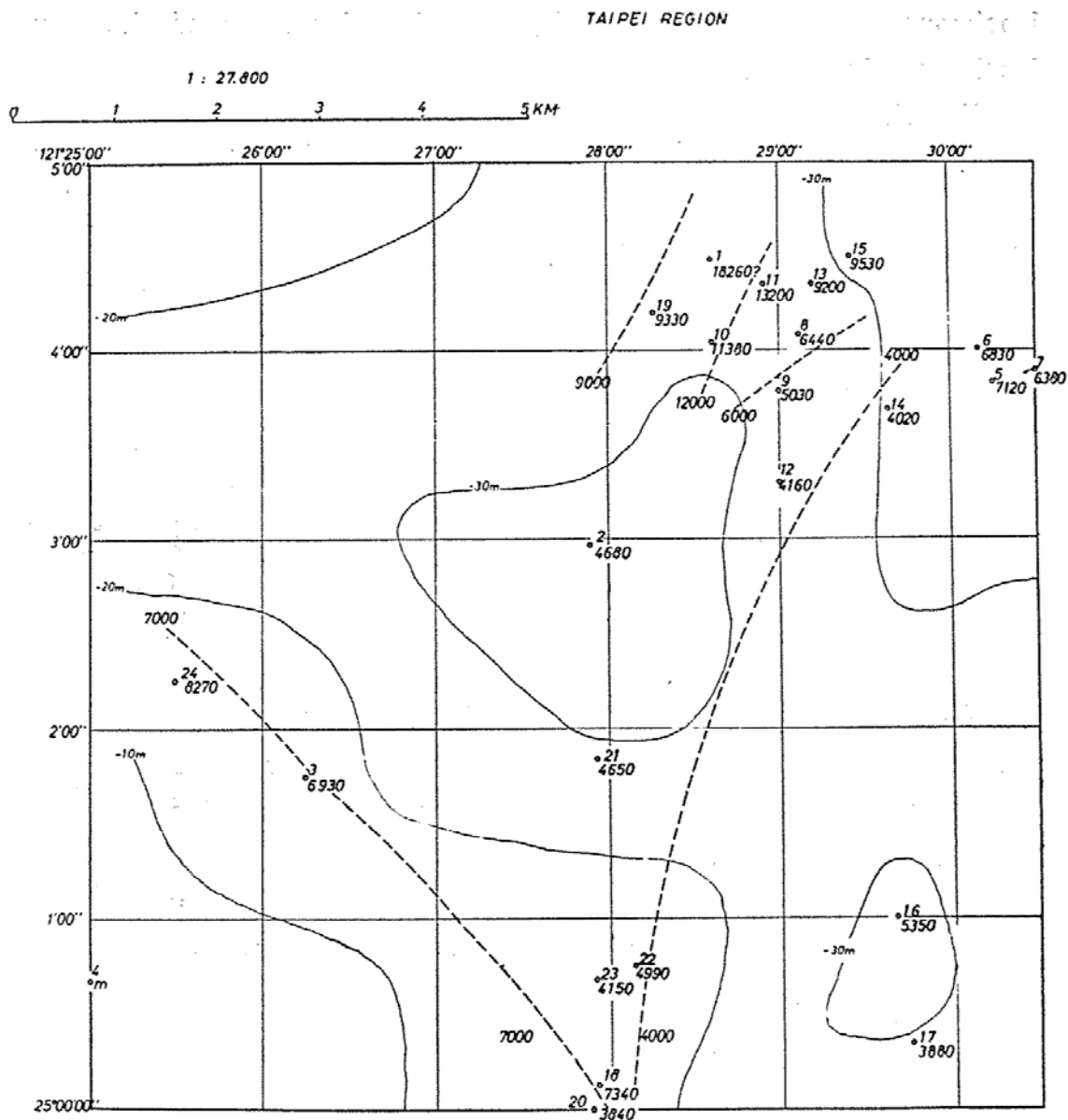
TAIPEI REGION

Fig. 7. The Taipei region

in Figure 6 point to the direction of ground water flow down from
the mountains and hills into the basin of Taipei. This flow direction
is confirmed by the centripetal increase of radio-carbon ages, which
means an increase of C^{14} age as the center of the basin is approached
from the remoter recharge areas of the ground water table. In this
basin of Taipei, we found the oldest ground water deposits of this
study having more than 13,000 years B. P.

Isochrones of 4,000; 6,000; 12,000; and 9,000 years (E—W) permit
calculating the flow velocity of the ground water, by dividing the

isochrone distances in meters by the time intervals of the same isochrones in years.

For the Taipei basin, the following flow velocities were found: between isochrones 9,000 and 12,000 about 0.28 m/year, between isochrones 6,000 and 12,000 about 0.15 m/year, and between isochrones 4,000 and 6,000 about 0.40 m/year. This indicates an almost immobile and static collection of ground water in the depression of the Taipei basin. A higher flow velocity may occur if sink cones are formed by increasing water consumption, such that a greater flow gradient is created, and in the scope of the "Darcy k-value relation" a quicker water transport is made possible.

The degree to which the presently observed subsidence is connected to the formation of such sink cones (which are due to increased ground water consumption), is best determined by measurements in piezometric tubes.

Atomic-bomb H^3 contents in the ground water samples (except sample 23, paper mill) hint also at a vertical water movement, since the flow velocity from the more elevated ground water recharge areas is much slower. It must be assumed, however, that a direct intrusion of young water from rainfall into the wells is excluded. This assumption may be true for the vast majority of wells in the basin of Taipei.

2. The coastal plane between the river Wu and Chiayi (the Choshui River Alluvial Fan)

This is the area (see Fig. 8) where the recent alluvial and colluvial sediments attain their biggest E-W extension. The flow direction of the ground water is clearly from the rain-rich heights of the central mountains sloping down towards NW and SW. Isochrone connections of the sample points 25 to 33 with age-steps 2,250 to 5,250 years a'low calculation of a flow velocity of about 5 m/year. The young age of the westernmost sampling point 31 is probably influenced by the closeness of the well to the river, where modern water of the river's ground water brink might have infiltrated the well. All these samples contain tritium. Also the samples of the relatively deep wells in the area of Touliu indicate an H^3 concentration of 20 to 40 T.U.
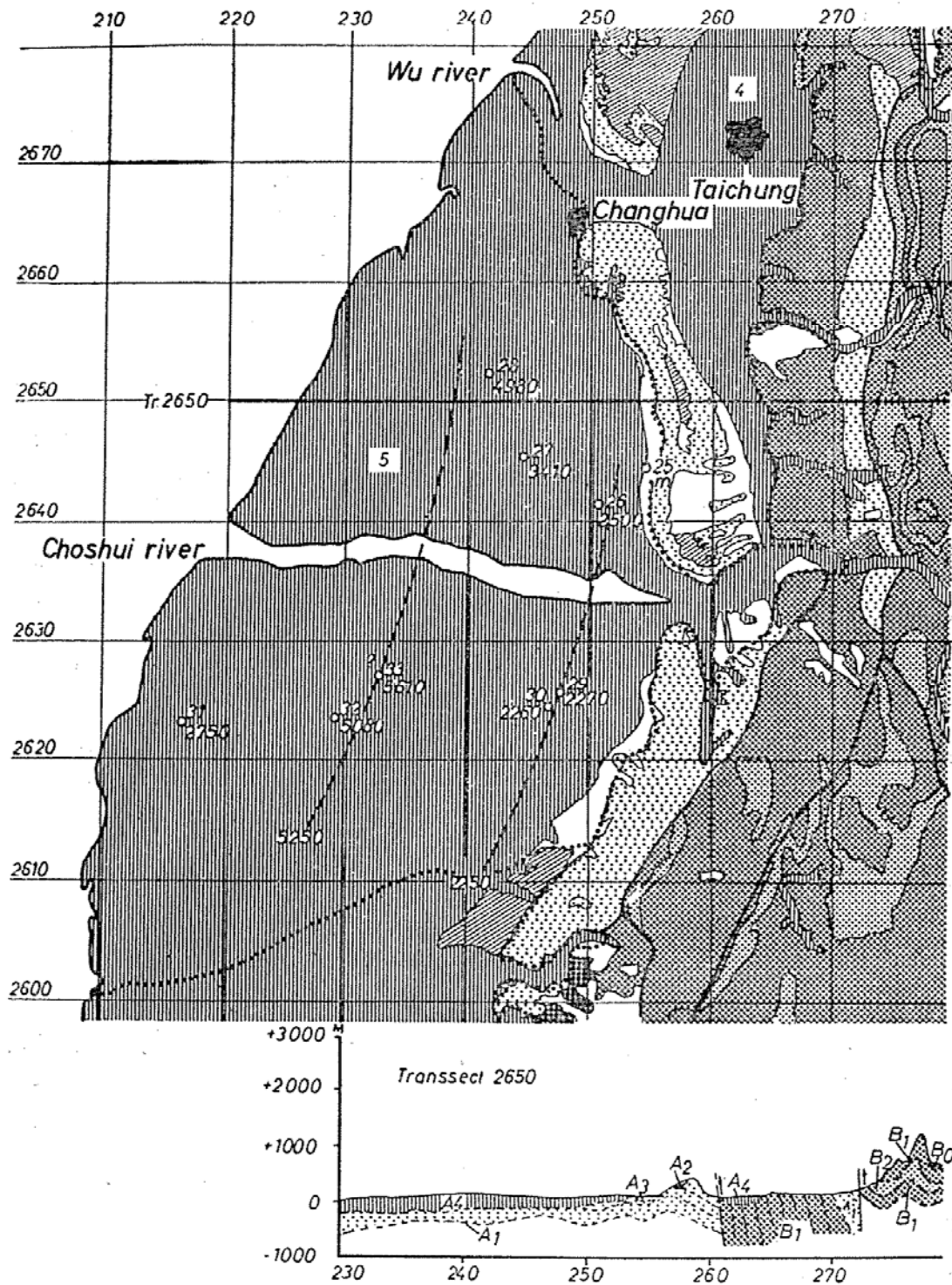
Fig. 8. Choshui River Alluvial Fan

Since with the low flow velocity of about 5 m/year this water containing tritium cannot have drifted to the present sampling position from the ground water recharge regions in the mountains, (thermo-nuclear tests, freeing H³, only started around 1956), it must be assumed that also a vertical importation to the present ground water exists. This means a rejuvenation and demands an originally higher age of the unblended depth ground water. In addition, such a vertical infiltration of modern, tritium-containing water into the ground water, can also originate from intrusion of water close to the surface into the well tube, especially if all available water is unselectively included (see Table 1).

In that case, the tritium measurements can not be interpreted with respect to ground water recharge, and the C^{14} data must be taken as minimum ages. Unfortunately in this area, just as in the Taipei basin, no data could be obtained about the depth of perforation of the filtering system of the well tubes. At single sampling stations, a faulty intrusion of surface water into the capture region of the well might be recognized by a decrease of the radiocarbon age, and therefore an inconsistency with the isochrone. The possibility of mixing between ground water and young water from the phreatic table must finally be decided by a control of correct performance as well as building plans of the wells.

3. The sugar cane region in the coastal plain between the river Tsengwen and the southeasterly river Kaoping

In this southern part of the coastal region, 51 sampling stations were selected, making it the most densely sampled area. In principle the flow direction of the ground water is from N. E. to N. W. In the southern part of the syncline between the river Kaoping and the eo-oligocene mountainous region of the southern tip of Taiwan, this flow direction is also confirmed by the direction of flow. From the distance of isochrones in meters, divided by the time difference in years, the flow velocity of the water is found to be about 2–3 m/year (Fig. 9).

However, in the northern part, which is south of Tainan and around the Akungtien reservoir, the measured isochrones of 1,000 to
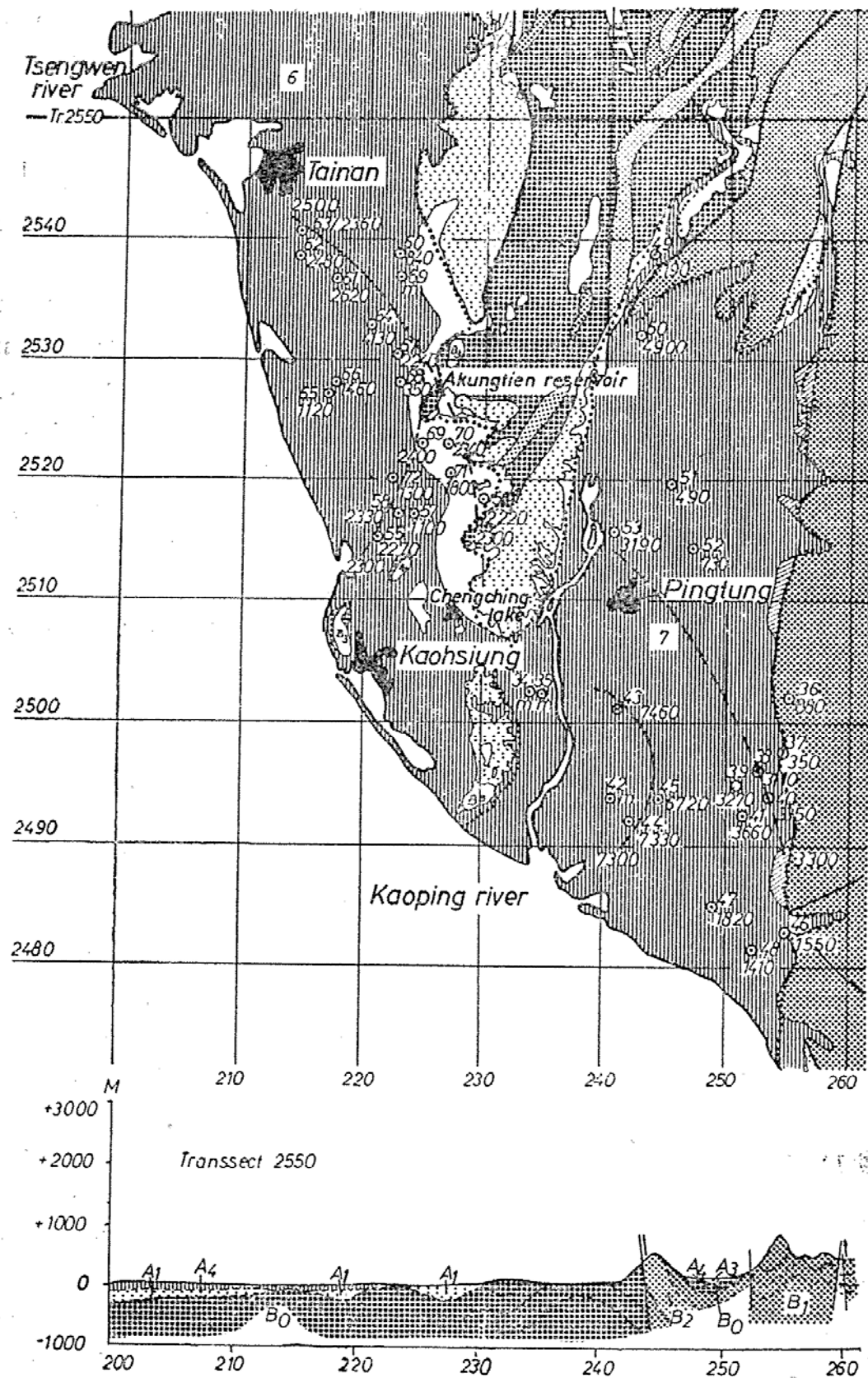
Fig. 9. Regions in Southern Taiwan growing sugar cane

3,000 years, are very closely spaced. This points to an accumulation of ground water in a shallow depression. Exceptionally low ages and low measurements of C^{14} concentrations (eg. 34, 35, 42) are due to samples from the vicinity of rivers and apparently are influenced by the rim of the river ground water.

Also in districts of the southern coastal plain, where sugar cane is grown, all the examined ground water samples contain tritium.

Most of the wells are only moderately deep with a perforation that makes use of the greatest part of the drilling depth. From data obtained by bomb-tritium measurements it might be necessary to conclude that a recharge with modern rain water took place, which is more probable for shallow wells. In general, however, the measurement data are valid only under the assumption that the wells have water-tight walls and even under heavy rainfall will not allow modern water to infiltrate the shaft of the well.

The higher age of samples 74–76 is influenced by enrichment of the water with fossil CO_2.

SUMMARY

In the basin of Taipei as well as in two regions along the western coastal plain of Taiwan, which are important for domestic economy and water consumption, a total number of 84 springs and wells were examined as to the natural C^{14} and H^3 content of their waters. A reported strong subsidence of ground water level in these areas of Taiwan was the main incentive for these experiments. The high pluviometry of Taiwan increases the danger of intrusion of young rain-water into the shaft or the perforation volume of the column of the well, which had to be accepted as a risk factor.

1) The basin of Taipei experiences a strong topographical subsidence of the surface and a decrease of the ground water level. Here the oldest waters of the region are found, converging from the Andesit heights of the North, the pleistocene sediments of the West, and the young tertiary sediments of the South and North. The flow velocity inside the basin is calculated by means of isochrone distances and is found to be very small (less than 1 m/year). From

the tritium contents of the samples a substantial horizontal and also vertical renewal of ground water is concluded, originating from the phreatic level. During the last years, a sharp increase of water consumption took place. This might presently lead to formations of sink-cones, of stronger slope declines, of increased flow velocities, and hence of a resulting new, lower-lying ground water level.

2) In the coastal area of the "Choshui River Alluvial Fan", the experimental data allow the construction of two isochrone ground water thresholds with C^{14} ages of 2,250 and 5,250 years. The north-westerly and north-easterly directed water drainage shows a flow velocity of about 5 m/year. Tritium concentrations hint at a complementary vertical infusion of recent waters down to ground water layers of more than 200 meters depth.

3) In the southern tip of the coastal plain of Chianan, Tainan, and Pingtung, two regions have to be distinguished. First the region of rather stagnant ground water of the depression in the area of the Akungtien Reservoir with C^{14} ages around 1,000–3,000 B. P., and secondly the Pingtung plain, where the south-westerly flowing waters have a velocity of about 3 m/year, and where from N. E. to S. W. the C^{14} isochrones of about 3,300 and 7,300 years can be distinguished. In this southern area, the depth of ground water is without exception lower than in the area of the Taipei basin and the "Choshui River Alluvial Fan". Tritium contents in water with its small flow velocity hint also to vertical infiltration into the ground water.

LITERATURE

(1) H. Walter und H. Lieth, *Weltklimakarten*, G. Fischer Verlag, Jena, 1967.

(2) B. Chingchang, *Lexique Stratigraphique International*, Volume III, Asie, Centre National de la Recherche Scientifique, 13. Quai Anatole France, Paris VII.

(3) H. W. Scharpenseel und F. Pietig, Einfache Boden-und Wasserdatierung durch Messung der ^{14}C- oder Tritiumkonzentration, *Geoderma*, 2, 273–289, 1969.

(4) H. Craig, Mass Spectrometer Analysis of Radiocarbon Standards, *Radiocarbon*, 3, 1–3, 1961.

(5) M. A. Tamers, Radiocarbon Ages of Ground Water in an Arid Zone Unconfined Aquifer, *A. Geophys. Union Mon.* 11, 143, 1967.

(6) H. W. Scharpenseel und J. Ohling (under technical assistance of F. Pietig,

E. Kruse, H. Gewehr, W. Kerpen, Chr. Haupenthal und H. Tapp), *Natürliche Radiokohlenstoff-und Tritiummessungen in Grundwasserproben von Tunesien und Algerien*, Fortschritte der Geologie Nordrhein-Westfalens (im Druck).

(7) C. W. Rose, *Agricultural Physics*, Pergamon Press, Sydney, 162, 1966.

COMPARATIVE STUDY OF OSTEOLOGY ON THE HOUSE GECKOS, *HEMIDACTYLUS BOWRINGII* (GRAY) AND *HEMIDACTYLUS FRENATUS* DUMERIL & BIBRON FROM TAIWAN

YUNG-SHENG LIANG & CHIN-SHIANG WANG

INTRODUCTION

Two kinds of house-geckos, *Hemidactylus bowringii* and *Hemidactylus frenatus*, are abundant and widely distributed in Taiwan. The taxonomic studies based on the external features were made by many herpetologists. However, the osteological features of these two species are still unexplored. The differences and the similarities of skeletal structure between these two species are not only for anatomical interest but also for providing help to taxonomic study because the osteological characteristics are always more constant. In the present paper, we intend to deal with the osteological studies of *H. bowringii* and *H. frenatus*. Every part of their skeletons and each piece of bone are observed in detail. A comparison of the characteristics of each, whether similarities or differences, will be made. By means of this comparison, these two species can be distinguished much more clearly.

The lizards, *H. bowringii* and *H. frenatus* were collected from Taipei and Puri, Taichung. Five specimens of the former and thirty specimens of the latter were used in this study. They were treated by cleaning and staining methods. The skeletons were examined under a binocular microscope. The drawings were made by using camera lucida.

DESCRIPTION OF THE SKELETON OF *H. BOWRINGII* (GRAY)

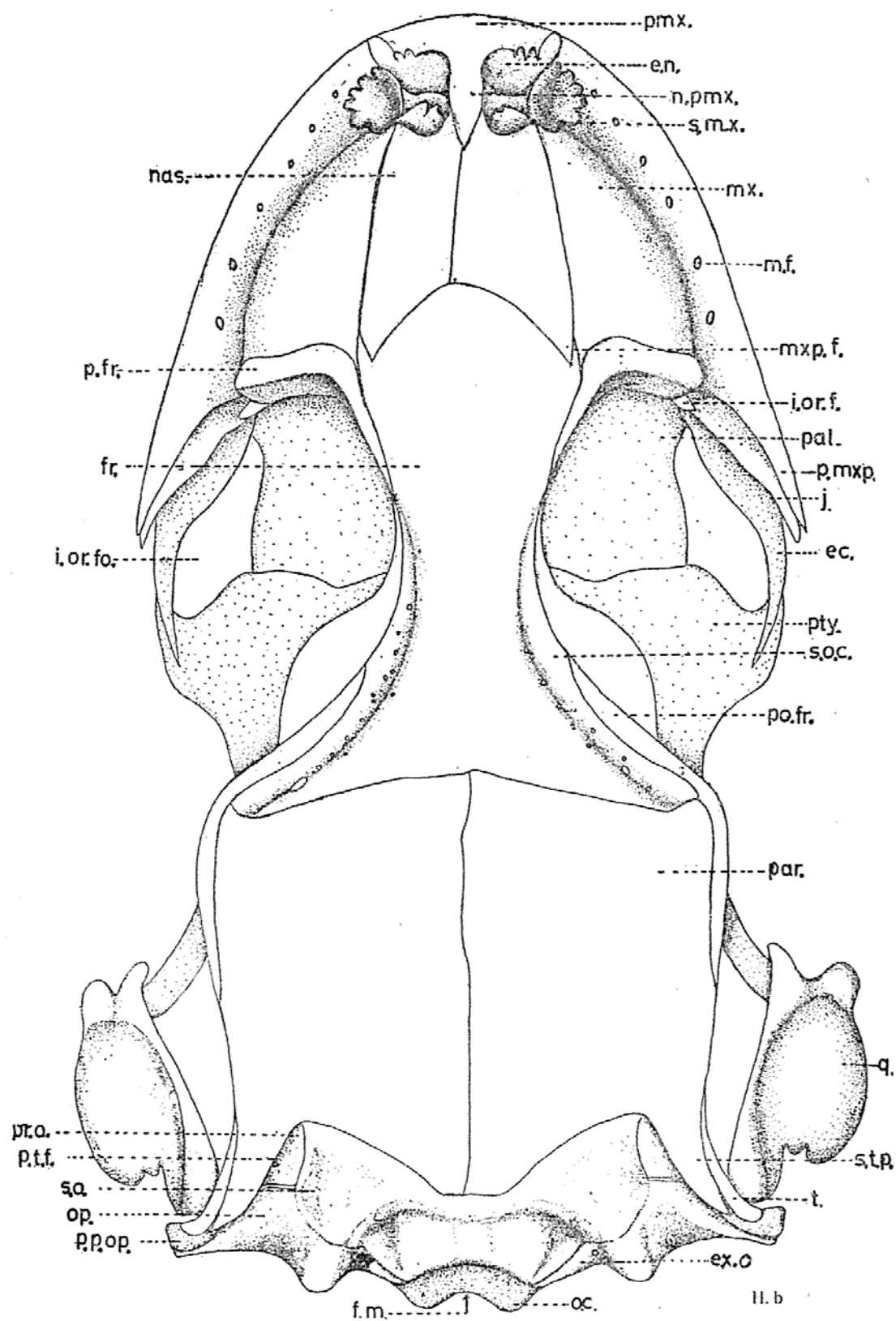## 1. Skull

A. *General Characteristics*

The skull of *H. bowringii* is depressed and flattened in general. The ventral surface and the caudal surface of the skull are flattened but the two dorso-lateral sides of the preorbital region are curved convexly and pass insensibly into each other in the middorsal line. The convexity of the dorsal surface is slight. The snout of the skull is rounded. All bones of the skull are loosely articulate with each other.

B. *The Cranium*

(1) Occipital region

The occipital region is completely ossified and surrounds the big, rounded aperture, foramen magnum. It consists of four bones, (a) the basioccipital, (b) the paired exoccipitals and (c) the supraoccipital. Except the exoccipitals which are cossified with the opisthotic, the remaining bones remain distinct throughout life. The single occipital condyle is crescentic in outline; the median basioccipital piece of the condyle (*pars condyloidea*) is as large as the lateral pieces which are formed by the posterior end of the exoccipitals. The supraoccipital houses the roof and internal postero-superior side of the auditory capsule.

Basioccipital: The median basioccipital forms the posterior portion of the ossious cranial floor, which is more or less triangular in shape, broad in front but narrow behind. Its anterior border forming the base of a triangle is slightly curved backward and articulates with the basisphenoid. The antero-lateral border forming the side of the triangle is curved outwards. It articulates with the prootic in front and the opisthotic behind, and the outer side of it projects ventro-laterally and forms the antero-inner borders of a rather deep concave cavity called the *recessus scalae tympani*. It houses three foramina. The *apertura medialis recessus scalae tympani*,

Fig. 1. Dorsal view of the skull of *H. bowringii*.
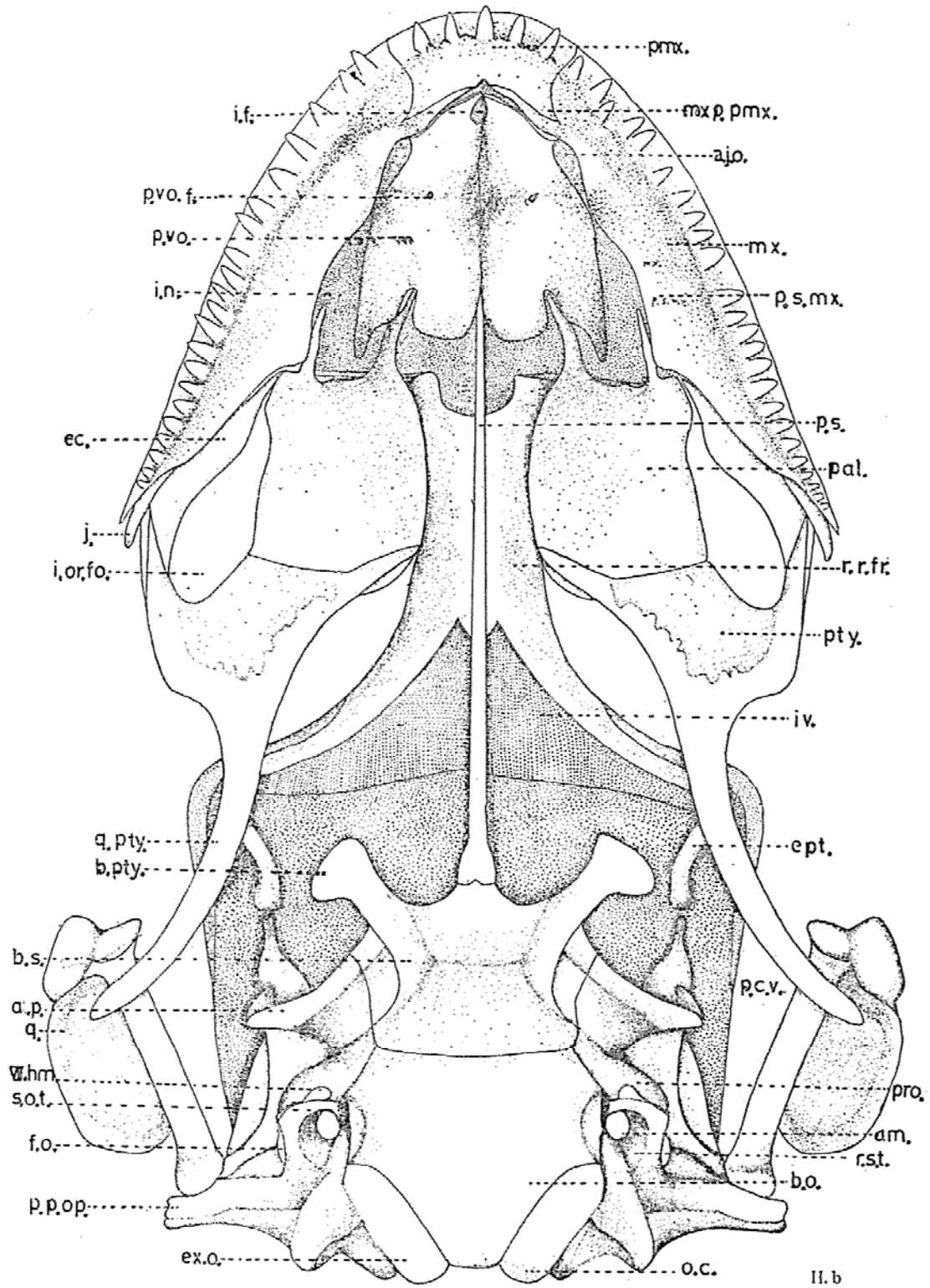
Fig. 2. Ventral view of the skull of *H. bowringii.*

one of these three foramina, is surrounded by the basioccipital ventrally, by the opisthotic dorsally and by the exoccipital caudally. On the outer side of the lateral border of basioccipital is a kidney-shaped tubercle which is called the *spheno-occipital tubercle* or *tuberculum spheno-occipital*. The postero-lateral border forming the side of the triangle is slightly curved inward and fuses with the exoccipital.

The narrowed posterior end of the basioccipital forms the median piece of the *occipital condyle (pars condyloidea)* and also a very small part of the ventral median boundary of the *foramen magnum*, which is slightly raised.

The dorsal surface of the basioccipital is concave for the accommodation of the *medula oblongata*. The lateral eminenses project dorsally to form the dorsal portion of the antero-inner wall of the *recessus scalae tympani*.
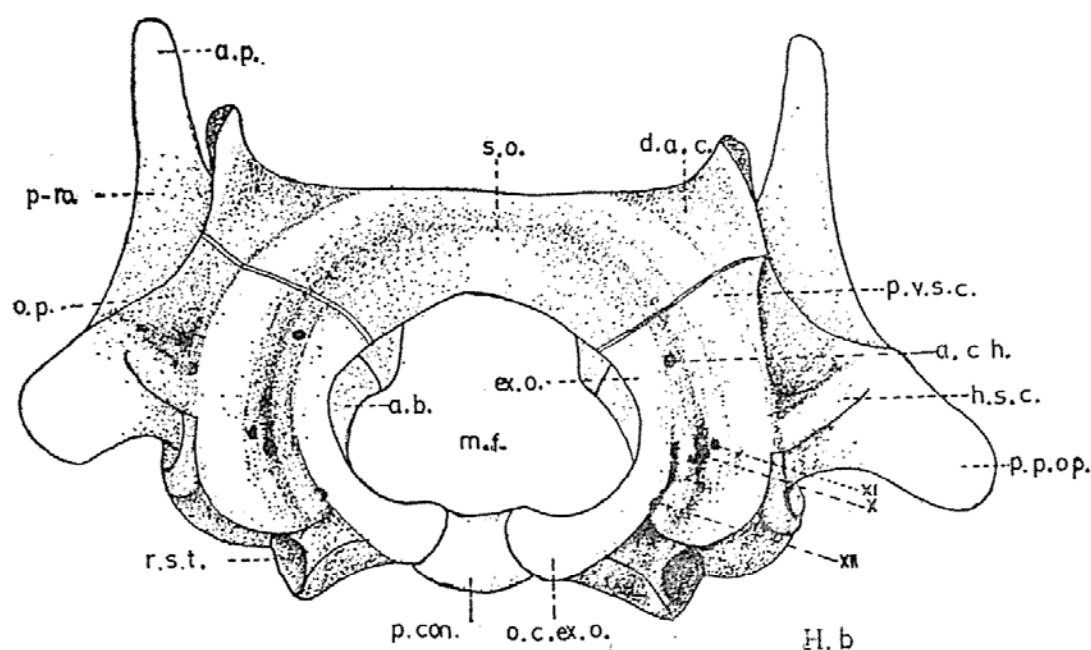

Fig. 3. Posterior view of the skull of *H. bowringii*, parietals removed.

Exoccipital: The paired exoccipitals of the adult are inverse T in shape and recurved bones. When it is viewed from lateral side, it fuses with the opisthotic bone and can hardly be distinguished from each other in the adult (Fig. 8). The ventral rami of the exoccipitals form a part of the caudal and ventral wall of the cranium

and the lateral pieces of the occipital condyle on each side, while the dorsal rami form the lateral sides of the foramen magnum (Fig. 3).

The exoccipital lies ventro-dorsally on each side of the basi-occipital. It articulates along its ventromedial border with the basi-occipital, fuses completely with the opisthotic laterally and articulates with the supraoccipital dorsally.

The ventral ramus of the exoccipital is pierced by three small foramina in linear series (Fig. 7). These foramina permit the branch of the *hypoglosal nerve* (XII) to leave the skull (Fig. 8).

The boundary between the exoccipital and opisthotic bone is clearly indicated by a distinct furrow on the inner surface of the cranium. This furrow is pierced by five foramina. The exoccipitals also form the posterior border of the apertura medialis recessus scalae tympani. As viewed from the ventral side, the exoccipital forms the small portion of the posteromedial wall of the recessus scalae tympani.

Supraoccipital: The median butterfly-shaped supraoccipital bone forms the dorsal roof of the occipital complex, the roof and the inner superior portion of the auditory bulla on each side (Fig. 8), and the dorsal border of the foramen magnum. Dorsally, it lies at a lower level behind the parietal. The anterior border is crescentic in outline and provided with a smooth area which is overlapped by the parietal, the two bones being movable with respect to each other on a limited range. The posterior border is notched. The supraoccipital articulates with the prootic antero-laterally and with the opisthotic and exoccipitals posterolaterally. The portion forming the roof of the auditory capsule is triangular in shape, the remaining region of the bone is fan-shaped and lies at a lower level behind the dorsal roof of the auditory capsule. The fan-shaped area is more raised medially and slopes in an antero-posterior direction as well as laterally on each side.

On the inner surface, the supraoccipital gives rise ventrally to a large triangular eminence which articulates with prootic anteriorly and with the opisthotic and exoccipitals posteriorly (Fig. 8). This eminence houses the superior portion of the auditory bulla. Between

the union of the prootic, opisthotic and supraoccipital, there is a small *endolymphatic foramen*. The supraoccipital, housing the auditory capsule, is perforated by a part of the *anterior* and *posterior vertical semicircular canals* which surround the semicircular ducts.

(2) Parietal region

The parietal region lies in front of the occipital complex and consists of a pair of the parietals above and a single basisphenoid below. The side wall of this region is formed by the prootic behind and by a thick membranous wall in front.

Basisphenoid: The basisphenoid articulates loosely with the basioccipital by the posterior border whose corner is overlapped by the basioccipital on the dorsal aspect. There are two lateral borders on each side, i. e. a dorsal lateral border and a ventral lateral border which are separated by a longitudinal furrow, *sulcus venae jugularis*. Between the two, the dorsal lateral border articulates along its entire length with the prootic, while the ventral lateral border is free (Fig. 2). The basisphenoid articulates with the pterygoid, through the pterygoid meniscus, by the ligament (Fig. 15A). This articulation is movable like that between supraoccipital and parietal and forming another essential factor in the kinetism of the skull.

On the dorsal surface, the single *crista sellaris* forms a transverse high ridge separating the anterior deep depression called the *hypophysial fossa* (*sella turcica*) from the posterior basicranial depression (Fig. 4). The hypophysial fossa lodges the *recessus infundibularis* and the *hypophysis* of the diencephalon. The anterior border of the hypophysial fossa gives off a short and stumpy medial bified process, *parasphenoid process*, with which the parasphenoid articulates in front. On each side of this process, the bone is produced antero-laterally into a thick stout process, the *basitrabecular process* (*basipterygoid process*), which is expanded at the distal portion. A thin sheet of bone continues laterally from the floor of the hypophysial fossa over the dorsal surface of the base of the basitrabecular process to form the lateral wing of the basisphenoid (or dorsal lateral border of the basisphenoid).
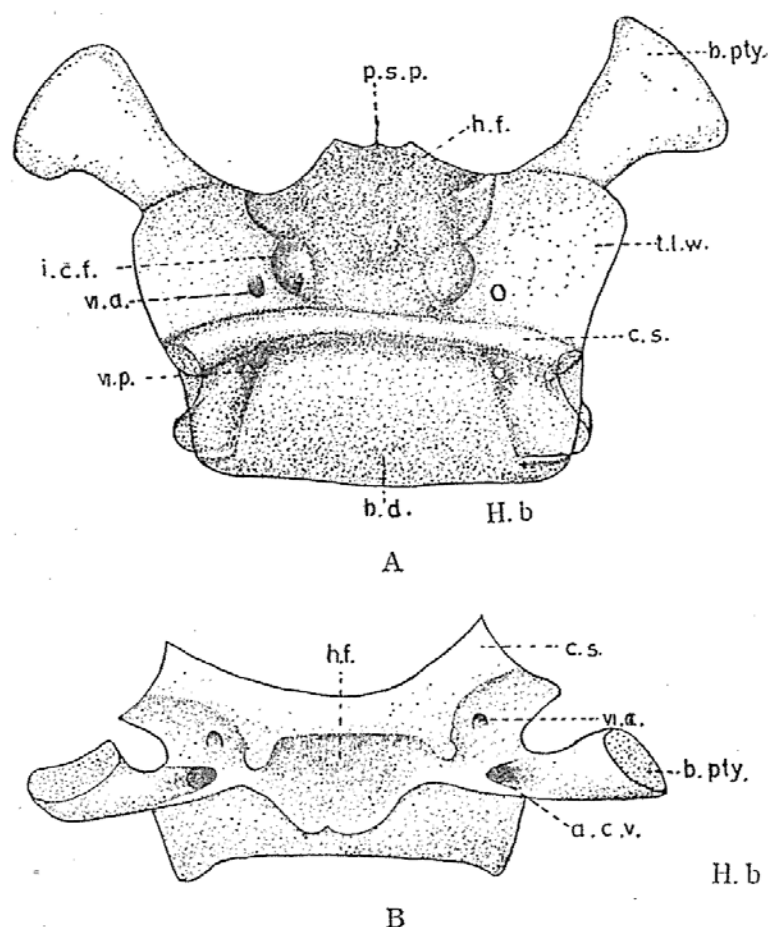
Fig. 4. Basisphenoid of *H. bowringii*. A. dorsal view; B. anterior view.

On the dorsal surface, there is a foramen, *posterior foramen for the abducens nerve*, on each anterior corner of the basicranial depression for the exit of the *abducens nerve* (VI). This nerve perforates the crista sellaris at right angle, then runs through a very short canal and comes out through the lateral wing at the base of the basitrabecular process on the dorsal side, wherefrom it runs outwards to inervate the external rectus muscle of the eye. The large posterior *vidian canal* (*canalis vidianus*) penetrates through the posterior side of the sulcus venae jugularis and bifurcates anteriorly into two canals: (1) the *posterior internal carotid foramen* (*foramen caroticum internum*) opening into the posterior lateral side of the hypophysial fossa and (2) the anterior opening of the vidian canal lying at the base of the basitrabecular process on each side, which is visible from the anterior side. Through the vidian canal, the *palatine branch of*

the internal carotid artery and the *palatine branch of the facial nerve* pass out. Through the internal carotid foramen, the cranial branch of the internal carotid artery enters the hypophysial fossa from the vidian canal and becomes completely intro-cranial.

Parietals: The parietals are a pair of more or less quadrangular bones. They articulate with each other in a middle line, with the frontal through a more or less outwardly curved suture in front, and overlap the supraoccipital with their obliquous posterior border. The antero-lateral border of each parietal articulates with the posterior ramus of the postfrontal.
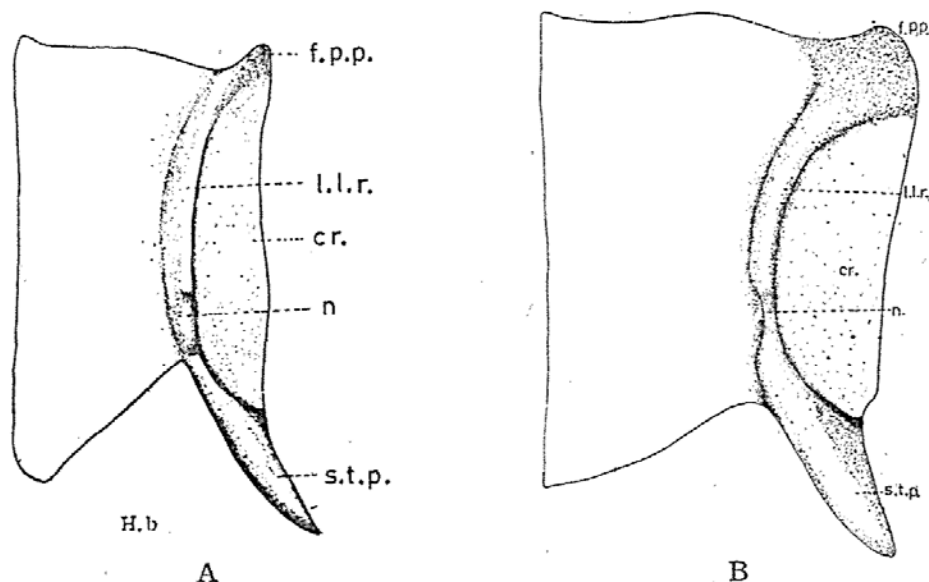

Fig. 5. Ventral view of the left parietal. A. *H. bowringii* and B. *H. frenatus.*

The *pariental foramen* is covered by a piece of bone in original position. Each parietal is produced behind into a *supratemporal process* which runs outward and backward to articulate with the tubular and the proximal region of the distal end of the paroccipital process of opisthotic, and thereby bounds the *post-temporal fossa* dorsally and laterally. The lateral border together with the proximal portion of the supratemporal process are produced into a crest. A short *frontal process* extends forward from the anterolateral corner of the parietal and articulates with the frontal and postfrontal.

Ventrally, there is a slender longitudinal lateral ridge near the outer border in continuation with the supratemporal process. Just

anterior to the base of the supratemporal process the lateral ridge is shallowly notched. Through this notch and the depression between the anterior and posterior process of prootic bone, the temporal region of the skull is fenestrated. The anterior process of prootic articulates movably with the outer surface of the lateral ridge of the parietal just in front of the notch. The dorsal head of the epipterygoid articulates with the lateral ridge of the parietal just in front of the anterior process of prootic.

(3) Frontal Region

Anterior to the parietal region is the frontal region. It consists of a single frontal above and parasphenoid below.

Beside these bones there are membranous tracts which complete the wall of the cranial cavity. The brain cavity is confined to the dorsal part of the skull and lodges only the anterior part of the cerebral hemisphere and the olfactory stalk.

Frontal: The frontal is a single median element forming the dorsal border of the orbit and the anteriormost ring of the brain case; it lies in front of the parietals. It is an elongated bone, wide in front, broadest behind and narrow in the middle. The anterior border is slightly curved outward and is produced anterolaterally into a short *maxillary process.* The antero-lateral side of the bone is overlayed by the frontal process of the maxilla and fits into the groove of the lateral frontal process of prefrontal. Its outer borders behind the lateral frontal process of prefrontal are raised, on the dorsal surface, into the thin *supraorbital crest,* the posterior portion of which articulates with the anterior ramus of the postfrontal, while the inwardly curved posterior border of the frontal bone loosely articulates with the parietals (Fig. 1).

On the ventral surface, the borders are inflected downward and inward to form a pair of *ventro-lateral processes,* which fuse with each other to form a round ridge and enclose a canal, *olfactory canal (canalis olfactorius),* in order to lodge the olfactory stalks. The fusion of the processes is incomplete anteriorly in young specimen. Each side of the anterior border of the round ridge is produced into
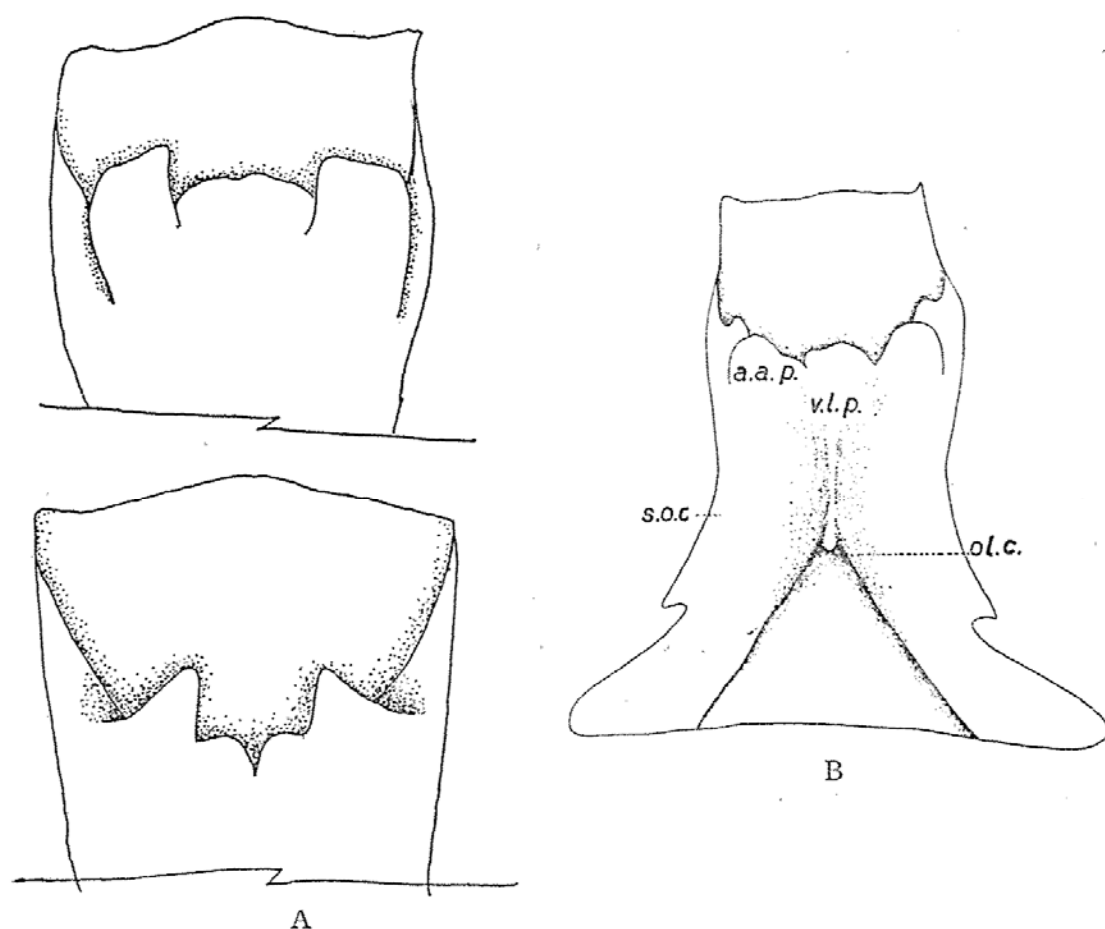
Fig. 6.   Ventral view of the frontal.   A. part of the frontal of *H. bowringii*: above, adult; below, young.   B. *H. frenatus*.

an *antero-lateral alar process* which articulates with the medial frontal process of prefrontal anteriorly and prevomerine process of palatine, ventrally.   The mid-posterior end of the round ridge is produced posteriorly into a short pointed process (Fig. 2 & 6).

Parasphenoid: The parasphenoid is a long, narrow, conical cartilage, partially calcified in its posterior part, but the posterior end is bifid and flattened dorso-ventrally.   It underlies the ventral border of the interorbital septum in the mid-ventral line, articulating behind with the median parasphenoid process of the basisphenoid and terminating in front between the septomaxilla.   The major portion of its length forms the support of the interorbital septum (Fig. 1).

C.   *The Sensory Capsules*

The olfactory or nasal capsule and auditory capsule are closely

connected with the skull, but the optic capsule is free and is protected by several bones of the skull.

(1) The Auditory Capsules

The auditory capsules are situated on each side of the occipital and parietal regions. They are formed on each side by the prootic, opisthotic of exoccipital and supraoccipital. A well developed *auditory bulla* formed by each of the above bones is bulbed inward into the cranial cavity and can easily be seen from the foramen magnum (Fig. 7 & 8).

Opisthotic: The opisthotic is indistinguishably fused with the exoccipital and houses the posterior portion of the membranous labyrinth of the inner ear. A stout horizontal process, the *paroccipital process*, is directed outward and slightly backward. This process supports the supratemporal process of parietal and squamosal, above and quadrate, below.

As viewed from the outer side, the opisthotic articulates anteriorly, with the prootic, ventrally, with the basioccipital and

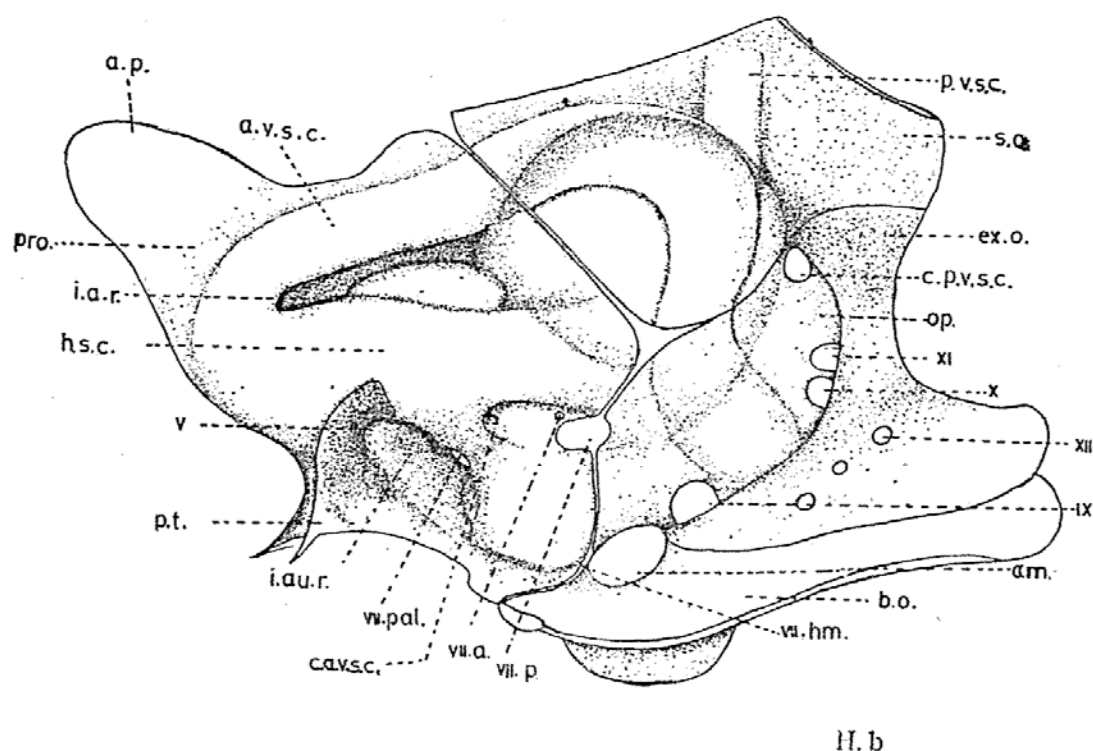Fig. 7. Auditory capsules viewed from outer side.

Fig. 8. Auditory capsule viewed from inner side.

dorsally, with the supraoccipital, while it fuses caudally, with the exoccipital.

On the internal side, the superior half of the anterior border of the opisthotic articulates with the supraoccipital, and the inferior half of it articulates with the prootic, while the posterior border fuses with the exoccipital.

On the ventral side, the opisthotic forms the ventral boundary of the auditory capsule. The *recessus scalae tympani* is widely open ventrally. The margin of the recessus scalae tympani is enclosed medially by the basioccipital and the remaining part is enclosed by the opisthotic and exoccipital. Within the recessus scalae tympani there are three large foramina: (1) the *perilymphatic foramen (foramen perilymphaticum)* which is the superior one of these three foramina, surrounded by the opisthotic and leading into the *lagenar recess*; (2) the antero-ventral *apertura medialis recessus scalae tympani* which is surrounded by the opisthotic, basioccipital and exoccipital; (3) the postero-ventral *glossopharyngeal foramina* which is surrounded on its ventral half by the basioccipital and dorsally by the opisthotic.

On the outer side, the prominent *paroccipital process* extends perpendicular to the auditory capsule. This process projects much beyond the side of the occipital complex; the height is greater than the width. Just anterior to and below the base of the paroccipital process there lies a large ovally shaped *foramen oval (fenestra ovalis)* which is enclosed on its anterior half by the prootic and on its posterior half by the opisthotic.

On the inner side, the opisthotic bone houses the posterior lower portion of the swollen auditory bulla. Opisthotic and exoccipital are co-ossified into a single bone. There is no suture between them, but there is a prominent furrow between opisthotic and exoccipital on the inner side of the cranium. This furrow forms the boundary between the opisthotic and exoccipital and is perforated by four foramina. On the ventral termination of the furrow there is a large foramen which is enclosed dorsally by the opisthotic and ventrally by the exoccipital; it opens into the recessus scalae tympani. This large foramen is the *glossopharyngeal foramen* and permits the *glossopharyngeal nerve* to pass out of the skull. Approximately on the middle portion of the furrow there are two foramina, of which the lower one, *vagus nerve foramen*, transmits the *vagus nerve* (X) and the dorsal one, *spinal accessory nerve foramen*, transmits the *spinal accessory nerve* (XI). Both of these two nerves come out of the skull through a single linearly shaped *jugular foramen* which is enclosed laterally by the opisthotic and medially by the exoccipital. On the dorsal termination of the furrow, there is an opening leading into the posterior vertical semicircular canal of the internal ear. Opposite to this opening, on the outer side of the skull, there is a small foramen leading into the posterior vertical semicircular canal (Fig. 3 a. ch.). Immediately anterior to the glossopharyngeal foramen, there is a large foramen, *apertura recessus scalae tympani*, which is enclosed by the opisthotic, basioccipital, and exoccipital.

The opisthotic is perforated by the posterior half of the horizontal semicircular canal and the lower major part of the posterior vertical semicircular canal.

Prootics: The prootic is a 凸 shaped bone, antero-dorsally pro-
jecting stout, flat processes, and forming the anterior section of the
auditory capsule.

There are three processes on the prootics. The *anterior process*
is stout and flat and projects antero-dorsally. It is perforated on its
root by the anterior vertical semicircular canal of the internal ear
and articulates movably against the outer surface of the lateral ridge
of the parietal ridge of the parietal. The bulged anterior vertical
semicircular canal houses the *external ampular recess* on the outer
side and the *internal auditory recess* on the inner side of auditory
capsule. The *posterior process* is flat and projects postero-dorsally.
It articulates with the supraoccipital and opisthotic on the upper side
of the skull. This process is perforated by the anterior vertical
semicircular canal, and on its root by the horizontal semicircular
canal of the inner ear. On the ventral side, the third process, *alar
process*, which projects antero-ventrally beneath the base of the
anterior and posterior process, is a flat wing-like process and articu-
lates with the basisphenoid by its medial border. The ventral border
of the prootic articulates, from the anterior to posterior, with the
basisphenoid and basioccipital bones. On the ventro-lateral side,
below the anterior vertical semicircular canal, there is a deep outer
auditory recess which is bordered anteriorly by the alar process. On
the postero-dorsal corner of the bottom of the recess and just below
the ampula of the anterior vertical semicircular canal, there is a
small foramen, *anterior facial foramen*, which provides for the exit
of the *palatine branch of the facial nerve*. Near the base of the
paroccipital process of the opisthotic, there is an ovally shaped foramen,
foramen oval (fenestra ovalis), for the insertion of the inner end of
the *columella auris*, which is margined anteriorly by the prootic and
posteriorly by the opisthotic. While the slit-like foramen, *posterior
facial foramen*, lies immediately anterior to the anterior border of
the recessus scale tympani, it is surrounded by the prootic, opisthotic,
and basioccipital bones and lets through the *hyomandibular branch of
the facial nerve.*

On the internal side of the cranium, the posterior border of the prootic articulates with the supraoccipital and opisthotic, and the ventral border articulates with the basioccipital and basisphenoid. The bulged anterior vertical semicircular canal and auditory bulla houses the *internal ampula recess*. Immediately below the anterior vertical semicircular canal there is a deep concave cavity, called *internal auditory recess*, which is perforated by two foramina. The postero-dorsal corner of the bottom of internal auditory recess is pierced by the *anterior facial foramen* through which the *palatine branch of the* VIIth *nerve* leaves the skull. Enclosing the anterior portion of the internal auditory recess is the perpendicular *pars trigeminalis*, which is pierced by the large, round *trigeminal nerve foramen* (V). Two *auditory foramina* pierce the under surface of the overhanging roof formed by the bulge of anterior vertical semicircular canal at the posterior margin of prootic. The posterior auditory foramen is much larger than the anterior auditory foramen, which is bordered posteriorly by the opisthotic and anteriorly by the prootic and lets through the posterior division of the auditory nerve. A very small anterior auditory foramen lies immediately on the antero-dorsal side of the posterior auditory foramen, which lets through the anterior division of the auditory nerve. Just anterior to the auditory foramina there is a channel tunneled into the anterior vertical semi-circular canal. A slit like *posterior facial foramen* lies immediately anterior to the apertura medialis scalae tympani, which is surrounded by the prootic, opisthotic and basioccipital and permits the *hyomandibular branch of the* VIIth *nerve* to leave the skull.

(2) The Bones in Relation with the Optic Capsule

The optic capsule is not connected to the skull. The depression in which it is situated is called the *orbit*. The orbit is surrounded partly by bones and partly by membrane. It is roofed over by the prefrontal, frontal, and postfrontal. The anterior side of the orbit is bounded by the prefrontal. The floor is formed partly by the jugal, ectopterygoid, palatine and pterygoide and partly by the thickened palatal membrane. The posterior side of the orbit is

bounded by the membranous ventro-lateral wall of the cranial cavity enclosing the forebrain. The orbit is separated from its fellow by the cartilagenous membrane which is suported by the cartilagenous parasphenoid that extends anteriorly into the nasal septum. The lacrimal is absent in this species (Fig. 1).

Prefrontals: The prefrontal is a large cup-shaped bone, forming the anterior angle of the orbit (Fig. 9). It is composed of two portions. *Pars maxillaris* forms a part of the hind wall and lateral wall of the olfactory chamber, and the anterior wall of the orbits. Pars frontalis consists of two processes: (1) *lateral frontal process* and (2) *medial frontal process.* The cup-shaped lateral frontal process is a continuation of the pars maxillaris; it runs dorsoposteriorly and articulates with the lateral edge of the frontal by its grooved inner surface. A short, pointed and flattened medial frontal process of pars frontalis arises from the grooved inner side of the dorsal margin of the pars maxillaris and turns medially, creating a gently rounded corner at its base which is overlapped by the frontal. It articulates with the
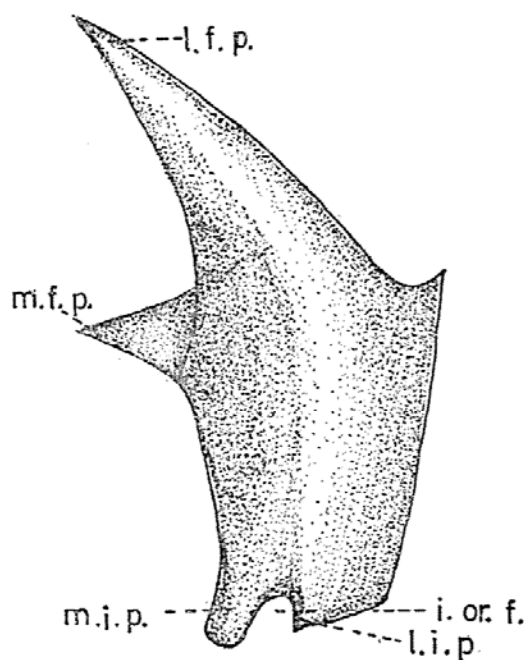
H. b

Fig. 9. Postero-lateral view of the prefrontal of *H. bowringii.*

antero-lateral alar process of the frontal, and it also articulates with the base of the prevomerine process and maxillary process of the palatine. The portion of the prefrontal forming the lateral wall of the olfactory chamber is thin and is overlapped by the maxilla. The *infraorbital foramen* is formed by the moderate notch in the ventral margin of the anterior wall of the orbit. The foramen is bounded by the downwardly projecting *infraorbital processes*, of which the lateral infraorbital process is much smaller than the medial one and articulates with the palatal shelf of the maxilla, while the medial infraorbital process articulates with the jugal, ectopterygoid, and paratal shelf of the maxilla. The roof of the infraorbital foramen is the rounded corner which is perforated by a foramen.

Postfrontal: The postfrontal is a crescentic shaped bone articulating along its grooved margin with the frontal and parietal. Both the anterior and posterior ends of the bone are pointed (Fig. 1).
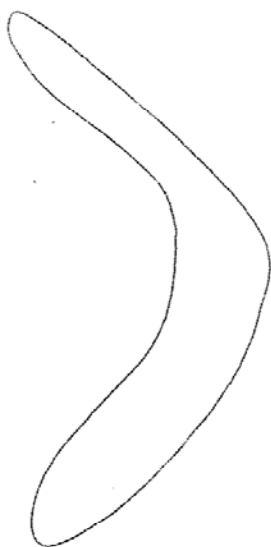
Fig. 10. Dorsal view of the right postfrontal of *H. frenatus*.

Jugal: The paired jugals are slender, flat, and slightly curved bones forming the outer ventral boundary of the orbits, which lie on the palatal shelf of the maxilla between the posterior maxillary process of maxilla and ectopterygoid. Anteriorly, each of these is broad and pointed at the tip but posteriorly, it becomes slender and pointed. The anterior end of the jugal projects slightly beyond the

infraorbital foramen, while its posterior end is beyond the extreme of the posterior maxillary process of the maxilla. The jugal articulates with the maxilla, prefrontal, and ectopterygoid (Fig. 1).

(3)   Bones in Relation with the Olfactory Capsules

The olfactory capsules occupy the greater portion of the facial portion of the skull. They lie in front of the cranial cavity and are separated from each other by the nasal septum. Each is bounded behind by the prefrontal, and laterally by the prefrontal and maxilla. Its roof is covered by the nasal and its floor is formed by the palatal shelf of the maxilla laterally, of the prevomer frontally, and of the maxillary process and prevomerine process of palatine and cartilagenous membrane, dorsally. Each olfactory capsule has the shape of a modified horse shoe and consists of two parts: (1) the *vestibule*, is a short outer limb of the horse shoe, which begins behind with the *external narial aperture* and leads forward right up to the junction of the pre-maxilla and maxilla; and (2) the *olfactory chamber* is the inner limb of the horse shoe, which is parallel and internal to the vestibule, and leads backward to open into the buccal cavity through
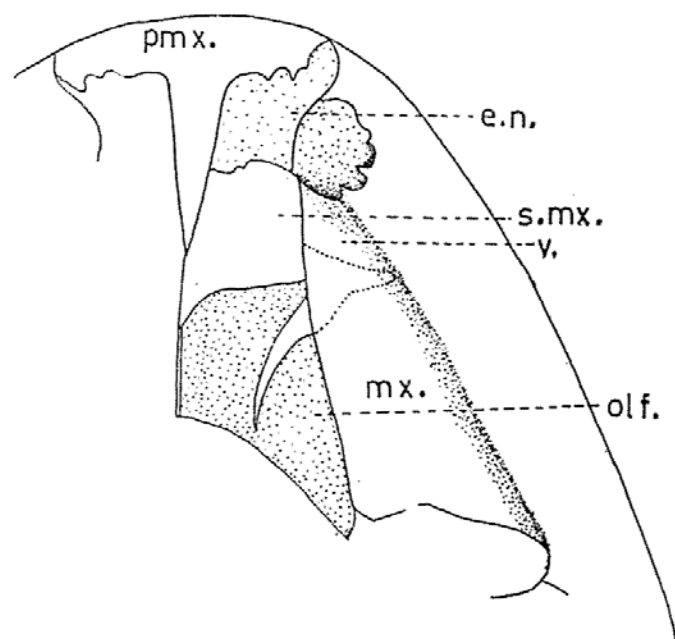

Fig. 11. Right side of the anterior portion of the head of *H. frenatus*.
The nasal is removed to reveal the olfactory chamber.

the internal nares or choana.   The vestibule and olfactory chamber are communicated with each other at the extreme anterior end just behind the premaxilla but are separated from each other by the lateral border of the body and the base of the lateral posterior process of septomaxilla (Fig. 11).

Nasals: The paired nasals are the thin bones lying in front of the frontal, forming the roof of the nasal capsule and the posterior boundary of the external nares.   Anteriorly and posteriorly along the midline, the nasals overlap with its counter part from the opposite side or articulate with each other.   They overlap the frontal posteriorly and articulate more or less on its whole lateral length with the maxilla.   The anterior end of the nasal is produced into the *premaxillary process* which provides the shallow socket into which the nasal process of the premaxilla lodges.

Septomaxilla: The septomaxilla is a pair of convex bones lying inside of the nasal capsule and is best exposed by the removal of nasals and prevomers.   The bones form both the floor of the nasal capsule and the roof of the Jacobson's organ (Fig. 1).   The extreme anterior end of the bone is produced into a small, short, and pointed
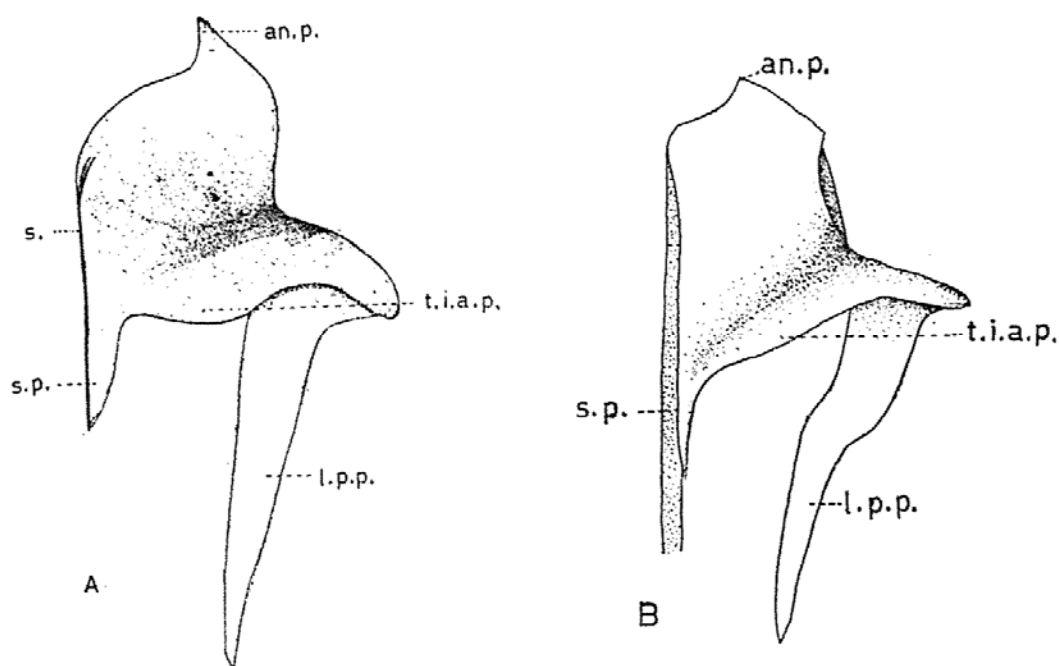

Fig. 12.   Ventral views of the left septomaxilla.   A. *H. bowringii* and B. *H. frenatus*.

anterior process. The outer border of the anterior process of the septomaxilla articulates with the rostral portion of the palatal shelf of the maxilla and the *transverse inferior alar process* articulates transversely across the anterior third of the prevomer, while the medial borders bound the parasphenoid. The medial border of the bone is raised into the *superior* and *inferior ledges* which continue to the posteriorly projecting flat septal process. The superior and inferior ledges are separated by a deep sulcus which permits the cartilaginous parasphenoid to run through. The posterior portion of the bone forms an inferiorly projecting transverse inferior alar process which forms the posterior borders of the Jacobson's organ. The lateral border is curved upward and is produced posteriorly into a long, laterally grooved *posterior process.*

D. *The Suspensorium*

The lower jaw is supported, on each side, by a pillar-like bone, the quadrate.

The only remnants of the palatopterygoid cartilage are the epipterygoid, the basitrabecular process of the basisphenoid, and the quadrate.

Quadrate: The quadrate is a comparatively massive bone lying on the outer side of the occipital complex; it forms the bridge for the lower jaw and cranium. It lies in an obliquely dorso-ventral direction in such a way that the ventral end is anterior to the dorsal end. Its dorsal end is directed backward and the ventral end is directed forward.

This bone is composed of three parts, the dorsal head, the body, and the ventral head. The dorsal head, *condylus cephalicus,* is elliptical. It articulates above with the squamosal and below with the paroccipital process of the opisthotic. The *body* of the quadrate consists of an inner rod-like portion and an outer expanded wing-like portion. The latter is convex and thin, with a marked concavity facing backward and downward. The ventral head of the quadrate, *condylus mandibularis,* bears a medial and a lateral *condylar facet* for the articulation with the mandible. The medial and lateral condylar facet are sepa-

rated from each other by an antero-posteriorly directed sulcus. Between the articular surface and the mandible, there is a meniscus of intercalary cartilage which provides the movement of the mandible. Close to the ventral head, along its internal border, the quadrate bears a facet for articulation with the pterygoid (Fig. 13).
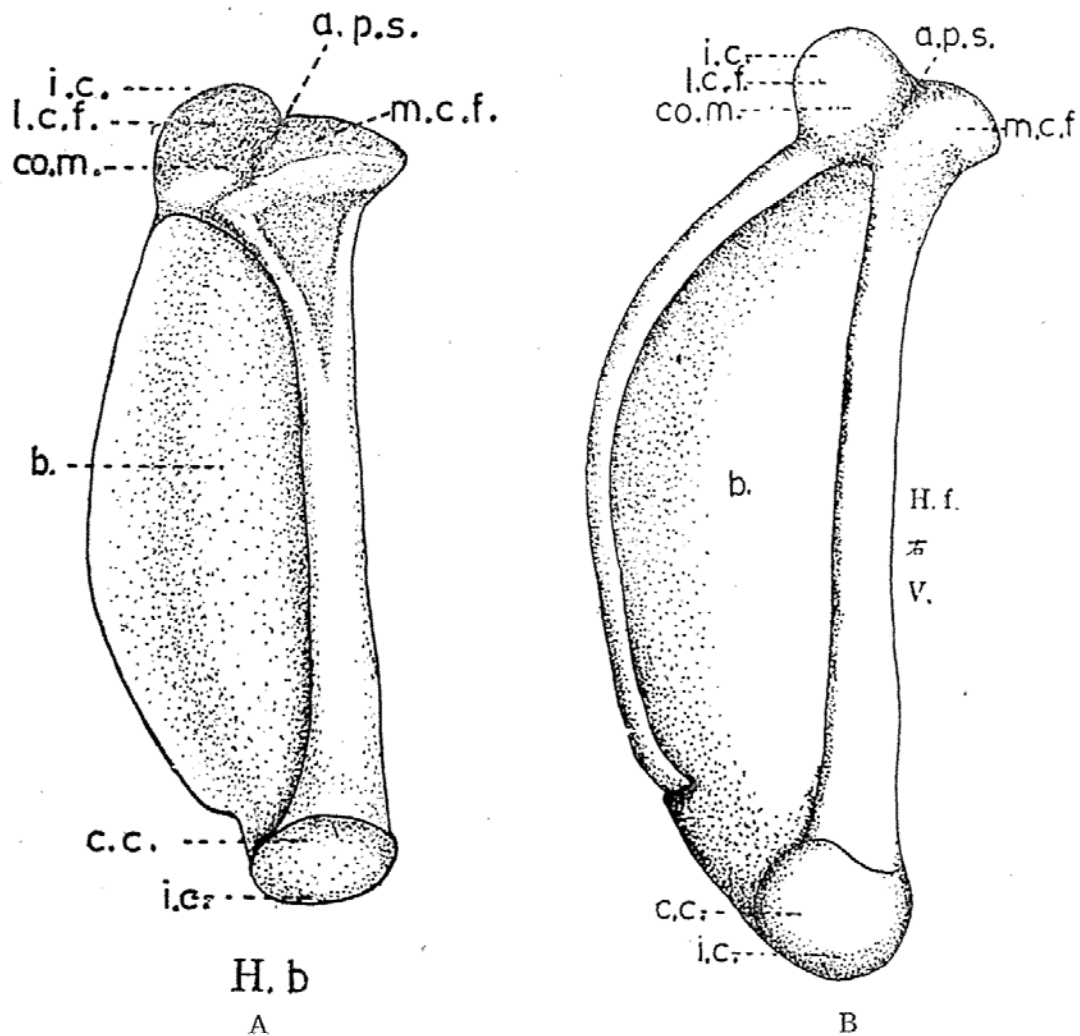

Fig. 13. Ventral view of the right quadrates. A. *H. bowringii* and B. *H. frenatus.*

Between the condylus cephalicus of the quadrate, the paroccipital process, and squamosal, there is a small meniscus of partially ossified cartilage called the *intercalary cartilage.* The cartilage provides the movement of the quadrate on the paroccipital process.

Squamosal: The squamosal is a small bone, its rounded ventral end articulating with the anterior surface of the paroccipital process

and with the condylus cephalicus of the quadrate. It curves slightly upward and forward to articulate with the outer margin of the supra-temporal process of the parietals along its grooved inner surface. The dorsal end of the bone is pointed; its lateral surface is also grooved more or less along its whole length (Fig. 1).

Epipterygoid: The paired epipterygoid (*columella cranii*) are slender and rod-shaped bones which are disposed in an obliquely dorso-ventral direction, the ventral end lying distinctly anterior to the dorsal end. The expanded calcified, cartilaginous, knob-like end fits against the lateral edge of the parietal and is also articulated to the anterior process of the prootic by a ligament, while the ventral end fits into a large socket (*fossa columellae*) at the medial edge of the dorsal surface of the quadrate process of the pterygoid.

E. *The Upper Jaw and Palates*

The upper jaw is formed by the maxilla and premaxilla, while the palate is formed by the maxilla, premaxilla, prevomer, pterygoid, palatine, ectopterygoid, and a small jugal on the posterior parts of each maxilla.

Pterygoid: The pterygoid is a Y shaped bone, uniting the palatine and ectopterygoid with the quadrates. It forms a more or less flat plate in front and a long outwardly directed rod-like process behind. The flat plate is produced in front into a *palatal process* medially,

Fig. 14. Dorsal view of the left side of tabular bone of the *H. frenatus.*

which is overlapped by the *pterygoid process* of the palatine in dorsal view, and laterally into an *ectopterygoid process* which is overlapped by the ectopterygoid in dorsal view.

The raised ridge on the ventral side of the ectopterygoid process continues to the outer border of the flat plate. The ectopterygoid process and the lateral part of the anterior margin of the flat plate form the posterior border of the suborbital fenestra. The rod-like *quadrate process* is the longest one and rests posteriorly against the inner border of the quadrate, close to its lower end, in such a way that the articulation is movable with the pterygoid sliding on the quadrate.
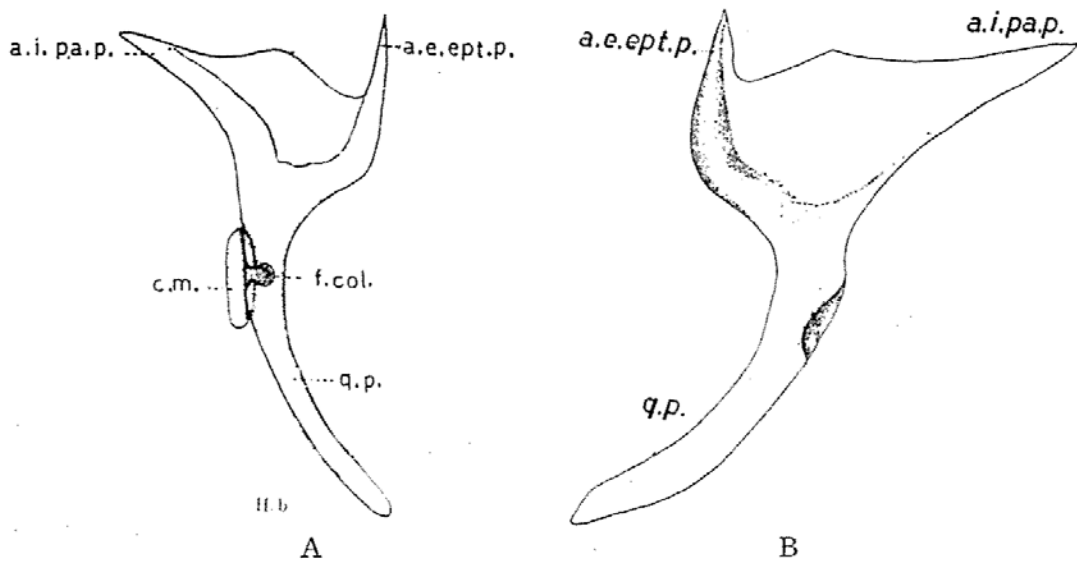

Fig. 15. Right pterygoid. A. Dorsal view of right pterygoid of young *H. bowringii*. B. Ventral view of right pterygoid of adult *H. frenatus*.

An inner border of the anterior part of the quadrate process of the pterygoid is deeply grooved. Its dorsal border extends medially into a large, thin cartilaginous wing in young specimens but not in the adult. This groove provides the surface for the attachment of the ligament that unites the pterygoid with the basitrabecular process of the basisphenoid. On the dorsal surface, immediately above the groove, there lies a round depression, the *fossa columellae*, into which fits the lower end of the epiterygoid (Fig. 15).

Ectopterygoid: The ectopterygoid is a small, flat and outwardly curved bone connecting the pterygoid to the posterior process of the maxilla. It is pointed at both ends and encloses nearly all of the lateral border of the sub-orbital fenestra. The lateral margin of the anterior ramus articulates with the palatal shelf of the maxilla, and the pointed anterior end articulates with the palatine and prefrontal. The posterior ramus overlaps the ectopterygoid process of the pterygoid on dorsal aspect.

Palatine: The palatine is a more or less quadrangular bone lying in front of the pterygoid. It is greatly concave on the ventral surface and is produced in front into a *prevomerine process*, medially, and into a *maxillary process*, laterally. The prevomerine process fits into the *palatine notch* of the prevomer and its base articulates dorsally with the medial frontal process of the prefrontal. The maxillary process articulates laterally with the palatal shelf of the maxilla by means of its lateral shallowed groove and at its base with the medial frontal process of the prefrontal and ectopterygoid. These two processes and the anterior border of the palatine form the posterior boundary of the internal nares. The posterior portion of the palatine is flat and is perforated by the *palatine foramen*. It is produced postero-medially into a short *pterygoid process* which overlaps the palatine process of the pterygoid at the dorsal side. The more or less straight posterior border of the palatine articulates with the pterygoid, while its lateral border forms the inner border of the sub-orbital fenestra.

Prevomer: The paired prevomers lie in front of the palatine which forms the floor of the olfactory capsule and Jacobson's organ, and the anterior part of the roof of the mouth cavity. When viewed from the ventral side, the medial border is shallowly depressed and forms the mid-longitudinal shallow furrow with the counter part of the opposite prevomer. The remaining part of the bone is divided by the transverse shallow groove into anterior and posterior and posterior convex portions, the transverse shallow groove is pierced by a *prevomerine foramen*. The *incisive foramen* is enclosed by the anterior medial borders of the prevomers. The anterior one-third

of the prevomer overlaps along the midline with its counterparts from the opposite side (Fig. 2). The antero-lateral edge of the pre-vomer is produced dorsally and ventrally into slender ridges which are separated by the *transverse sulcus* or *articular groove* to accomo-date the palatal shelf of the maxilla. Immediately posterior to the large antero-lateral articulation with the palatal shelf there is an indentation for the *inner opening of the Jacobson's organ*. Further caudate, the prevomer gradually widens, to form the medial border of the internal nares. The posterior margin is greatly indented; it is called the *palatine notch* which accomodates the prevomerine process of the palatine. This notch divides the posterior portion of the prevomer into the *postero-lateral* and *postero-medial processes*. The postero-lateral process is pointed and descends slightly caudally. It extends more caudate than the postero-medial process which is broad and plate-like in appearance.

When viewed from the dorsal side, the medial border is higher than the remaining portion which is divided into anterior and posterior concave portions, of which the anterior one forms the floor of the
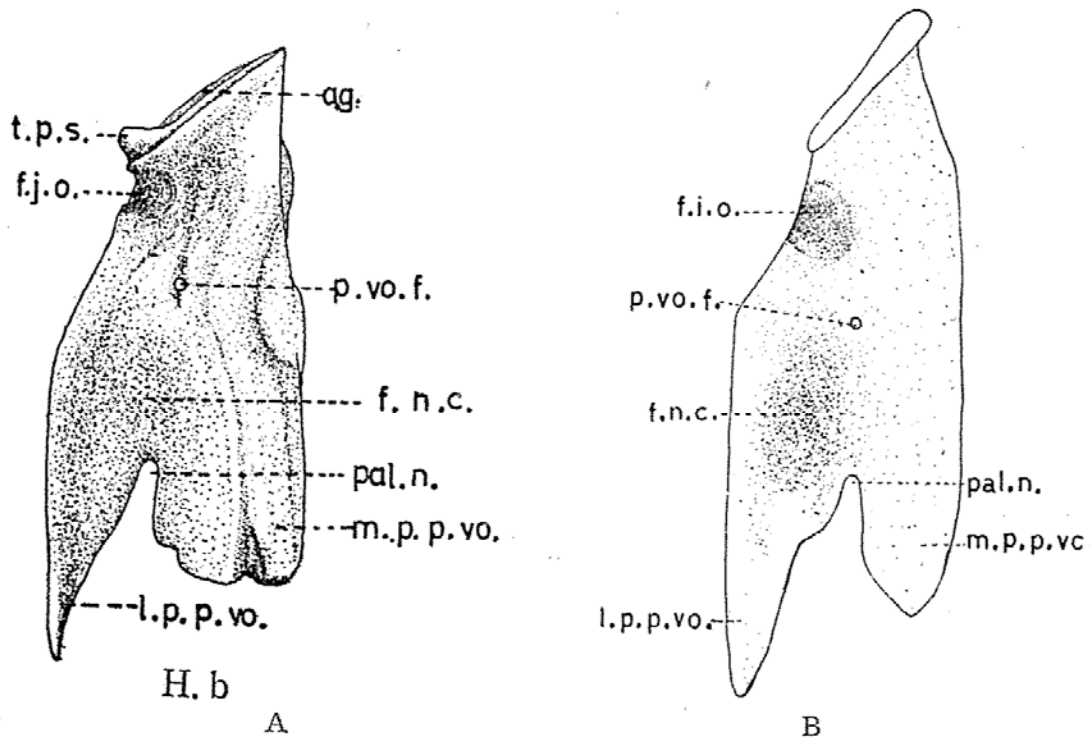

Fig. 16. Dorsal view of prevomer. A. left prevomer of *H. bowringii* and B. right prevomer of *H. frenatus*.

nasal capsule. The lateral corner of the dorsal ridge of the antero-
lateral edge of the prevomer is more highly developed in the adult,
which projects into the ventral concavity of the septomaxilla (Fig. 16).
The septomaxilla articulates with the prevomer by means of a
transverse inferior alar process.

Maxilla: The paired maxillae are the large bones which occupy
a major portion of the sides of the snout. They form the lateral
and ventral borders of the external nares and the lateral borders of
both the inner opening of the Jacobson's organ and internal nares.
The outer surface is smooth, dorsally curving slightly toward the
midline. The maxilla is composed of two portions: (1) the vertical
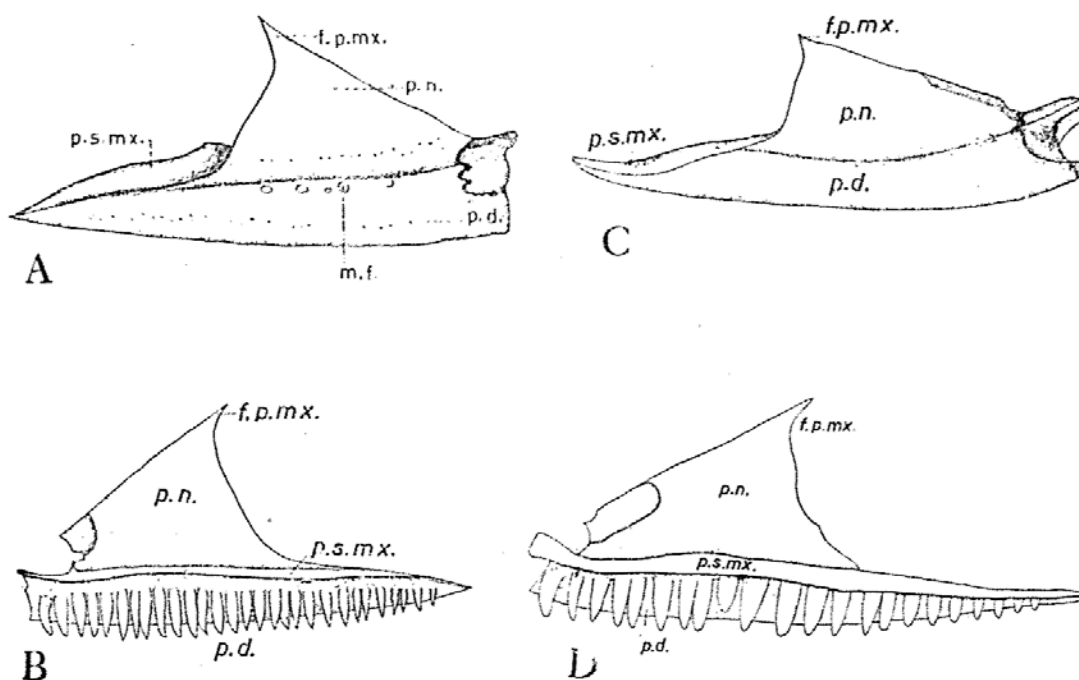lateral portion and (2) the palatal shelf portion.

Fig. 17. Maxilla of *Hemidactylus*. A. Lateral view and B. Inner view of
the maxilla of *H. bowringii*. C. Lateral view and D. Inner view
of the maxilla of *H. frenatus*.

The vertical lateral portion of maxilla is composed of two parts:
(1) the triangular dorsal *pars nasalis* and (2) the ventral *pars dentalis*.
Pars nasalis gives off a pointed frontal process dorsally which
overlaps the frontal and prefrontal and articulates with the nasal
dorsally and overlaps the prefrontal along its posterior margin; its

anterior border forms the lateral boundary of the external nares.
The portion forming the lateral wall of the vestibule of the nasal
passage is shallowly grooved internally.   The ventral pars dentalis,
which bears a number of conical teeth ankylosed to its inner aspect,
articulates anteriorly with the premaxilla and posteriorly with the
jugal.

The palatal shelf is wide and perpendicular to the almost vertical
lateral portion of the maxilla, at a level with the ventral margin of
the external nares.   The shelf runs almost the whole length of the
maxilla.   Its inner margin is waved and its width decreases only
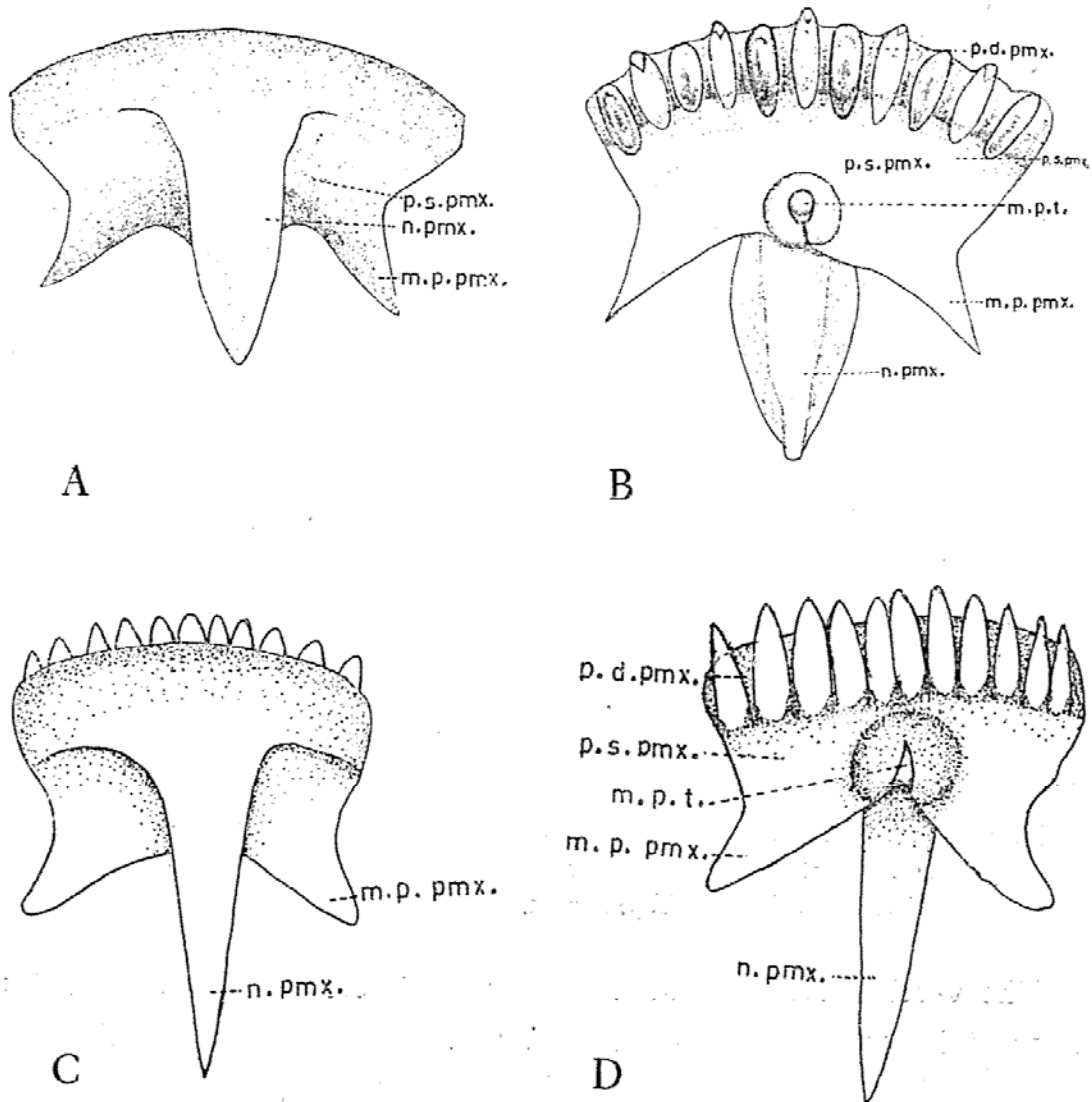

Fig. 18.   Premaxilla.   A. Dorsal view and B. Ventral view of *H. bowringii*.
C. Dorsal view and D. Ventral view of *H. frenatus*.

gradually along the large posterior *maxillary process* (Fig. 2). Antero-ventrally, it is overlapped by the maxillary process of the premaxilla. Antero-medially, it fits into the articular groove of the anterior edge of the prevomer. Antero-dorsally, it articulates with the septomaxilla; postero-medially, with the maxillary process of the palatine and ectopterygoid; and postero-dorsally along the posterior maxillary process, with the prefrontal and jugal.

The pars dentalis of the maxilla is tunnelled through by several *maxillary foramina (nasalis alveolaris superior)*.

Premaxilla: The premaxillae of the two sides are united to form a single medial premaxilla which lies at the anterior end of the skull and gives off a moderate medial convex, pointed process, the *nasal process (processus nasalis)*. This process forms the median boundary of the external nares, and its distal half overlaps the premaxillary process of the nasal. Its distal end is wedged in between the nasals. The body of the premaxilla consists of the parts; (1) the teeth bearing *pars dentalis* and (2) the *palatal shelf* which is perpendicular to the pars dentalis and forms the ventral border of the external nares. The pars dentalis bears eleven conical teeth ankylosed to its inner side. The palatal shelf is produced posterolaterally into a pair of the short triangular *maxillary processes*. From the ventral aspect, the maxillary processes overlap the palatal shelves of the right and left maxilla. The mid-posterior edge of the palatal shelf of the premaxilla is notched and elevated ventrally to form a socket for conical median teeth.

The premaxilla articulates with the septomaxilla, maxilla, and nasal.

F. *Lower jaw*

Each ramus of the lower jaw consists of the following 5 separate elements: (1) dentary, (2) splenial, (3) coronoid, (4) surangular and (5) articular (with a fused prearticular and angular).

Dentary: The dentary is a tubular bone bearing teeth on the inner dorsal margin. It forms the anterior half of the mandible. When viewed medially, it increases from the *symphysis* to a maximum
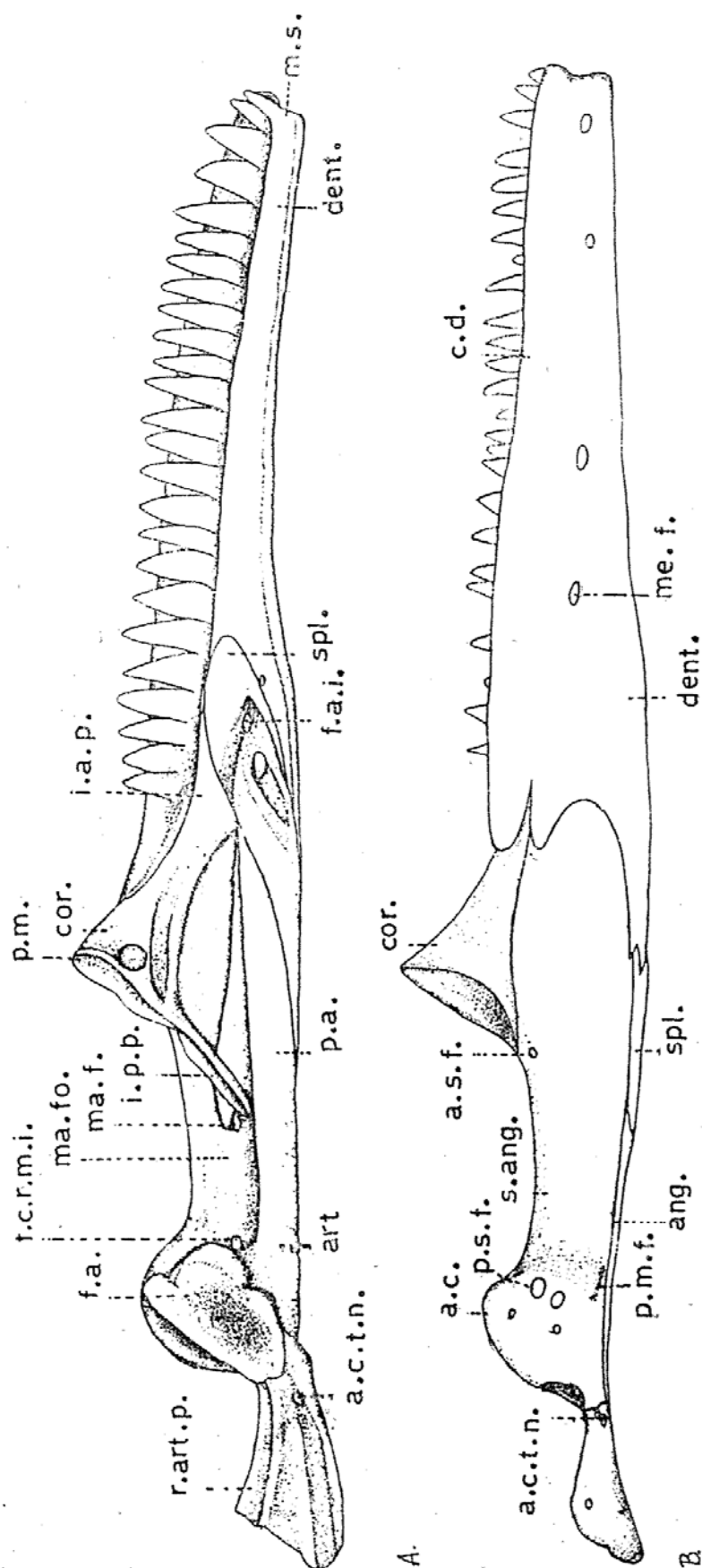
Fig. 19.   The mandible of *H. bowringii*. A. inner view, B. outer view.

at the posterior margin. Laterally, the posterior margin of the dentary is produced posteriorly into three large pointed processes: the superior one overlaps the anterior outer process of the coronoid; the middle one overlaps the surangular; and the inferior one overlaps the surangular and splenial. The teeth are ankylosed to the labial wall and grow upwards from the *crista dentalis*. Medially, the posterior margin of the dentary also protrudes into three pointed processes. The superior one is overlapped by the coronoid; the medial one overlaps the coronoid but is overlapped by the splenial; and the inferior one is overlapped only by the splenial. There is a foramen between the dentary and splenial on the inner side of the ramus, through which the *nervous alveolaris inferior* passes out. Laterally, the dentary bears 4 *mental foramina* which parallel the level of the medially located crista dentalis. The bone is canalized along its whole length by the nervous alveolaris inferior which give off several branches, each coming out of one of the 4 mental foramina. The inner surface of the anterior end of the dentary is slightly flattened and fits against a similar surface of the dentary from the other side to form the *mandibular symphysis (symphysis mandibularis)*.

Splenial: The splenial occupies the medial, ventral, and lateral aspect of the mandible. The majority of the body of the splenial occupies the ventral middle third of the inner surface of the mandible. Medially it overlaps the dentary, coronoid, and prearticular portion of the articular. It bears two foramina for the passage of the nervous alveolaris inferior.

Coronoid: The coronoid is a triangular element straddling the dorsal central third of the mandible by means of its *inner anterior process, outer anterior process,* and *inner posterior process*. The ventral edge of the thin inner anterior process is overlapped by the inner middle process of the dentary and splenial, and at the same time it overlaps the inner superior process of the dentary. The short outer anterior process overlaps the outer superior process of the dentary on the outer side. The inner posterior process overlaps the surangular and prearticular on the inner side. The coronoid projects upwards in the form of a *processus messetericus*.

Surangular: The surangular forms the lateral wall of the major posterior part of the mandible and is overlapped by the posterior margin of the dentary and the splenial. Ventrally, it articulates with the angular. It is sword-shaped because its anterior part is pointed. The surangular forms the anterior, lateral, and posterior margins of the *mandibular fossa (fosseus mechelli).* The interior and lateral edge of the articular condyle completes the roof and lateral wall of the *Meckel's canal.* There are two foramina on the inner side of the bone. The *mandibular foramen* is located dorsally to the anterior margin of the mandibular fossa. Passing through this foramen, the main trunk of the mandibular division of the 5th cranial nerve and mandibular artery enter the lower law, while the mandibular vein comes out from this foramen. The other foramen lies just superior to the closed posterior end of the mandibular fossa and into which enter, from the inner surface, the nervous cutaneous recurrence maxillae inferior branch of the mandibular division of the 5th cranial nerve. This nerve comes out to the outer surface through one or more foramina, *posterior surangular foramen,* near the opposite side of the leading-in foramen and innervates the skin of this region. One branch of the mandibular nerve comes out through a foramen, *anterior surangular foramen,* on the outer surface of the surangular near the coracoid. The other branch of the mandibular nerve comes out through a series of slit-like foramina, posterior *myelophygoid foramen.* These foramina are located just anterior and ventral to the posterior surangular foramen.

Articular: The articular forms the posterior portion of the mandible. It consists of the prearticular and the ossified Meckel's cartilage. The *Meckel's cartilage* consists of the large dorsal prominence *(articular condyle)* which contains the *articular facet* anteriorly and the posterior *retroarticular process* which is ankylosed by the articular cartilage on its posterior margin. The retroarticular process forms the point of attachment for the ventral terminal projection of the epihyal and serves to form the ventral boundary of the tympanic membrane. The prearticular is a piece of the elongated, pointed bone visible on the inner side of the mandible, which projects from the

Meckel's cartilage. Its anterior border is overlapped by the splenial. The prearticular forms the inner wall and floor of the mandibular fossa and supports the Meckel's canal. Near the base of the articular facet, on the inner side of mandible, there is an aperture for the entrance of the chorda tympani branch of the 5th cranial nerve. This nerve comes out through two foramina just on the opposite side of the leading-in foramen.

Angular: The angular is represented by a strip of bone on the ventral side of the surangular, which articulates with the articular. The anterior half length of the bone is overlapped by the ventral margin of the splenial when it is seen from the outside.

G. *Teeth*

The teeth are of the undifferentiated conical pleurodont type, and are ankylosed to the inner wall of the mandible, premaxilla, and maxilla. The teeth are replaced successively. The replacements of the teeth are beneath the older teeth. So, on the same area successional teeth may be seen in varying sizes and stages of replacement of the adult teeth.

The premaxillary teeth are 11–12, the maxillary teeth vary from 22 to 29. The mandibular teeth are 31 in one specimen.

H. *The Temporal Fossa and other Large Vacuities*

On the temporal region, there are two vacuities: (1) *lateral occipital fenestra (post-temporal forra)* which is bordered by the parietal, squamosal, prootic, and paroccipital process of the opisthotic, and (2) the posterior *cranio-pterygoid vacuity* which is incompletely bordered anteriorly by the basipterygoid process of the sphenoid, laterally by the pterygoid and quadrate, posteriorly by the paroccipital process of opisthotic, and medially by the opisthotic, prootic, and basisphenoid. The *superior temporal fossa* and *inferior temporal fossa* has not been examined due to the missing jugal-quadratojugal bar and the postorbital-squamosal bar.

On the frontal region there are one fossa and two vacuities: (1) the *supraorbital fossa* which is bordered by the prefrontal in front

and the frontal and postfrontal behind, but incomplete laterally, (2) the *sub-orbital fenestra* which are two elongated oval apertures lying beneath the optic capsule, one on each side, surrounded by the pterygoid, ectopterygoid, and palatine bones, and (3) the *interpterygoid vacuity* (*incisura piriformis*) which is bounded by the prevomer, anteriorly, palatine and pterygoid, laterally, and basisphenoid, posteriorly. In front of the interpterygoid vacuities there is a pair of elongated openings, the posterior portions of which form the choana or internal nares.

I. *Hyoid Apparatus*

The hyoid apparatus of the *H. bowringii* is formed by the 2nd and 3rd *visceral arches*. The 1st *ceratobranchial* is heavily ossified and the *glossohyal* and *basihyal* are ossified to a slightly lesser extent. The remainder of the apparatus is unossified, but the anterior border
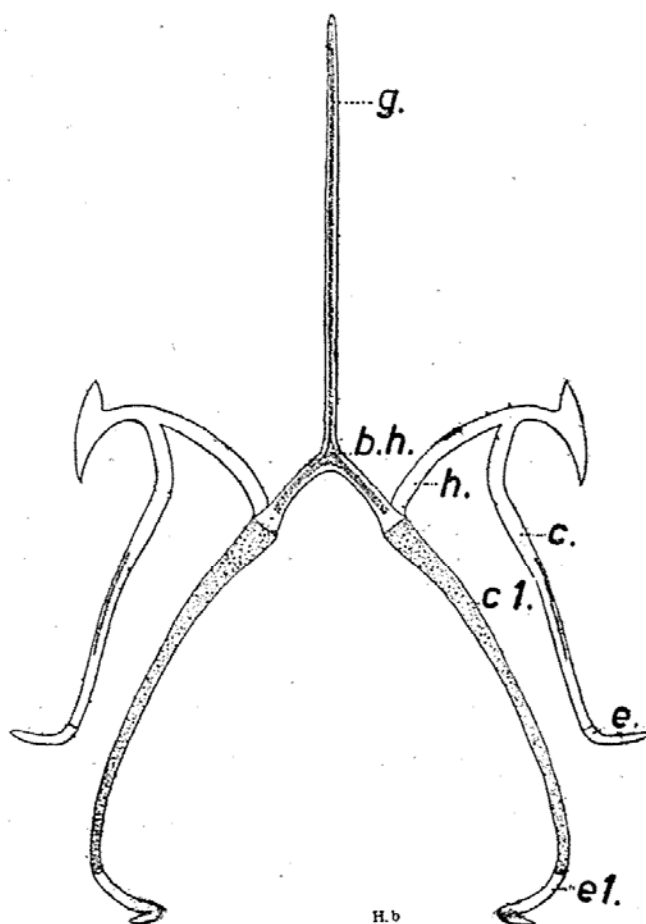

Fig. 20. Ventral view of the hyoid apparatus of *H. bowringii*.

of the middle portion of the *hypohyal* and the lateral border of the middle portion of the *ceratohyal* are ossified.

The thread-like glossohyal extends anteriorly from the basihyal into approximately half the length of the tongue. Dorsal to the proximal portion of the glossohyal, there lie the *cricoid* and *arytenoid cartilages*.

The 2nd visceral arch forms the hypohyal, the lateral descending ceratohyal, and the terminal projection, the *epihyal*. The epihyal attaches to the lateral end of the paroccipital process by the short ligament and the posterior margin of the crest of the retroarticular process of the articular.

The 3rd visceral arch forms the heavily ossified *cerato-branchial* and *epibranchial*. This superficially located visceral arch has no direct attachment to the skull. The terminal dorsal projection of the epibranchial parallels the epihyal and terminates far back of the paroccipital process.

2. Vertebral Column

The vertebral column of the genus *Hemidactylus* consists of six regions: (1) the *cervical* or *presternal* which consists of eight vertebrae, of which the posterior five bear ribs, (2) the *anterior thoracic*, which consists of three vertebrae with ribs connected to the sternum, (3) the *posterior thoracic*, which consists of the successive fourteen vertebrae with free ribs, (4) a *lumbar* which bears no rib, (5) the *sarrals*, consisting of two vertebrae giving attachment to the pelvic girdle and (6) the *caudal vertebrae*, consisting of five *pre-caudals* (*pygals*) and a variable number of *postcaudal vertebrae*. The first 4 regions are sometimes called *presacrals*.

Atlas: The atlas is a ring shaped bone and consists of three separate parts: the ventral, smallest *hypocentrum* (*first intercentrum*), and the dorso-lateral *neurapophyses* on each side. The centrum of the atlas has been transferred to the axis. The hypocentrum is the smallest of these three pieces and bears a process projecting downward and slightly forward. The neurapophyses are rather large. They are curved upward and mediaward to house the *neural canal*
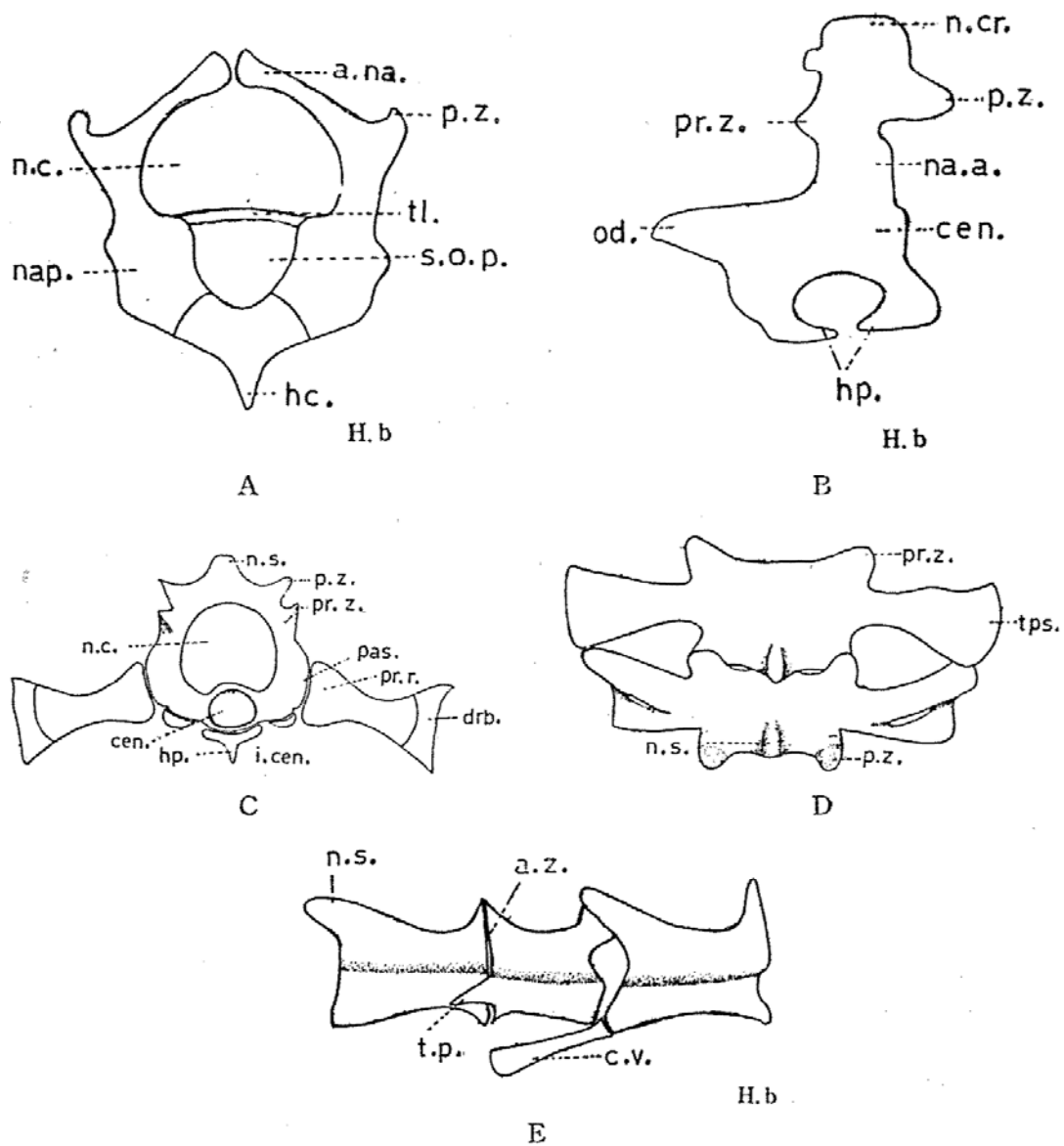
Fig. 21. Vertebrae of *H. bowringii*. A. anterior view of the atlas. B. lateral
view of the axis. C. cervical vertebrae 4, frontal view. D. dorsal
view of the sacral vertebrae. E. lateral view of the postcaudal
vertebrae.

and they articulate to the dorso-lateral surface of the hypocentrum
by ligament. The neurapophyses are divisible into a ventral massive
part (*neural arch pedicel*) and the dorsal thin plate part. The anterior
surface of the ventral massive part of neurapophyses, together with
that of the hypocentrum, form the *semicircular articular facet* to
articulate with the occipital condyle of the skull. On the posterior
surface of the same region, they develop an *articular facet* to articu-

late with the odontoid process of the axis. The dorsal plates of the
neurapophyses curve mediaward to form the side and the roof of the
neural canal but are separated from each other on the middorsal line.
The neurapophyses bear a small process projecting dorso-laterally
and backward, which means in opposition to the prezygapophyses of
the axis, though not in contact with each other. The process is
homologous to the postzygapophyses of the following vertebrae.

The space enclosed by the bones of the atlas is divided into two
parts by the transverse ligament connecting the neurapophyses. The
dorsal one is a neural canal and the ventral one serves to accomodate
the odontoid process of the axis.

Axis: The second cervical vertebra differs from the other
vertebrae. The centrum of the axis is *amphicoelous*. The posterior
surface is concave and the anterior surface fuses indistinguishably
with the base of the *odontoid process* (the centrum of the atlas) in
the adult. The neurapophyses on each side meet middorsally to form
a prominent longitudinal *neural spine* (*neural crest*). The *prezygapo-
physes* are non-functional and the *postzygapophyses* articulate with the
prezygapophyses of the third cervical vertebra.

There are two intercentra bearing *hypapophysis*. The anterior
one (2nd intercentrum) articulates with both the base of the odontoid
process and the base of the axis centrum and these bones tend to
fuse in the adult. The posterior one (3rd intercentrum) articulates
with the base of the axis centrum in the young, but tends to fuse
with the base of the axis centrum in the adult. The anterior
hypapophysis is directed backward while the posterior one is directed
forward.

Other Presacrals: These vertebrae are *amphicoelous* throughout.
The neural spines increase in height posteriorly. On the other hand,
the vertebrae increase in length and width caudally but the posterior
three segments of the posterior thoracics decrease in width caudally.

The third cervical vertebrae is shorter than the following ones.
Although it bears no ribs, it has the obscure condyle (*parapophysis*)
on each side. The last presacrals bearing no ribs has no condyle for
the ribs; it is shorter and broader than the preceding presacrals.

The neurapophysis on each vertebra is notched both in front and behind. The large *intervertebral foramen* is enclosed on each side between the neural arches of any two continuous vertebrae for the exit of the spinal nerve. They articulate by means of the centra and also through the prezygapophysis and postzygapophysis. The anteriorly directed prezygapophysis is large and cup-shaped and with a dorso-medially directed articular facet which articulates with the ventro-externally directed articular facet of the posteriorly directed postzygapophysis of the preceding vertebra. A pair of small *subcentral foramina*, lying on the ventral aspect of the centrum for the passage of the blood vessels, occurs in all presacral vertebrae except the atlas.

The intercentra are small bones, lying interventrally between the centra. They fuse with the axis and sacrum but are free on the remaining vertebrae. The intercentra between the third and fourth, fourth and fifth, fifth and sixth, and sixth and seventh cervical vertebrae bear hypapophysis directed downward and forward to articulate with the ventral surface of the proceeding vertebrae.

The ribs of the fourth, fifth, and sixth cervical vertebrae consist of a short bony portion and a distal forked cartilaginous portion. The bony portion is flat and expanded both on their proximal and distal ends. The ventral ramus of the forked cartilaginous portion is longer than the dorsal ramus. The ribs of the seventh and eighth cervical vertebrae are broader, proximally and slender distally. The cartilaginous portion on the distal end of the bony portion is single and pointed. The ribs of the following vertebrae are normal. The ribs of the vertebrae IX-XI are connected to the sternum and xiphisternum by the cartilaginous *sternal ribs.* The first two pairs of these articulate directly with the postero-lateral borders of the sternum, while the remaining pair connects to the xiphisternum. The ribs of the twelfth to the twentieth vertebrae are free ventrally and shorter posteriorly. They are also composed of the proximal bony and distal cartilaginous portions. The last presacral vertebrae has no ribs and may be classified as the lumber vertebrae.

Sacrals: There are only two sacral vertebrae in these animals.

They are characterized by the presence of the large, expanded transverse process which is directed outward. The anterior process is greatly expanded distally into a tough articular facet for the ilium. The posterior process is curved forward to meet the distal end of the anterior process and houses a large foramen between them which bears a thin projecting plate along its caudal border. The distal extremities of the processes are broad and each bears a small articular facet for the ilium. Like the presacral vertebrae, the subcentral foramina are present on the sacrum.

Caudals: The caudal vertebrae are divided into two groups: the *pre-caudal vertebrae* (or *pygal*) are five in number and located immediately behind the sacral vertebrae; the *post-caudal vertebrae* lie in the autotomous part of the tail.

The precaudal vertebrae have no autotomy segments. The *transverse processes* are present in all precaudals, which are dorso-ventrally flattened and shorter posteriorly. The *chevron bones* are present between the third and fourth, and fourth and fifth precaudals and are Y-shaped. These chevron bones contain the *haemal canal* for the passage of the caudal artery and vein. The postcaudal vertebrae is divided into the anterior half and posterior half sections by an *autotomy zone*. The transverse process of the postcaudals is present in the first seven but is very short. The Y-shaped chevron bones are also present in the first seven postcaudals and they also contain the haemal canal for the passage of the caudal artery and vein and are attached to the ventral aspect of the intervertebral joint. The remaining caudal vertebrae decrease gradually in size and become rod-like in the distal end of the tail.

3. The Sternum

The *sternum* is a calcified cartilaginous rhomboidal plate with flanges on the anterior border to receive the epicoracoid. The posterior border is attached to two pairs of sternal ribs which articulate with the first and second pair of the thoracic ribs. The *xiphisternum*, attached to the posterior tip of the sternum, is a calcified cartilage which gives rise to two posterior cornua, of which

the outer one articulates with the third pair of the thoracic ribs and the inner one is short and free.

4. Appendicular Skeleton

A. *The Pectoral Girdle*

The *pectoral girdle* is formed of the median unpaired *interclavicle*, paired *clavicles, epicoracoides, scapulo-coracoides* and partially calcified *suprascapulae*. The cruciform interclavicle connects to the sternum with the clavicles. Portion of the interclavicle lying attached to the ventral surface of the antero-median part of the sternum is covered ventrally by the clavicle at the anterior tip. Of its four arms, the posterior one is the stoutest, while the anterior and lateral ones are rather slender. The two lateral arms are obliquely curved forward and articulate with the posterior border of the clavicle. All of the arms are obtusely pointed.

The epicoracoids are calcified cartilaginous flat plates. They are movably articulated to the flange of each side of the anterior border of the sternum but immovably articulated to the coracoid by their outer border. The medial border of each side of the epicoracoids do not meet in the mid-longitudinal line on the dorsal side of the inter-clavicle. They are broad in front and narrow behind. Each epi-coracoid has, at its anterior outer end, a recurved prolongation which unites with the *primary coracoid ray* of the coracoid and becomes the anterior border of the *primary coracoid fenestra.*

The clavicles are flat and curved bones with their medial part dilated and perforated by a large ovoid *clavicular fenestra.* The medial ends are attached to the ventral surface of the anterior area of the interclavicle and nearly in contact with each other, but the distal ends are connected to the notch on the ventro-anterior part of the suprascapula

The coracoids are a pair of thin convex bones with the curved inner border which articulates with the epicoracoid. Its dorsal end unites to the scapula and bears a small *supracoracoid foramen* for the passage of the nerve going to the forearm. Two rays project

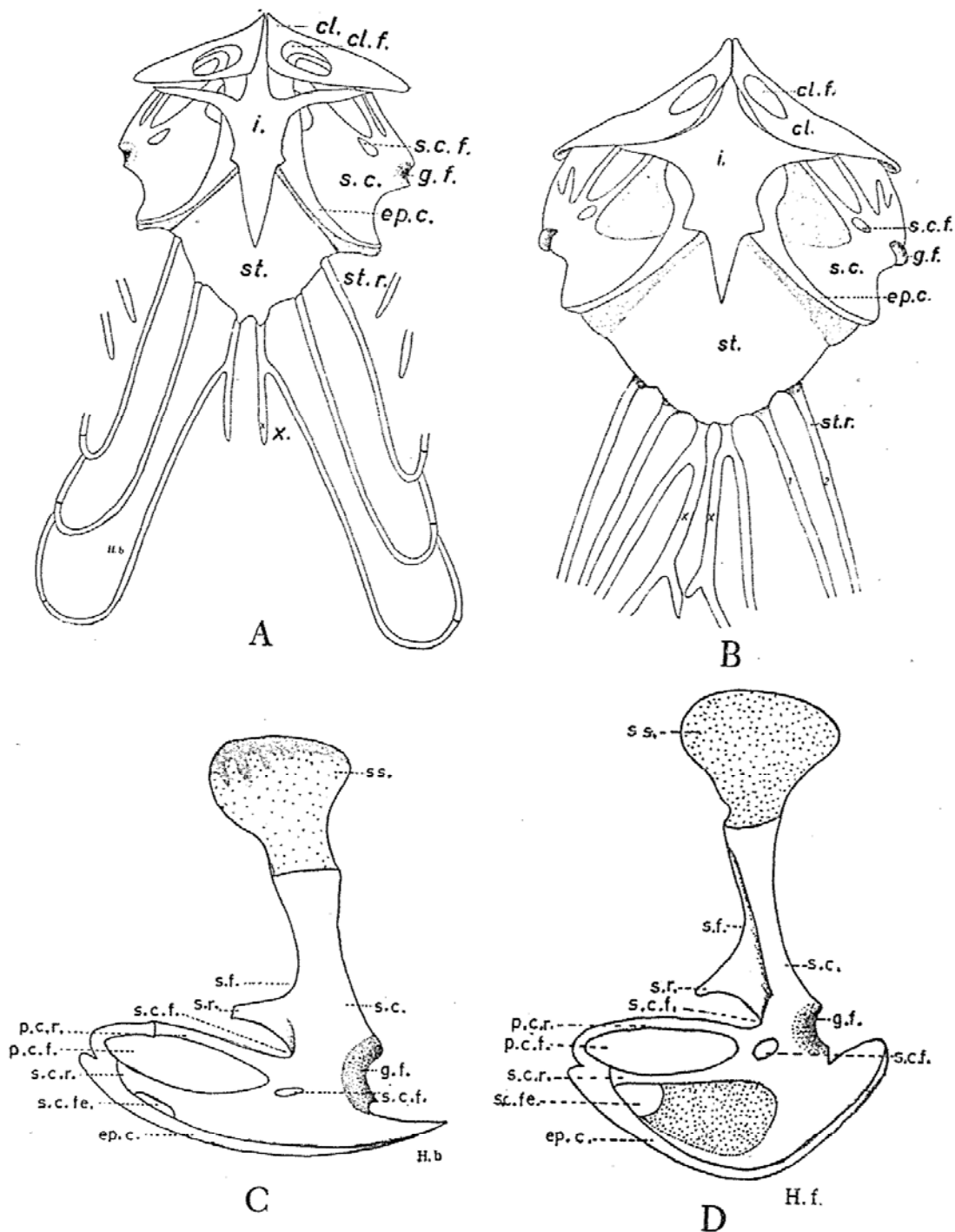Fig. 22. A and B. Ventral view of the sternum and the pectoral arch of *H.*
bowringii and *H. frenatus* respectively. C. and D. Lateral view of the
pectoral arch of *H. bowringii* and *H. frenatus* respectively.

forward from the coracoid: (1) the dorsal *primary coracoid ray* and
(2) the ventral *secondary coracoid ray*. There is a large *primary*
coracoid fenestra between the primary and secondary coracoid ray,

and it is bordered anteriorly by the epicoracoid. A small *secondary coracoid fenestra* lies between the secondary coracoid ray and the epicoracoid. The coracoid forms the posterior half of the glenoid fossa, the anterior half of which is formed by the scapula.

The scapula situates dorsal to the glenoid fossa and is fused to the coracoid with its proximal end. It is a flat and bar-like bone lying in a vertical plane and participating in a formation of the glenoid fossa. It bears a triangularly shaped process on its anterior surface. This process represents the *scapula ray* (*mesocoracoid* or *acromial lobe*).

The suprascapula is a broad and flattened plate; it is mainly cartilaginous but partially ossified. It is directed obliquely inward from the scapula and covers the fifth to seventh cervical ribs. Its dorsal region is quite broad and thin but the ventral region is narrow and bears a facet for the articulation of the clavicle.

B. *Fore Limbs*

Humerus: The shaft of the humerus is cylindrical and expands at its extremities. The proximal end is a rounded head which fits into the glenoid fossa of the scapulocoracoid. There are two crests near the head for the attachment of the muscles. On the preaxial surface the *deltoid crest* is less developed than the pectoral crest on the postaxial surface. There is a deep depression, the *bicipital fossa*, between the head and the *pectoral crest*. The distal end of the humerus forms the areas of articulation with the radius and ulna. The *capitulum* or *radial condyle* is preaxial in position and articulates with the radius. The *trochlear* or *ulnar condyle* is postaxial in position and articulates with the ulna. A linearly shaped *ectepicondylar foramen* lies beside the wing-like expansion on the preaxial border near the capitulum.

Radius: The radius and ulna lie nearly parallel with each other. The preaxial radius is shorter and more slender than the postaxial ulna.

The radius is a rod shaped bone; it bears the concavity at its proximal end to articulate with the capitulum of the humerus. The

straight shaft terminates in *pseudepiphysis* which articulates with the shallow groove of the radiale.

Ulna: The *oleclanon process* at the proximal end of the ulna projects postaxially and bears the concave fossa (*sigmoid fossa*) for the articulation of the trochlea of the humerus. On the preaxial surface of the head of the ulna at the level of pseudepiphysial plate there is a shallow articular facet for the articulation of the head of the radius. The opposing facet of the radius is also obscure. It expands distally to the pseudepiphysis which articulates with the shallow depression of the ulnare. On the postaxial surface the pseudepiphysis articulates with the pisciform. There is a small ossification, the *brachial patella* (*patella ulnaris*) between the olecranon process and the humerus.

Carpus: The carpus consists of three rows of indistinct bones. The proximal row is formed of three bones, i.e. radiale, ulnare and pisciform; the middle row is represented only by a centrale, and the distal row consists of carpals I-V. The *intermedium* is absent. The *radiale* articulates proximally with the radius, postaxially with the centrale, and distally with the first carpals and first metacarpal through the small articular facet. There is a small protuberance on the distal region of the preaxial surface of the radiale. The *ulnare* provides a concavity on the postaxial surface for the articulation with the ulna. Preaxially, it articulates with the centrale and distally, provides a concavity for the articulation with the fourth and fifth carpals. The *centrale* is an elongated bone, a compressed preaxial-postaxial axis between the ulnare and radiale. Distally and postaxially it articulates with the first to the fourth carpals. The *pisciform* bone is a small ovoidal bone articulating independently with the ulna. A small rounded first *carpal* articulates proximally with the radiale and centrale, distally with the first metacarpal and postaxially with the second carpal. The second and third carpals are larger than the first carpal and articulate proximally with the centrale. The fourth carpal is largest and articulates proximally with the centrale and ulnare. The fifth carpal articulates proximally with the ulnare.
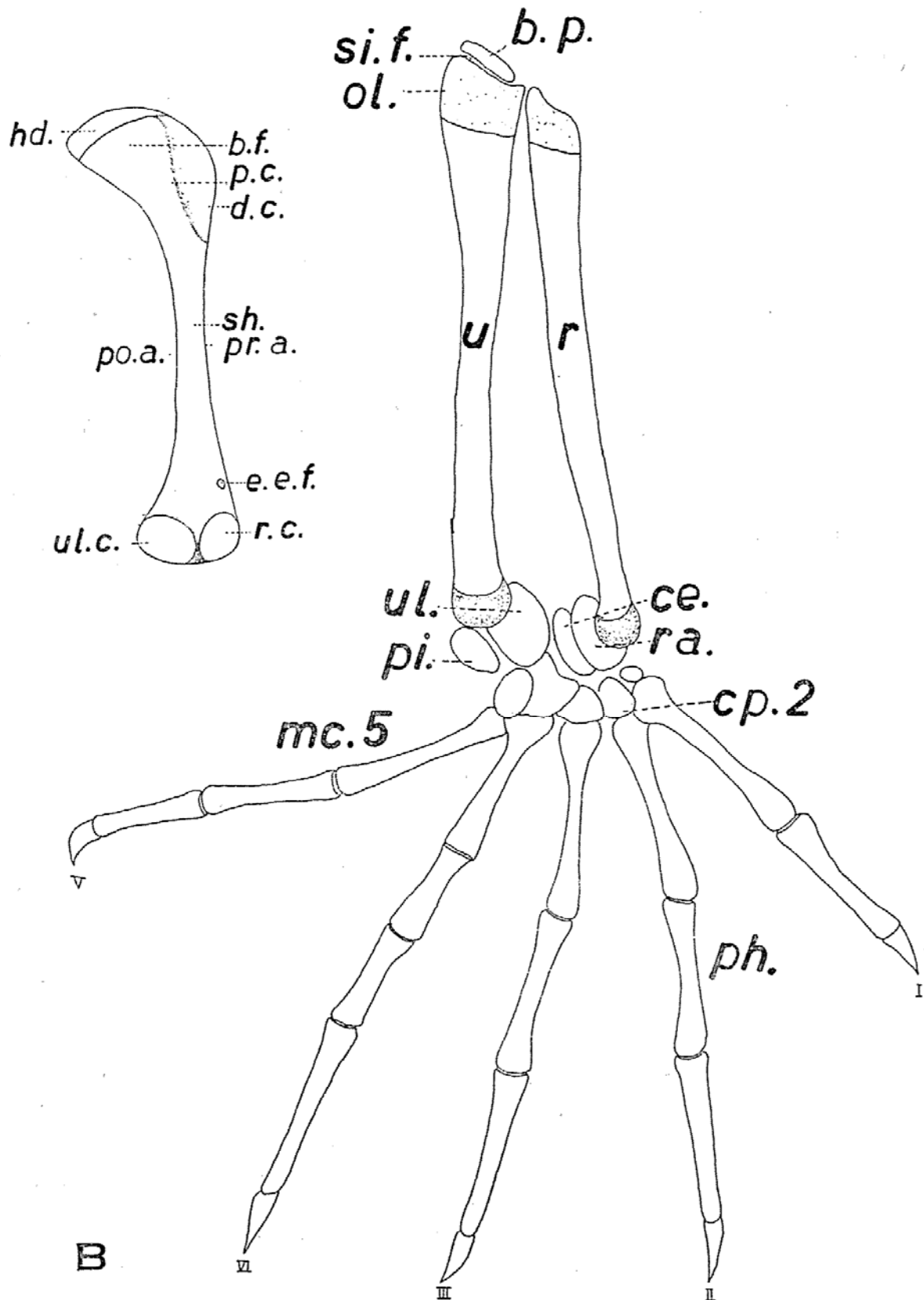
Fig. 23. Ventral view of the left anterior limb of *H. bowringii*. A. the humerus. B. the radius, ulna and bones of manus.

A   **B**
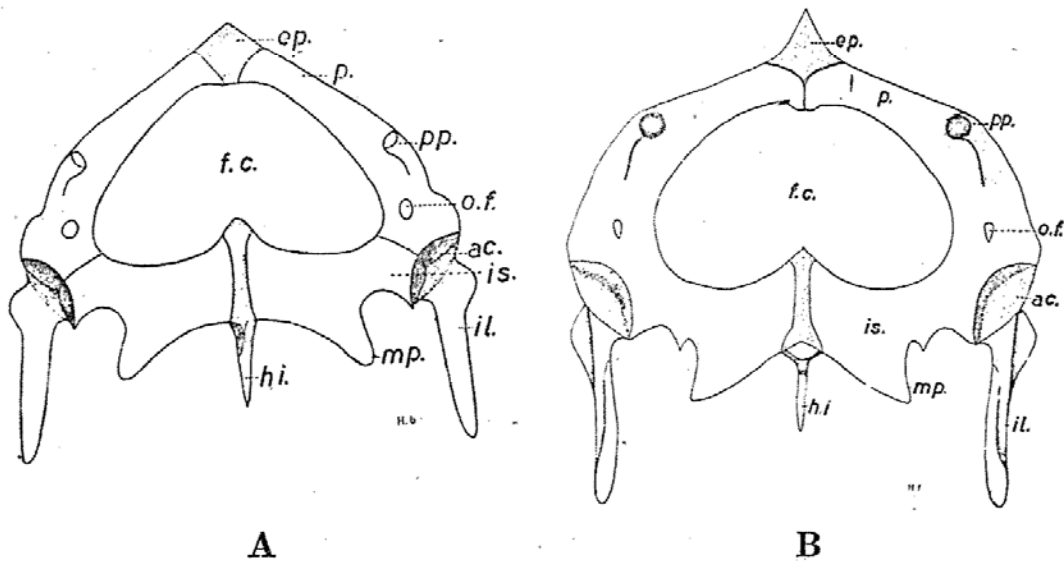
Fig. 24. Ventral view of the pelvic girdle. A. *H. bowringii*. B. *H. frenatus*.
H. frenatus. Dotted area represents the cartilage.

The manus consists of 5 *metacarpals*, each followed by the phalanges. The phalangeal formula of the *H. bowringii* is 2-3-3-4-3.

C. *Pelvic girdle*

The pelvic girdle is composed of two halves of a triradiate bone which is formed by the dorsal ilium, ventro-anterior pubis, and the ventro-posterior ischium. All these bones take part in the formation of the shallow depression, the *acetabulum*. These bones are distinct from each other in young specimen but they are fused into a single bone in the adult.

The *ilium* is a flat, rod-shaped bone, which directs upward and backward and articulates with the articular surface of the transverse process of the sacral vertebrae by means of the inner surface of the ilium.

The *pubis* is a dorso-ventrally flattened bone. It is almost horizontally directed from the acetabulum forward and inward to fuse with the rhomboidal cartilagenous *epipubis* which is wedged in between the anterior end of the pubis. There is a small foramen near the acetabular fossa in each pubis. This is the *obturator foramen*. The *prepubic* or *pectineal process* is moderately developed.

The *ischium* is also dorso-ventrally flattened and horizontally

projects to the medial direction from the acetablum to fuse with a slender, rod-shaped cartilagenous *hypoischium* in the mid-line. The bone is broader medially. It bears a *metischial process* at the posterior border. There is a slender rod-shaped hypoischium which projects from the *ischiatic symphysis* backward to support the ventral wall of the cloaca.

The pubis and ischia bound the heart-shaped space, the *ischiopubic fenestra* or *foramen cordiforme.*

D. *Hind Limb*

Femur: The column-like femur is a slightly curved bone. It has an ovoidal head which articulates with the acetabulum of the pelvic girdle, and a massive *internal trochanter* on the ventral side of the head. On the postaxial surface between the head and internal trochanter of the femur there is a deep *intertrochanteric fossa.* The expanded end of the femur has a large articular surface on the preaxial side of the condyle for the articulation with the tubia and a smaller articular surface on the postaxial margin of the condyle for the articulation with the fibula.

There are four small *patella* bones on the knee joint. The largest one is on the upper side of the condyle of the femur, the other two patella tibialis are wedged between the femur and the tibia. The parafibula is wedged between the femur, fibula, and tibia.

Tibia: The tibia is a stout compressed bone. The triangular head is greatly expanded, with pseudepiphysis and gradually narrow to the rounded distal end, the flat surface of the proximal end of the tibia articulates with the femur and the distal end articulates with the preaxial side of the tibio-fibulale.

Fibula: The flat fibula is more slender than the tibia. The slender head articulates with the femur but not with the tibia, and gradually expands to the distal end which articulates with the proximal part of the tibio-fibulale.

Tarsus: The tarsus consists of five bones arranged in proximal, middle, and distal rows. The proximal row is represented by a large *tibio-fibulale* in the adult. It is a fused tibiale and fibulale. The tibio-
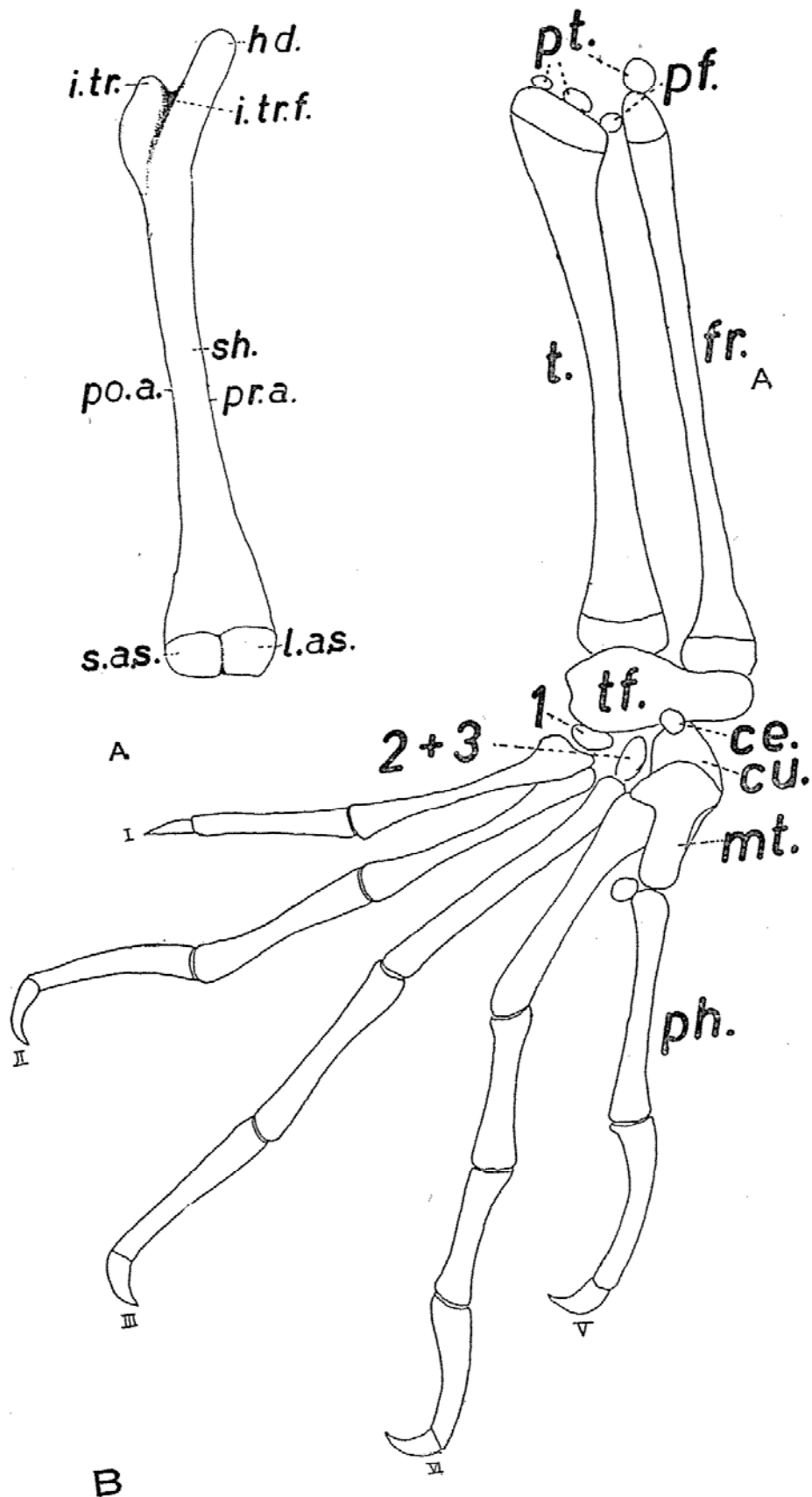
Fig. 25. A. Anterior-ventral view of the left femur. B. Dorsal view of left foot.

fibulale articulates with the tibia and fibula proximally and with the first, second, and third tarsals and cuboid bones distally. The middle row is only represented by a small node-like *centrale*. The distal row of the *tarsus* consists of three bones: (a) a small flat first tarsal in contact with the tibio-fibulale and the first metatarsals, (b) the triangular shaped second and third tarsal articulate with the tibio-fibulale, cuboid, the 2nd, and the 3rd metatarsals, (c) the *cuboid bone* is a fairly large bone which articulates with the tibio-fibulale, third tarsal, fourth, and fifth metatarsals. The fifth metatarsal is the last bone on the distal row of the tarsus.

Of the five *metatarsals* the fifth is shortest, it is probably the fused bone of the fifth tarsal and fifth metatarsal. The first and the fourth metatarsals are the next shorter ones. Each metatarsal is followed by phalanges. The phalangeal formula of the hind limbs of the *H. bowringii* is 2-3-3-4-3.

E. *The Cloacal Bones*

The cloacal bones of the male are subcutaneous elements which lie posterior to the anal vent. They are L-shaped, and their medial ends are pointed and slightly hocked, but their lateral ends are blunt and directed to the medial posterior side in the adult. In young specimens, the medial end of the cloacal bone is not hocked.

Fig. 26. Cloacal bones. A. *H. frenatus* B. *H. bowringii*.

THE COMPARISON OF THE SKELETON OF *H. BOWRINGII* AND *H. FRENATUS* IN SUMMARY

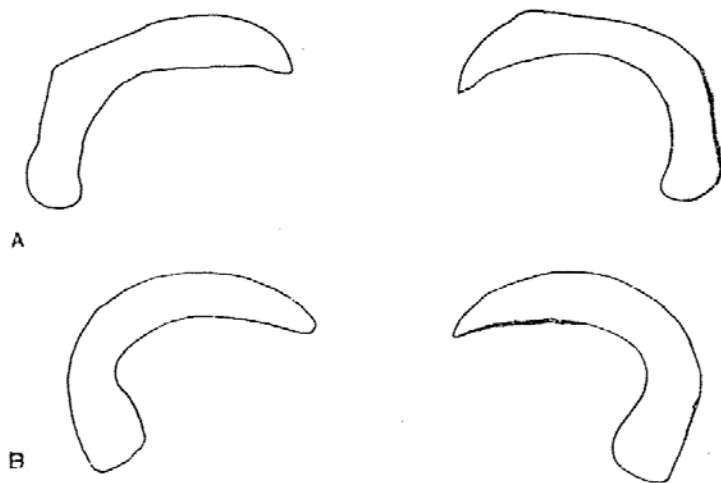**Skull:** In general the skulls of both species are much alike. They are depressed, broad, and flattened.

The comparisons of the skeletal structures of both species are chiefly based on the details of the structure of each bone. The differences in the structures of each bone between both species are given below:

Parietals: The width of crest is broader in *H. frenatus* than *H. bowringii* (The width of the crest of parietal to the width of the remainder portion of the parietal is about 2:5 in *H. bowringii* but is about 3:5 in *H. frenatus*) (Fig. 8).

Frontals: The greatest width of the supraorbital crest of the frontal is nearly equal to, or smaller than the smallest diameter of the olfactory canal in *H. bowringii* but it is about two times the diameter of the olfactory in *H. frenatus*. The ratio of the narrowest width to the length of the frontal is 0.21 in *H. bowringii*, but is 0.33 in the *H. frentatus* (Fig. 1 and Fig. 6).

Prootic: The alar process (Fig. 2, al.p.) of the prootic forms only the anterior boundary of the external auditory recess in *H. bowringii* but forms the anterior and incompletely the lateral boundary of the external auditory recess in *H. frenatus* (Fig. 2). The alar process of the prootic extends outwardly beyond the lateral margin of the parietal in *H. frenatus*, but it does not in *H. bowringii*. The superior border connecting the anterior and posterior process of the prootic is largely concave in *H. bowringii* but is slightly concave in *H. frenatus*. (Fig. 7).

Postfrontal: Both the anterior and posterior rami of the postfrontals are slender and of equal width, and the anterior and posterior tips are pointed in *H. bowringii*, while in *H. frenatus*, the anterior ramus is narrower than the posterior ramus, both the anterior and posterior tips are blunt (Figs. 1 and 10).

Septomaxilla: The posterior process is nearly parallel to the septal process and is straight in *H. bowringii* but is slightly curved

inward in *H. frenatus*. The groove on the posterior process is directed toward the lateral side in *H. bowringii* but directed in the dorso-lateral direction in *H. frenatus*. The septomaxilla is wider in *H. bowringii* than in *H. frenatus* (excluding posterior process and septal process) (Fig. 12).

Quadrate: The concha of quadrates are more highly developed in *H. bowringii* than in *H. frenatus* (Fig. 13). The candylus cephalius is elliptical in *H. bowringii* but is spherical in *H. frenatus*.

Squamosal: The posterior end of the squamosal is pointed in *H. frenatus* but it is blunt in *H. bowringii*.

Pterygoid: The ectopterygoid process of the pterygoid gives rise dorsally and ventrally into high ridges in *H. frenatus*, while the dorsal ridge is absent in *H. bowringii*. The quadrate process of the pterygoids is short in *H. frenatus* as compared with the long quadrate process of *H. bowringii* (Fig. 15).

Palatine: The anterior end of the lateral border of the palatine is notched in *H. frenatus* but it is without notch in *H. bowringii*.

Prevomer: The postero-medial process of prevomer is slender in *H. frenatus* but it is broad and plate-like in *H. bowringii*. The lateral corner of the dorsal ridge of the antero-lateral edge of the prevomer is highly developed in the adult specimen of *H. bowringii*, but is not in *H. frenatus* (Fig. 16).

Parasphenoid: The round, rod-like parasphenoid of *H. bowringii* is calcified on the posterior half of the bone. While in *H. frenatus* the major part of the parasphenoid is calcified, except the portion entering the nasal capsules.

Maxilla: The anterior part of the dorsal margin of the pars nasalis of the maxilla develops a longitudinal, narrow articular surface to articulate with the antero-lateral margin of the nasal in *H. frenatus*, while this articular surface is absent in *H. bowringii* (Fig. 17).

Premaxilla: The nasal process of the premaxilla is longer than the width of the pars dentalis in *H. frenatus* but it is shorter than the width of the pars dentalis in *H. bowringii*. The maxillary process touches the line connecting the anterior margin of the aperture of

Jacobson's organ of each side in *H. frenatus*, but it only reaches a short distance in front of the anterior margin of the aperture of the Jacobson's organ in *H. bowringii* (Fig. 18).

Teeth: The maxillary teeth on one side of the maxilla varies from 30 to 40 in *H. frenatus* but varies from 22–34 in *H. bowringii*. The mandibular teeth range from 34–37 in *H. frenatus*, but 31 (one specimen) in *H. bowringii*.

Vertebral column: The number of vertebrae in each region of both species is listed below:

	H. bowringii	*H. frenatus*
Cervical	8	8
Anterior thoracics	3	3–5
Posterior thoracics	14	12–14
Lumber	1	1
Sacral	2	2
Precaudal	5	5

Atlas: The postzygapophysis of atlas is blunt in *H. frenatus* but it is pointed in *H. bowringii*. On the neural arch pedicel, a postero-laterally projecting tuberosity is not present in *H. frenatus*.

Axis: In *H. frenatus*, the hypapophysis of the second intercentrum have three processes, of which the medial hypapophysis directs ventro-anteriorly and the two lateral ones direct ventro-posteriorly, while in *H. bowringii* there is only one process on the 2nd hypapophysis. It is directed ventro-posteriorly in young specimens but is directed to the back in the adult specimens. The neural crest of the axis is long in *H. frenatus* but is short in *H. bowringii*. The third intercentrum bears hypapophysis (3rd hp.), which articulates with the centrum of the axis in the young and fuses with the centrum in the adult of *H. bowringii*.

Intercentrum: The intercentrum between the 7th and 8th vertebrae in *H. frenatus* bears hypapophysis but it is absent in *H. bowringii*. The hypapophyses of the intercentrum are longer in *H. frenatus*.

Chevron bones: The chevron bones are present in the first 16 postcaudals in *H. frenatus* but they are present only in the first 7

postcaudals in *H. bowringii*. The transverse processes are present in numerous post-caudals except the caudal ring of the distal ones in *H. frenatus*, but they are present only in the first seven post-caudals in *H. bowringii*.

Cloacal bones: The angle formed by the anterior and posterior rami of cloacal bones is less than 90° in *H. bowringii* and is bigger than 90° in *H. frenatus* (Fig. 26).

Pectoral girdle: The medial end of the clavicles is broadest in *H. bowringii* but the central portion of the clavicle is broadest in *H. frenatus*. The scapular ray of the scapula is slightly pointed in *H. frenatus* but it is cut edged in *H. bowringii*. The major portion between the secondary coracoid ray and the epicoracoid is cartilaginous in *H. frenatus* but is calcified in *H. bowringii* (Fig. 22). The suprascapula of *H. frenatus* is completely calcified, but it is partially calcified in *H. bowringii* (Fig. 22).

Sternal and mesosternal or xiphisternal ribs: The first two (in 3 specimens) or three (in 14 specimens) of the thoracic ribs are tied to the sternum by slender true sternal ribs. The next one (in 15 specimens) or two (in 3 specimens) bear similar long mesosternal or xiphisternal ribs, of which the last one may or may not join with the xiphisternum.

The variations of the numbers of sternal and mesosternal ribs appear to be due to the variable attachment of the ribs of the 11th, 12th, and 13th vertebrae with the sternum and xiphisternum. The 11th may lose its attachment to the sternum and shift to the xiphisternum. The 12th and 13th may lose its attachment to the xiphisternum and thus end free (Fig. 22). The model formulas are: *H. bowringii* (2+1)/5 specimens; *H. frenatus* (3+1)/25 specimens, (2+2)/2 specimens, (2+1)/1 specimens and (3+2)/1 specimens.

Pelvic girdle: The pelvic girdle of both species are much alike in structure. The anterior end of the pubis of each side is completely separated from the epipubis in *H. bowringii*, but it is partially separated from the epipubis in *H. frenatus*. The posterior hoof of the hypoischium of *H. bowringii* is simple spinous in structure but

is Y-shaped in *H. frenatus.* A small spine beside the metischial process is present in *H. frenatus* but it is absent in *H. bowringii.*

Table. Variation in the number of sternal and mesosternal ribs in individuals of these two species of Hemidactylus

	H. bowringii	*H. frenatus*
No. of sternal ribs		
2	5	2
3	0	24
2/3	0	2
No. of mesosternal ribs		
1	5	25
2	0	2
1/2	0	1

ABBREVIATIONS

a.a.p.	antero-lateral alar process.
a.b.	auditory bulla.
a.c.	articular condyle.
a.c.t.n.	aperture for the entrance of the chorda tympani branch of the VIIth nerve.
a.c.v.	anterior opening of vidian canal.
a.ch.	aperture for the channel of posterior vertical semicircular canal.
a.e.ept.p.	ectopterygoid process.
a.g.	articular groove.
a.i.pa.p.	paratal process.
a.j.o.	aperture for the Jacobson's organ.
a.m.	aperture medialis recessus scalae tympani.
a.na.	neurapophysis of atlas.
a.p.	anterior process of prootic.
a.p.s.	antero-posterior sulcus.
a.s.f.	anterior surangular foramen.
a.v.s.c.	anterior vertical semicircular canal.

a.z.	autotomizing zone.
a.c.	acetabulum.
al.p.	alar process of prootic.
an.p.	anterior process of septomaxilla.
ang.	angular.
art.	articular.
b.	body of quadrate.
b.d.	basicranial depression.
b.f.	bicipital fossa.
b.p.	brachial patella (patella ulnaris).
b.pty.	basipterygoid process.
b.h.	basihyal.
b.c.	basioccipital.
b.s.	basisphenoid.
c.	ceratohyal.
cI.	first ceratobranchial.
c.a.v.s.c.	channel for the anterior vertical semicircular canal.
c.c.	dorsal head (condylus cephalicus).
c.d.	crista dentalis.
c.m.	cartilagenous pterygoid meniscus.
c.s.	crista sellaris.
c.v.	chevron bone.
ce.	centrale.
cen.	centrum.
cl.	clavicle.
clf.	clavicular fenestra.
co.m.	ventral head of quadrate (condylus mandibularis).
cor.	coronoid.
cp.	carpals (1–5).
co.	coracoid.
cr.	crest.
cu.	cuboid.
d.a.c.	dorsal roof of auditory capsule.
d.c.	deltoid crest.
dent.	dentary.

drb.	distal cartilagenous rib.
e.	epihyal.
eI.	first epibaranchial.
e.a.r.	external ampula recess.
e.aur.	external auditory recess.
e.e.f.	ectepicondylar foramen.
e.f.	endolymphatic foramen.
e.n.	external nares.
ec.	ectopterygoid.
ep.	epipubis.
ep.c.	epicoracoid.
ept.	epipterygoid.
ex.o.	exoccipital.
f.a.	articular facet.
f.a.i.	foramina for the passage of the nervous alveolaris inferior.
f.c.	ischio-pubic fenestra (foramen cordiforme).
f.c.r.m.i.	foramen for the nervous cutaneous recurrens maxillae, inferior branch of the mandibular division of the 5th nerve.
f.col.	fossa columellae.
f.j.o.	floor of the Jacobson's organ.
f.m.	foramen magnum.
f.n.c.	floor of the nasal capsule.
f.o.	foramen ovale.
f.p.mx.	frontal process of maxilla.
f.p.p.	frontal process of parietal.
fi.	fibula.
fr.	frontal.
g.	glossohyal.
g.f.	glenoid forra.
h.	hypophyal.
h.d.	head.
h.f.	hypophysial fossa (sella turucica).
h.i.	hypoischium.
h.s.c.	horizontal semicircular canal.

he.	hypocentrum.
hp.	hypapophysis.
i.	interclavicle.
i.a.p.	inner anterior process of coronoid.
i.a.r.	internal ampular recess.
i.au.r.	internal auditory recess.
i.c.	intercalary cartilage.
i.c.f.	internal carotid foramen.
i.cen.	intercentrum.
i.f.	incisive foramen.
i.n.	internal nares.
i.or.f.	infra-orbital foramen.
s.or.fo.	sub-orbital fenestra.
i.p.p.	inner posterior process of coronoid.
i.tr.	internal trochanter.
i.tr.f.	inter-trochanteric fossa.
i.v.	interpterygoid vacuity.
ie.	illium.
is.	ischium.
j.	jugal.
j.f.	jugular foramen (X, XI)
l.a.s.	large articular surface.
l.a.f.	lateral occipital fenestra.
l.c.f.	lateral condylar facet.
l.f.p.	lateral frontal process.
l.i.p.	lateral infraorbital process.
l.l.r.	lateral longitudinal ridge.
l.p.p.	lateral posterior process of septomaxilla.
l.p.p.vo.	postero-lateral process of the prevomer.
m.c.f.	medial condylar facet.
m.f.	maxillary foramina.
m.f.p.	medial frontal process.
m.i.p.	medial infraorbital process.
m.p.p.vo.	medial plate of prevomer.
m.p.pmx.	maxillary process of premaxilla.

m.p.t.	mid-posterior premaxillary teeth.
m.s.	surface of the mandibular symphysis.
ma.f.	mandibular foramen.
ma.fo.	mandibular fossa.
mc.	metacarpals (1-5).
me.f.	mental foramina.
mp.	metischial process.
mt.	metatarsals.
mx.	maxilla.
mxp.f.	maxillary process of frontal.
mxp.pmx.	maxillary process of premaxilla.
n.	notch.
n.c.	neural canal.
n.cr.	neural crest.
n.pmx.	nasal process of premaxilla.
n.s.	neural spine.
na.a.	neurapophysis of axis.
nap.	neural arch pedicle.
nas.	nasal.
o.c.	occipital condyle.
o.c.ex.	occipital condyle of exoccipital.
od.	odontoid process (centrum of atlas)
o.f.	obturator foramen.
ol.	oleclanon.
ol.c.	olfactory canal.
olf.	olfactory chamber.
op.	opisthotic.
p.	pubis.
p.a.	pre-articular.
p.c.	pectoral crest.
p.c.f.	primary coracoid fenestra.
p.c.r.	primary coracoid ray.
p.c.v.	posterior craniopterygoid vacuity.
p.con.	pars condyloidea of basioccipital.
p.d.pmx.	pars dentalis of premaxilla.

p.f.	parafibula.
p.fr.	prefrontal.
p.m.	processus messetericus.
p.m.f.	posterior myelohyoid foramen.
p.mxp.	posterior maxillary process.
p.n.	pars nasalis.
p.p.	posterior process of prootic.
p.p.op.	paroccipital process of the opisthotic.
p.s.	parasphenoid.
p.s.p.	parasphenoid process.
p.s.f.	posterior surangular foramen.
p.s.mx.	palatal shelf of maxilla.
p.s.pmx.	palatal shelf of premaxilla.
p.t.	pars trigeminalis.
p.ti.	patella tibialis.
p.v.s.c.	posterior ventical semicircular canal.
p.t.f.	post-temporal fossa.
p.vo.	prevomer.
p.vo.f.	prevomerine foramen.
p.z.	postzygapophysis.
pal.	palatine.
pal.n.	palatine notch.
par.	parietal.
pas.	parapophysis.
ph.	phalanges.
pi.	pisciform.
pmx.	premaxilla.
po.a.	postaxial.
po.fr.	postfrontal.
pp.	pectineal or prepubic process.
pr.a.	preaxial.
pr.r.	proximal rib.
pr.z.	prezygapophysis.
pro.	prootic.
ps.	pseudepiphysial plate.

pty.	pterygoid.
q.	quadrate.
q.pty.	quadrate process of the pterygoid.
r.	radius.
r.art.p.	retroarticular process.
r.c.	radial condyle (capitulum).
r.r.fr.	round ridge of frontal.
r.s.t.	recessus scalae tympani.
ra.	radiale.
s.	sulcus.
s.a.s.	small articular surface.
s.ang.	surangular.
s.c.	scapulo-coracoid.
s.c.f.	supra-coracoid foramen.
s.c.fe.	secondary coracoid fenestra
s.c.r.	secondary coracoid ray.
s.f.	scapular fenestra.
s.mx.	septomaxilla.
s.o.	supraoccipital.
s.o.c.	supra-orbital crest.
s.o.f.	supra-orbital fossa.
s.o.p.	space for odontoid process.
s.o.t.	spheno-occipital tubercle.
s.p.	septal process.
s.pmx.t.	socket for mid-posterior premaxillary teeth.
s.r.	scapular ray.
s.t.p.	supra-temporal process of parietal.
sh.	shaft.
si.f.	sigmoid fossa.
ss.	supra-scapula.
st.	sternum.
st.r.	sternal rib.
t.	squamosal.
t.i.a.p.	transverse interior alar process.
t.l.w.	thin lateral wing.

t.p.s.	thin process projected into the ventral concavity of the septomaxilla.
ti.	tibia.
tf.	tibio-fibulale.
tl.	transverse ligament.
tp.	transverse process.
tps.	transverse plate of sacrum.
u.	ulna.
ul.c.	ulnar condyle (trochlea).
v.	vestibule.
v.l.p.	ventro-lateral process.
x.	xiphisternum.
V.	trigeminal nerve foramen.
VIa.	anterior foramen for abducence nerve.
VIp.	posterior foramen for abducence nerve.
VIIhm.	anterior facial nerve foramen.
VIIpal.	anterior facial foramen through which the palatine branch of the VIIth nerve leaves the skull.
VIIIa.	anterior auditory foramen.
VIIIp.	posterior auditory foramen.
IX.	glossopharyngeal nerve foramen.
X.	vagus nerve foramen.
XI.	spinal accessary nerve foramen.
XII.	hypoglossal foramen.
1, 2+3	distal row of tarsals.

REFERENCES

(1) Bahl, K. N. 1937. Skull of Varanus monitor (Linn.). *Records of Indian Museum*, Vol. 39, Pt. II, pp. 133–174.

(2) Boulenger, G. A. 1885. *Cat. Liz. Brit. Mus.* I.

(3) Etheridge, Richard. 1964. The skeletal morphology and systematic relationships of Sceloporine lizards. *Copeia* 1964, No. 4, pp. 610–631.

(4) King, Diame. 1964. The osteology of the water skink, Lygosoma (Sphenomorphus) quoyii. *Australian Journal of Zoology*, Vol. 12, No. 2, pp. 201–216.

(5) Kluge, Arnold G. 1962. Comparative osteology of the Eublepharid lizard Genus Coleonys Gary. *J. Morph.* Vol. 110, pp. 299–332.

(6) Kluge, A. G. 1967. Higher taxonomic categories of geckonid lizards and their evolution. *Bull. Am. Mus. Nat. Hist.* Vol. 135, pp. 1-60.

(7) Kluge, A. G. 1967. Systematics, phylogeny, and zoogeography of the lizard genus Diplodactylus gray (Gekkonidae). *Aust. J. Zool.* Vol. 15, pp. 107-108.

(8) Lundelius, Ernest L. Jr. 1957. Skeletal adaptation in two species of Sceloporus. *Evolution*, Vol. 11, No. 1, pp. 65-83.

(9) Mcdowell, Samuel Booker & Bogert, Charles M. 1954. The position of Lanthanotus and the affinities of the anguinomorphan lizards. *Bull. of the Amer. Museum of Natural History.* Vol. 105, art. 1.

(10) Mahendra. Beni Choran. 1949. The skull of the Indian housegecko, Hemidactylus flaviviridis Ruppel. *Proceedings of the Zoological Society of Bengal*, Vol. 2, No. 1, pp. 29-42.

(11) Mahendra, Beni Choran. 1950. The osteology of the Indian house gecko, Hemidactylus flaviviridis Ruppel. *Proceedings of the Zoological Society of Bengal*, Vol. 3, No. 1, pp. 49-64.

(12) Mak'ı Moichior. 1923. On some geckos from Formosa. *Jap. Zoological Magazine*, Vol. 35, No. 415, pp. 193-203.

(13) Okada. Y. 1936. Studies on the lizards of Japan, Contribution I. Gekkonidae. *Tokyo Bunrika Daigaku, Science Report, Section B*, Vol. 2, No. 42.

(14) Presch, William. 1969. Evolutionary osteology and relationships of the horned lizard genus Phrynosoma (Family Iguanidae). *Copeia*, 1969, No. 3, pp. 250-275.

(15) Stejneger, L. 1907. Herpetology of Japan and adjacent territory. *U.S. Nat. Mus. Bull.* Vol. 58.

CONTRIBUTORS TO THIS NUMBER

John Koster, SVD, Ph. D., spent one year (1971/72) as a guest professor in the Physics department of Fu Jen University. He is presently chairman of the Computer Science department and professor of Physics at the University of Ghana, West Africa.

Günter Breuer, Ph. D., I. Institut für Experimentalphysik, Universität Hamburg, West Germany, is presently associate professor of Physics at Fu Jen University.

Hans-Wilhelm Scharpenseel, Ph. D., is professor at the Institut für Bodenkunde, Abt. f. Tropische Böden und Bodenradiometrie, Universität Bonn, West Germany. Together with his coworkers, he spent four months of research at Fu Jen University.

Yung-Sheng Liang, is chairman of the Zoology department, National Taiwan University, and professor of Biology at Fu Jen University.